Ultrasonic Seismic Wave Attenuation, Petrophysical Models and Work Flows for Better Subsurface Imaging, Energy Exploration, and Tracking of Sequestrated Carbon Dioxide

by

Daniel E. Delaney

B.S. Physics and Astronomy, University of Pittsburgh, 2012

Submitted to the Graduate Faculty of the

Kenneth P. Dietrich School of Arts and Sciences

in partial fulfillment

of the requirements for the degree of

Master of Science

University of Pittsburgh

2013

UNIVERSITY OF PITTSBURGH

Dietrich School of Arts and Science

Geology and Planetary Sciences

This thesis was presented

by

Daniel E. Delaney

It was defended on

July 25, 2013

and approved by

Daniel Bain, Assistant Professor, Geology and Planetary Science

Thomas Anderson, Professor Emeritus, Geology and Planetary Science

William Harbert, Department Chair and Professor, Geology and Planetary Science

Thesis Director: William Harbert, Department Chair and Professor, Geology and Planetary Science

Ultrasonic Seismic Wave Attenuation, Petrophysical Models and Work Flows for Better Subsurface Imaging, Energy Exploration, and Tracking of Sequestrated Carbon Dioxide

Daniel E. Delaney, M.S.

University of Pittsburgh, 2013

Ultrasonic Seismic Wave Attenuation, Petrophysical Models and Work Flows for Better Subsurface Imaging, Energy Exploration, and Tracking of Sequestrated Carbon Dioxide

Daniel E. Delaney, M.S.

University of Pittsburgh, 2013

Parameters related to seismic and ultrasonic elastic waves traveling through a porous rock material with compliant pores, cracks and isometric pores are subject to variations, which are dependent on the physical properties of the rock. The goal of this research is to understand these variations in rhyolite and carbonate samples. Understanding these materials is relevant to enhanced oil recovery, enhanced geothermal, and CO_2 storage activities. Experiments simulating subsurface conditions were performed in the COREFLOW laboratory at the National Energy Technology Laboratory (NETL) of the United States Department of Energy (DOE) with varied pore-filling fluids, effective pressures (0.01 to 50 MPa), and temperatures (21° to 80° C). P, S1 and S2 ultrasonic velocities were measured using a New England Research (NER) Autolab 1500 device, allowing calculation of the lame parameters (Bulk modulus (K), Young's modulus (E), Lamè's first parameter (λ), Shear modulus (G), Poisson's ratio (ν), P-wave modulus (M)). Using an aluminum reference core and the ultrasonic waveform data collected, we employed the spectral ratio method to estimate the quality factor for the P seismic wave. The quality factor (Q) is a dimensionless value that represents the attenuation of a seismic wave as it travels through a rock. Carbonate samples were tested dry (atmospheric gas as pore fluid) as well as saturated with deionized water, oil, and CO_2. Understanding wave attenuation and the elastic nature of

these materials and sensitivity to physical change will be a powerful tool for better subsurface imaging, tracking sequestered CO_2, and energy exploration.

Our research indicates porosity, heterogeneities, temperature, pressure and pore filling fluids are physical controls on wave attenuation and shifts $\lambda\rho$-$\mu\rho$ space. The effects of temperature and pressure on elatic attenuation and $\lambda\rho$-$\mu\rho$ are less significatnt than porosity and rock hetergeneities. The presence of fluids causes a distinct shift in $\lambda\rho$ which provides isight into subsurface exploration such as AVO classifaction. Our results will prove useful in enhancing subsurface imaging, analysis and exploration.

TABLE OF CONTENTS

LIST OF TABLES

LIST OF FIGURES

LIST OF EQUATIONS

1.0 INTRODUCTION

Seismic imaging, sonic wire-line log, and vertical seismic profile analysis are powerful tools used to understand the subsurface, for energy exploration, and tracking of fluids such as sequestered CO_2. In order to clarify the ambiguities in seismic analysis and to improve detection and tracking of fluids within the subsurface, we must characterize how rock and seismic wave reactions to physical changes such as temperature, pressure, porosity, and fluid saturation. Throughout this thesis rock is defined and examined in terms of its framework, porosity, and pore filling phases. Ultimately, thorough understanding of rock mechanics and elastic wave interactions with rock is crucial for understanding and enhancing seismic methods, technologies and analysis of seismic data.

This thesis presents experimental results from 19 rock core samples subjected to physical changes including temperature, pressure, porosity, and fluid saturation. Results are synthesized to characterize the effects of physical changes on the elastic nature of reservoir rock and seismic waves passing through the rock. These results can be applied to understanding rock mechanics, improving subsurface imaging, and detecting and tracking fluids such as sequestered CO_2 (Figure 1).

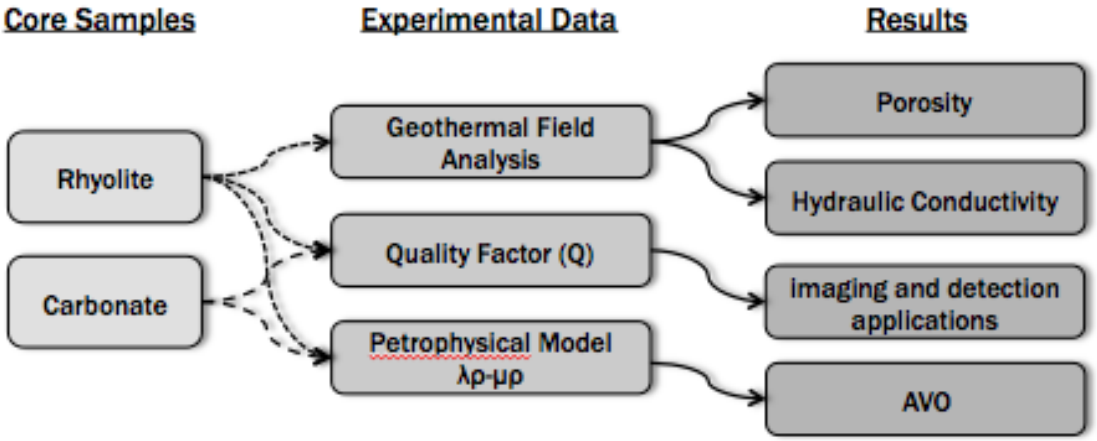

Figure 1:Research flow highlighting the experiments performed on each core and applications.

Experiments were performed on carbonate cores from an enhanced oil recovery (EOR) and CO2 sequestration reservoir, as well as rhyolite cores from a geothermal site near Reno Nevada (**Table 1** and **Table 2**). Experimental data was used to construct a petrophysical model, allowing enhanced assessment of the subsurface based on seismic reflection data and further, improved fluid detection via AVO (Amplitude Variation with Offset) analysis.

Elastic Experiments					
	Carbonate		Rhyolite		
Porosity (%)	18.5	8	9.5	17.5	0.47-18.16
Temperature (°C)	50	50	21 36 52 73	21 38 57 75 80	20
Pore-Filling Fluids	Dry (Air) CO_2 DeionizedWater Oil/CO_2	Dry (Air) CO_2 DeionizedWater	Dry	Dry	Dry

Table 1: Table depicts all elastic experiments and measurements taken on core samples. *Rhyolite core porosities: 16.75, 10.98, 9.47, 3.03, 1.28, 2, 11.5, 5.94, 17.17, 18.16, 7.14, 5.54, 0.49, 2.56, 0.77, 1.55, and 0.47%.

Attenuation Experiments				
	Carbonate		Rhyolite	
Porosity (%)	18.5	8	9.5	17.5
Temperature (°C)	50	50	21 36 52 73	21 38 57 75 80
Pore-Filling Fluids	Dry (Air) CO_2 DeionizedWater Oil/CO_2	Dry (Air) CO_2 DeionizedWater	Dry	Dry
Angle (°) **(Anisotropy)**	0 45 90 135	0 45 90 135	N/A	N/A

Table 2: Table depicts all attenuation experiments and measurements made on core samples. N/A indicates experiments were not performed.

1.1.1 Permian Basin Carbonate Cores

Carbonate sample cores were collected from near an EOR injection site located within the Permian Basin of western Texas, a region mined for its hydrocarbon resources (Figure 2). Utilizing EOR methods, the site was flooded with water in order to force out hydrocarbons and beginning in 2008 the reservoir was utilized as a location for CO_2 sequestration. Large amounts of CO_2 were flooded into the reservoir for storage. Understanding CO_2 in reservoirs is important for assessing possible risk of carbon sequestration. Our sample cores are collected from an active EOR and CO_2 sequestration reservoir, making experimental results immediately applicable to real field scenarios. The potential insight into EOR methods and CO_2 sequestration affects the elastic nature of reservoir rock enhances our ability to detect fluids stored within a reservoir.

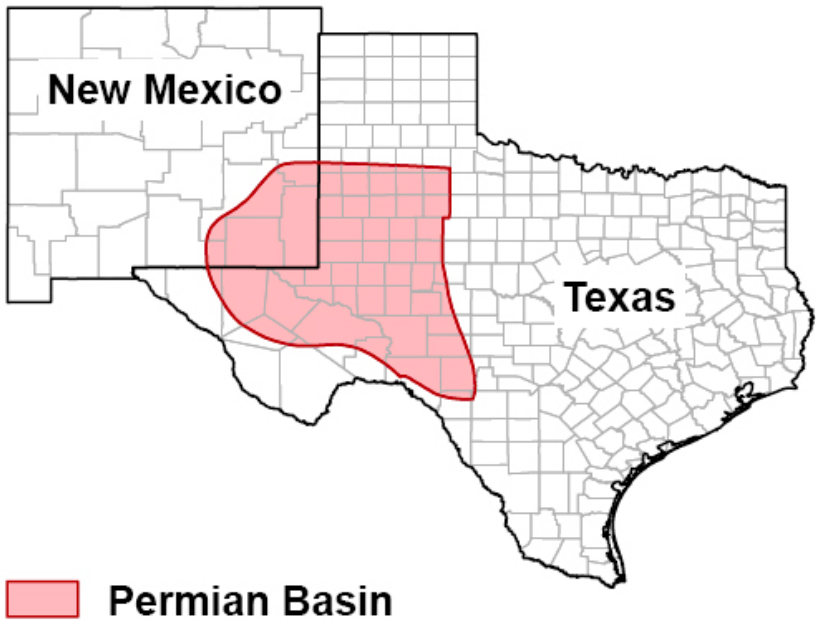

Figure 2: Map depicting the location of the Permian basin. Image Source: CircleStar Energy <http://www.circlestarenergy.com/projects/texas/permian-basin >

1.1.2 The Geothermal Well

The geothermal field is located in Churchill County just outside of Reno, Nevada and is an active source of energy. The reservoir temperature of the geothermal field has been estimated to be between 175-205°C at depth of 1-2 km (Brohmal 2011). The site is an established energy source and is currently powering a combined flash and binary power plant with a generation capacity of 16-17 MW (Brohmal 2011). A map view of the location of Churchill County can be seen in Figure 3 below.

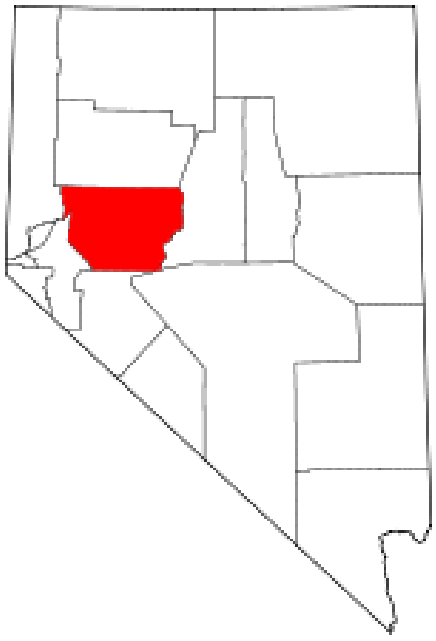

Figure 3: Map of Nevada highlighting Churchill county. Image Source: <https://familysearch.org/learn/wiki/en/File:Nv-churchill.png>

The stratigraphy underneath the geothermal field is highly deformed and faulted. The field is primarily composed of igneous rocks and ridden with closely spaced northeast trending folds within the rock that form as a result of cross cutting faults (Faulds, Garside et al. 2002, Faulds, Moeck et al. 2010). **Figure 4** below displays a cross section of the region displaying the complex geology of the field.

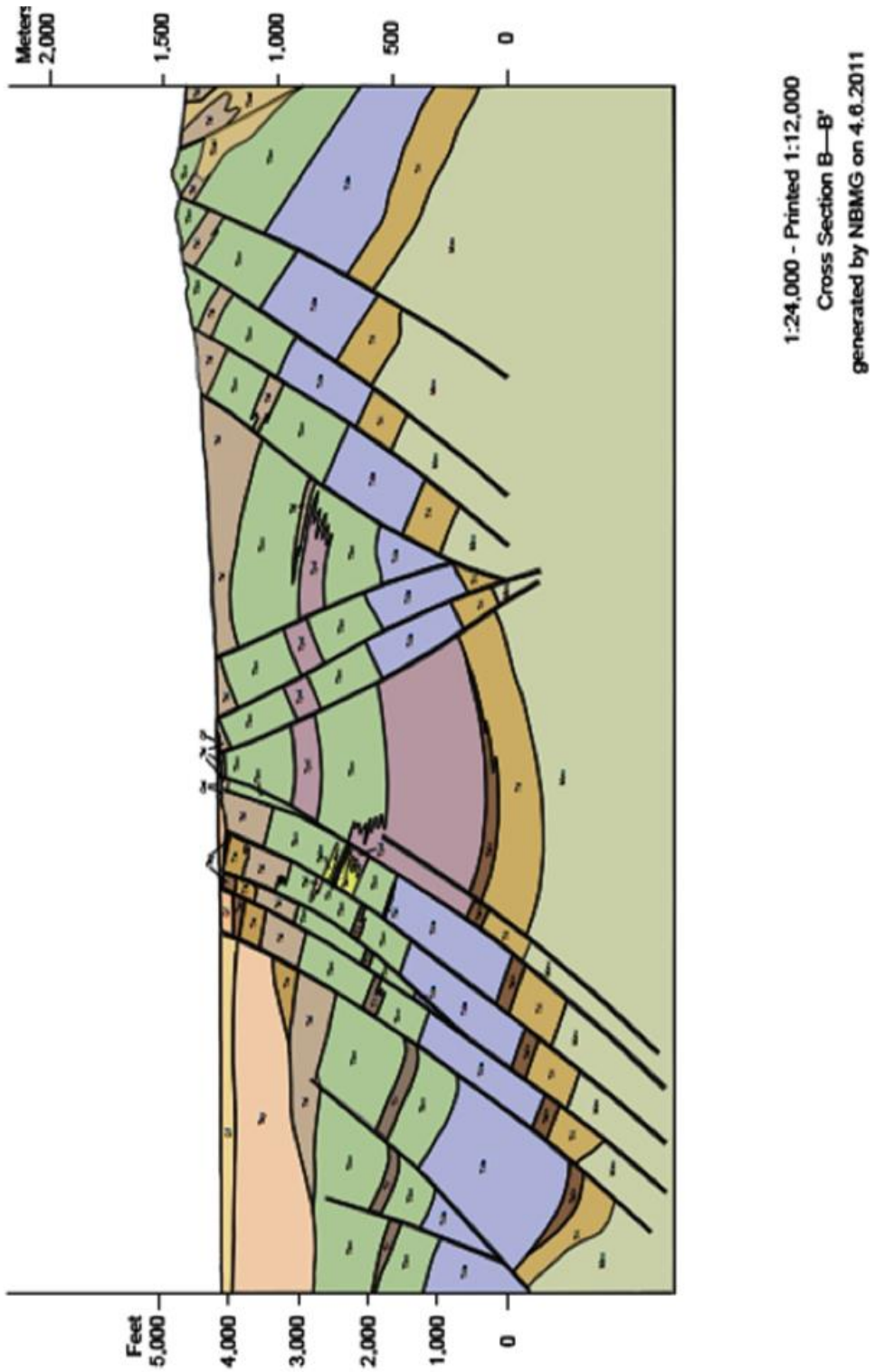

Figure 4: Cross section of the geothermal field. (Faulds, Moeck et al. 2010)

Qsi	Sinter deposits
Qf	Alluvial
Tsy	Sandstone, conglomerate, and tuffaceous sediments
Tsl	Lacustrine sediments (diatomite, siltstone, minor limestone and sandstone)
Tls	Limestone (commonly with abundant tufa)
Tabo	Altered aphanitic basalt flows and breccias
Tbo	Older, generally aphanitic basalt flows and breccias
Tbai	Basaltic andesite intrusions
Tpd	Porphyritic dacite to rhyodacite flows and domes
Tlr	Rhyolite lavas and lesser tuffs
Tda	Andesite-dacite lavas
Tslo	Older lacustrine sediments intercalcated with basalt, andesite, dacite, and rhyolite flows
Trt	Mesozoic granites and metamorphic rocks, undivided
Mzu	Oligocene ash-flow tuffs

Table 3: Lithologic descriptions (Faulds 2011)

1.1.3 Geothermal Energy

Geothermal energy is thermal energy generated the interior of the Earth and stored in the subsurface. This energy heats the groundwater to high temperatures, particularly in volcanically active regions in the subsurface. Water can be heated to temperatures of more than 200°C. Cool water recharges to groundwater is heated up, and rises to the surface discharging at hot springs. The steam from these heated waters are collected to generate energy. An enhanced geothermal sequence (EGS) uses at least two separate wells penetrating the geothermal field, at least one injection well pumping surface water deep into the warm underground and at least one production well collecting the injected, warmed water to produce energy (Figure 5).

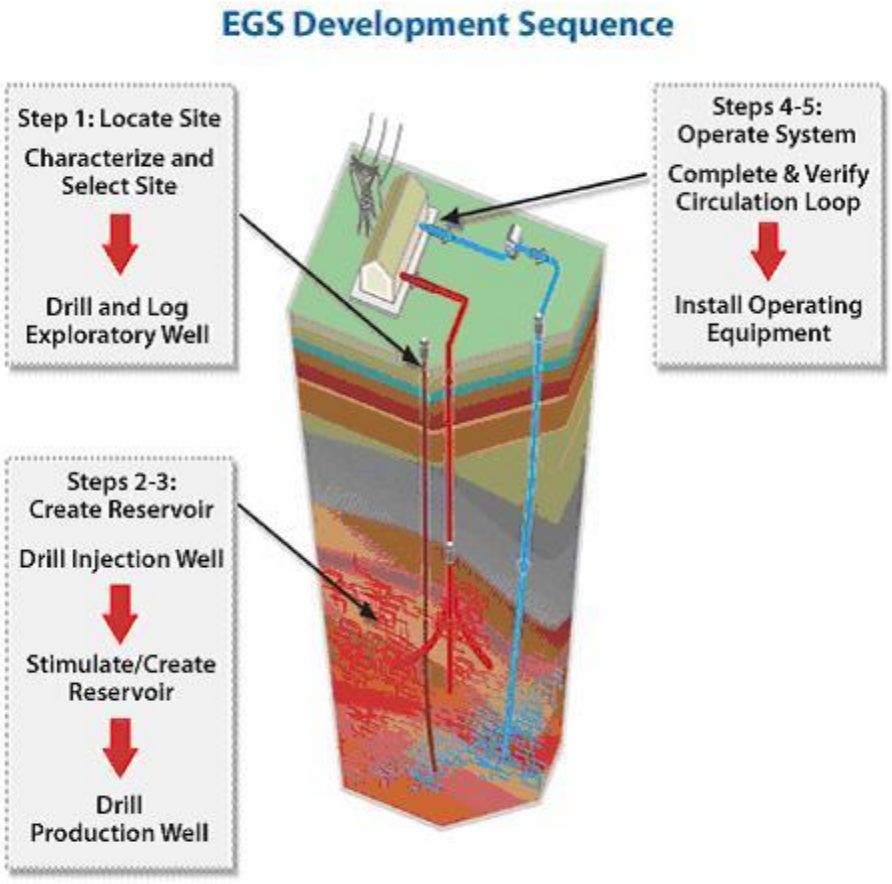

Figure 5: Enhanced Geothermal system in which water is injected (blue well) and recollected for use of energy generation (red well). Image Source: ProQuest <http://www.csa.com/discoveryguides/geothermal/review3.php>

Geothermal energy is a useful natural resource for eligible regions (Figure 6). Providing that the subsurface temperature of a region is great enough, EGS is an extremely effective and clean method of generating electricity and hence combating our dependence on fossil fuels. While geothermal energy is not feasible in much of the United States, much of the western USA is capable of harnessing geothermal energy resources.

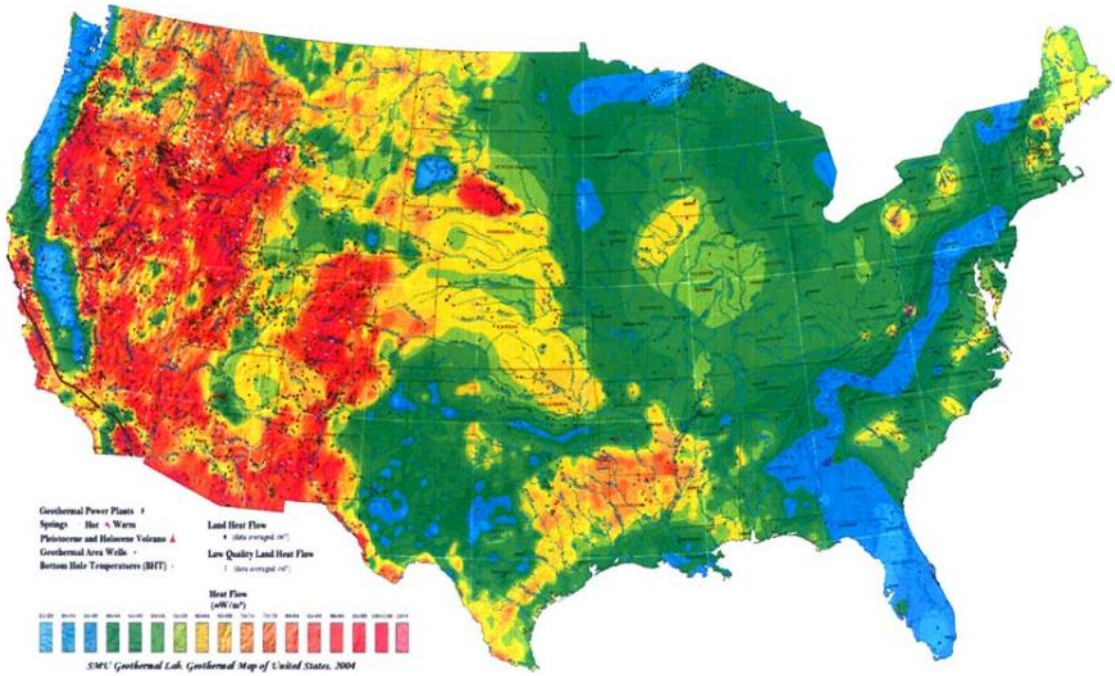

Figure 6: Heat flow map of the USA. Subset of Geothermal map of North America (Blackwell and Richards, 2004)

1.2 DATA COLLECTION

1.2.1 Ultrasonic-Waveforms and Velocities

All data was collected at the National Energy Technology Lab (NETL) of the United States Department of Energy (DOE). Using the Autolab 1500 device (Figure 7), from the New England Research Group (NER) ultrasonic velocity measurements including wave velocity and

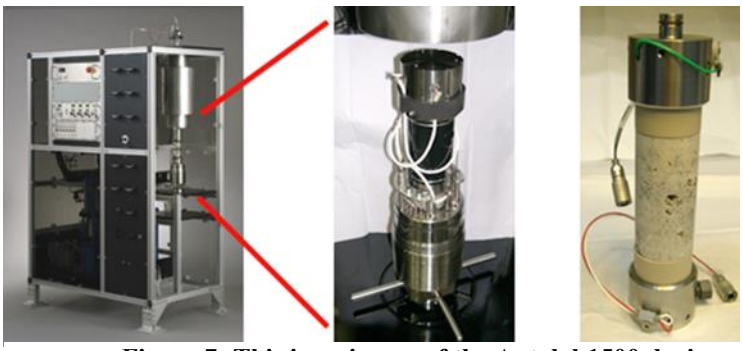

Figure 7: This is an image of the Autolab1500 device with a zoomed in view of the core holder where the rock core sample is placed and loaded into the device.

waveforms. The Autolab 1500 device is capable of triaxial compression and temperature control, allowing accurate control of the pore pressure, confining pressure, and temperature experienced by the loaded rock core sample. This experimental control allows for simulation of conditions consistent with field conditions. The Autolab 1500 device is also equipped with two ultrasonic wave transducers, which generate ultrasonic primary and secondary seismic waves in one end of the core sample and records waves at the other end. This waveform, as well as sampling frequency, wave velocity, and physical characteristics of the rock core sample such as Young' modulus and Poisson's ratio, are recorded. We tested several different rock types including Rhyolite, Carbonate and an aluminum reference core. Measurements were taken at various different pressures (0.1-50 MPa) and temperatures (20-80° C). The cores were tested both dry and with various pore-filling fluids (water, CO_2, and oil/CO_2 mix).

1.2.2 Porosity

Porosity is a fundamental physical parameter, the amount of pore space within a rock, and is typically quantified as a percent of total rock volume. Porosity measurements for all cores were made in the Core Flow Lab at NETL of the DOE. All cores were tested dry and kept in a controlled environment with humidity below 10% for several days prior to measurements. Porosity measurements were made using the TEMCO helium porosimeter (Figure 8).

Figure 8: TEMCO helium porosimeter, HP-401

Porosities were measured at least in triplicate and averaged. Porosity measurements were made at relatively low pressures, i.e. a confining pressure and pore pressure at about 100 psi. The helium porosimeter measures the porosity of a rock core, loaded into the sample chamber, by using helium gas to penetrate the pores of the rock core sample in a closed system. These porosity values may not accurately represent porosity at depth, as compliant pores would be closed under lithostatic pressure; however these measurements are a good characterization of system porosity.

1.2.3 Permeability

All Permeability data was collected at the National Energy Technology Lab (NETL) of the United States Department of Energy (DOE), using the Autolab 1500 device (Figure 7). Utilizing the core flow apparatus of the Autolab 1500 device and processing software from the New England Research group permeability was calculated using a pressure transient. This method works by inducing and recording a pressure spike or sine wave at one end of the core

sample (the upstream) and recording pressure wave at the other end of the core (the downstream) (Siriwardane, Haljasmaa et al. 2009). Characterizing travel of induced pressure waves travel through the core (i.e. how the upstream pressure response differs from the downstream) provides insight into fluid flow through the cores. The permeability of each sample was tested using both the pressure spike and sine wave to assure accuracy of measurements. Permeability is calculated as follows:

$$\left(\frac{k}{\eta}\right)\frac{\partial^2 p}{\partial x^2} = (\alpha + \varphi\beta)\frac{\partial p}{\partial t} \qquad \textbf{Equation 1}$$

(Siriwardane, Haljasmaa et al. 2009)

Where k is the permeability, η is the dynamic viscosity of the pore fluid (inert argon gas in our case), t is time, x is the axial coordinate (the origin located at the upstream of the core), α is the pore volume compressibility, β is the adiabatic compressibility of the pore fluid, and φ is the porosity of the sample (Siriwardane, Haljasmaa et al. 2009). The upstream boundary condition is as follows

$$p(0,t) = p_0(t) \qquad \textbf{Equation 2}$$

$p_0(t)$ is the pressure pulse which we send through the core. The downstream boundary condition is as follows

$$\frac{\partial p(L,t)}{\partial t} = \frac{Q}{\beta V}$$ **Equation 3**

Where L is the length of the sample, Q is the flow rate through the sample, and V is the downstream volume (Siriwardane, Haljasmaa et al. 2009). This set of equations is then solved numerically to determine the permeability (k) of the sample.

2.0 PETROPHYSICAL ANALYSIS OF THE GEOTHERMAL SITE

This research performs a petrophysical analysis, of the geothermal field core samples. Seventeen rock core samples were collected from the geothermal field at various depths ranging between 3100 ft to 4900 ft. This analysis clarifies how fluids (water in particular) will flow in a geothermal well, improving the efficiency of the well.

2.1.1 Hydraulic Conductivity

The hydraulic conductivity of rock is its ability to transmit water. The hydraulic conductivity (K) is calculated using the following relation.

$$K = \frac{k\rho g}{\mu}$$ **Equation 4**

(Bear 1972)

Where k is the permeability of the sample, ρ is the density of water, g is the gravitational acceleration, and μ is the viscosity of water. In this analysis we focus on the hydraulic conductivity of the geothermal samples, as water is commonly used as a geothermal fluid in the fields geothermal systems. Because of the high temperatures in the geothermal well we use the viscosity of water at high temperatures are used. Keslin (1978) describes the viscosity of water

at 150°C to be approximately $1.8146*10^{-4}$ Pa s (Keslin 1978) allowing us to calculate K for temperatures similar to the subsurface of the geothermal field.

2.2 GEOTHERMAL CORE ANALYSIS

Petrophysical measurements including porosity and bulk density were made for all rhyolite cores. Permeability measurements for 6 of the 17 sample cores have been measured thus far. Rock cores have a wide range of porosity values ranging from 0.47% to 18.16% with an average value of 6.75%. Therefore we calculated very low values of hydraulic conductivities.

Relationships among relevant core data including porosity, hydraulic conductivity, and depth were examined. Core depths can be broken up into four different sections, two of high porosity and two of lower porosity (Figure 9). We define the lower porosity bound (which is depicted as a red dashed line) to be ~4% core porosity. Low porosity depth regions have no core samples with porosity above this threshold and high porosity regions tend to have core porosities well above 4%.

We can understand that certain depths will be, due to higher rock porosity, more apt to holding water. That is to say our high porosity depth regions (~3100-3650ft and ~4200-4900ft) have a higher hydraulic storativity and could therefore be a more efficient at holding fluids and retrieving thermal energy.

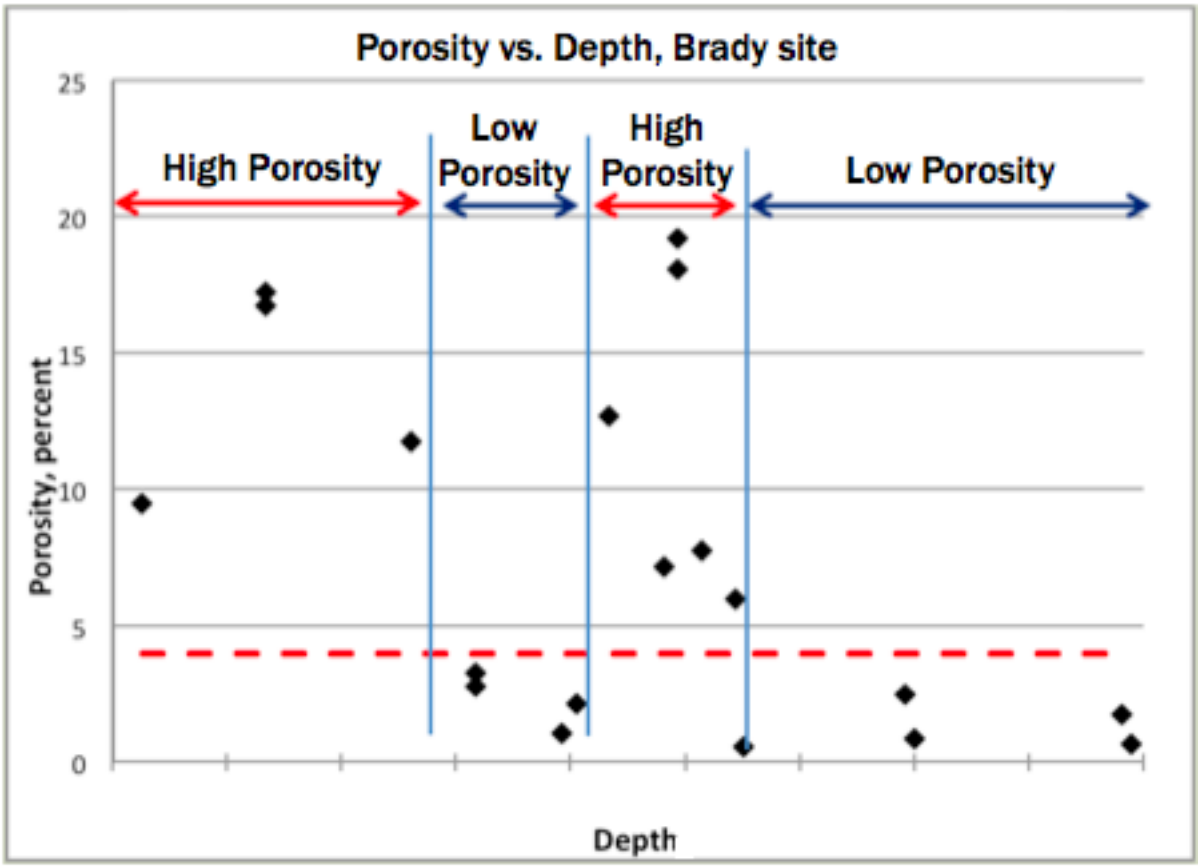

Figure 9: Plot contains porosity vs. depth. Data is broken into four different zones, two of high porosity and two of low porosity.

Figure 10 below displays the core hydraulic conductivity vs. depth, where hydraulic conductivity is on a logarithmic scale. As can be seen, the hydraulic conductivity of the measured cores seems to follow a similar relationship as for core porosity vs. depth. Although all hydraulic conductivities are very low (as is to be expected for an igneous rock), we see regions of relatively high values of K and regions with lower values of K. These regions correspond to the same depth regions highlighted in Figure 9.

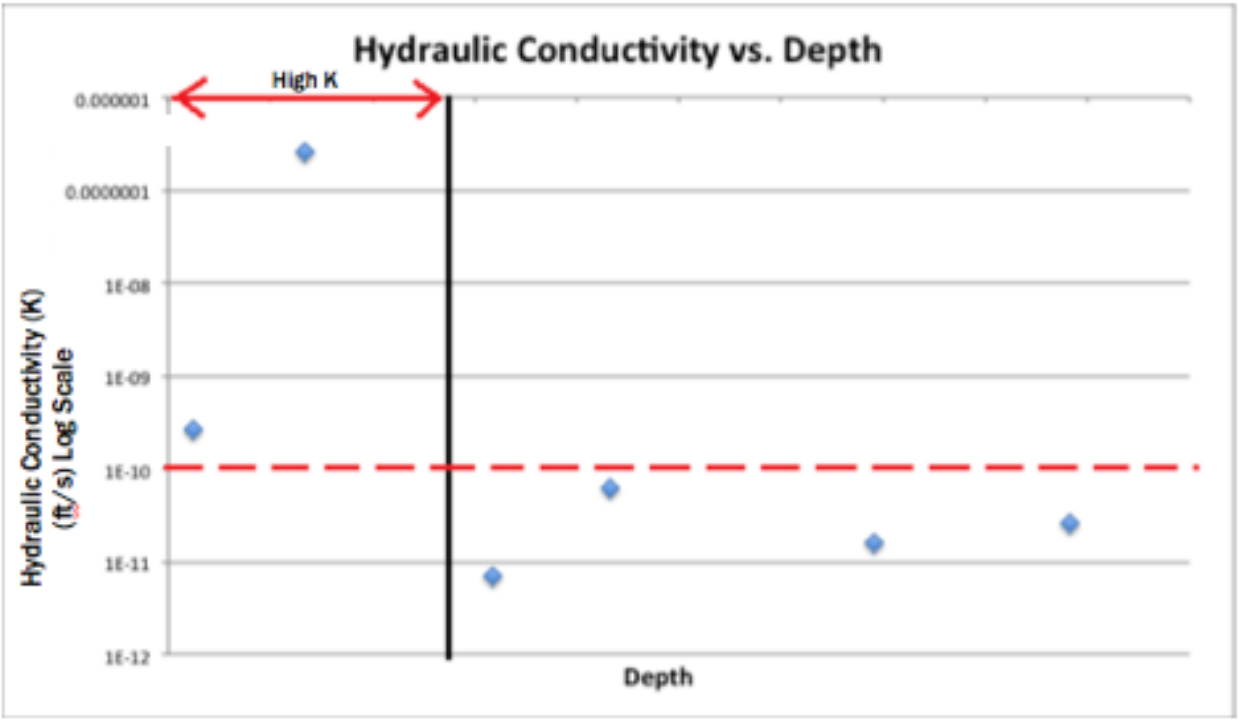

Figure 10: Plot displays hydraulic conductivity of cores vs. depth

2.3 GEOTHERMAL SITE CONCLUSIONS

The geothermal field is an extremely valuable energy resource that is and will continue to be utilized for its geothermal resources. Our analysis of the porosity, permeability, and hydraulic conductivity of the cores taken from the geothermal field has shed light onto the hydraulic nature of the region. We are able to conclude that there are depth regions of higher and lower porosity and hydraulic conductivity. These regions display the highest value of porosity, which will allow the rock to hold as much water as possible, and the highest hydraulic conductivity, which will allow this water to efficiently be transmitted through the rock from the injection well and to the production well hence maximizing the efficiency of our enhanced geothermal system.

Of course, we must remember that at these depths the porosity of the rock will be lower due to the intense lithostatic pressures closing the compliant pores. Further, it is important to note that even though there are regions of higher hydraulic conductivity, these values are still very low. We should expect fractures in the field to conduct water with much more efficiency than just the solid rock, especially if the well is being subjected to hydraulic fracturing to increase productivity and efficiency.

Overall the study of cores has provided us with valuable information as to the nature of the field, yet the study is incomplete. The remaining eleven cores must be tested for their permeability in order to gain a fuller understanding of the hydraulic nature of the region. Upon completion of the final measurements the resolution of our hydraulic stratigraphy will be greatly increased and we will be able have a much better understanding of the region providing us with better insight into how to design enhanced geothermal systems in the geothermal field.

3.0 PETROPHYSICAL MODEL: λρ-μρ

Understanding the physical nature of rock is extremely important from both engineering and geophysical standpoints. A clearer understanding of the physical structure of rock will improve interpretation of how the rock responds to stress, strain, and how it interacts with seismic waves particularly wave velocities and the reflectivity between two rock layers. As such, a better understanding of the elastic nature of rock allows us to gain insight into wave propagation and reflectivity at boundaries.

The importance of understanding the physical nature of rock is clear, but how can we effectively study and quantify the physical nature of rock? Approaches using the Lamé elastic moduli (λ representing the rigidity and μ representing pure incompressibility of the material (Goodway 2010)) are typical. Lamé used these two moduli, dubbed the Lamé parameters, to formulate a version of Hooke's law relating stress and strain in a 3D medium (Equation 5) (Goodway 2010).

$$s_{ij} = l d_{ij} e_v + 2m e_{ij} \qquad \textbf{Equation 5}$$

Where, σ is the stress, μ and λ are the Lamé parameters.

The elastic moduli (including the Lamé parameters) are ratios of applied stresses and the resulting strain in linear elastic materials. These rock moduli indicate how the rock responds to applied stress. Any two of the Lamé parameters allows complete fully understanding the stress and strain relations of a material (Mavko, Mukerji et al. 2009). With any two known moduli we

are able to calculate all other parameters using the relations displayed in **Table 4**. A brief description of the elastic moduli is given in the appendix Section 1.01(a)(i)A.1.

Sought / Given	E	k	M	λ	μ	ν
E, k	—	—	$\frac{3k(3k+E)}{9k-E}$	$\frac{3k(3k-E)}{9k-E}$	$\frac{3kE}{9k-E}$	$\frac{1}{2}-\frac{E}{6k}$
E, M	—	$\frac{3M-E+w_1}{6}$	—	$\frac{M-E+w_1}{4}$	$\frac{3M+E-w_1}{8}$	$\frac{E-M+w_1}{4M}$
E, λ	—	$\frac{E+3\lambda+w_2}{6}$	$\frac{E-\lambda+w_2}{2}$	—	$\frac{E-3\lambda+w_2}{4}$	$\frac{w_2-E-\lambda}{4\lambda}$
E, μ	—	$\frac{\mu E}{3(3\mu-E)}$	$\frac{\mu(4\mu-E)}{3\mu-E}$	$\frac{\mu(E-2\mu)}{3\mu-E}$	—	$\frac{E}{2\mu}-1$
E, ν	—	$\frac{E}{3(1-2\nu)}$	$\frac{(1-\nu)E}{(1+\nu)(1-2\nu)}$	$\frac{\nu E}{(1+\nu)(1-2\nu)}$	$\frac{E}{2(1+\nu)}$	—
k, M	$\frac{9k(M-k)}{M+3k}$	—	—	$\frac{3k-M}{2}$	$\frac{3}{4}(M-k)$	$\frac{3k-M}{3k+M}$
k, λ	$\frac{9k(k-\lambda)}{3k-\lambda}$	—	$3k-2\lambda$	—	$\frac{3}{2}(k-\lambda)$	$\frac{\lambda}{3k-\lambda}$
k, μ	$\frac{9k\mu}{3k+\mu}$	—	$k+\frac{4}{3}\mu$	$k-\frac{2}{3}\mu$	—	$\frac{3k-2\mu}{2(3k+\mu)}$
k, ν	$3k(1-2\nu)$	—	$\frac{3k(1-\nu)}{1+\nu}$	$\frac{3k\nu}{1+\nu}$	$\frac{3k(1-2\nu)}{2(1+\nu)}$	—
M, λ	$\frac{(M+2\lambda)(M-\lambda)}{M+\lambda}$	$\frac{M+2\lambda}{3}$	—	—	$\frac{M-\lambda}{2}$	$\frac{\lambda}{M+\lambda}$
M, μ	$\frac{\mu(3M-4\mu)}{M-\mu}$	$M-\frac{4}{3}\mu$	—	$M-2\mu$	—	$\frac{M-2\mu}{2(M-\mu)}$
M, ν	$\frac{(1-2\nu)(1+\nu)M}{1-\nu}$	$\frac{(1+\nu)M}{3(1-\nu)}$	—	$\frac{\nu M}{1-\nu}$	$\frac{(1-2\nu)M}{2(1-\nu)}$	—
λ, μ	$\frac{\mu(3\lambda+2\mu)}{\lambda+\mu}$	$\lambda+\frac{2}{3}\mu$	$\lambda+2\mu$	—	—	$\frac{\lambda}{2(\lambda+\mu)}$
λ, ν	$\frac{\lambda(1+\nu)(1-2\nu)}{\nu}$	$\frac{\lambda(1+\nu)}{3\nu}$	$\frac{\lambda(1-\nu)}{\nu}$	—	$\frac{\lambda(1-2\nu)}{2\nu}$	—
μ, ν	$2\mu(1+\nu)$	$\frac{2\mu(1+\nu)}{3(1-2\nu)}$	$\frac{2\mu(1-\nu)}{1-2\nu}$	$\frac{2\mu\nu}{1-2\nu}$	—	—

Table 4: Displays the relationships between the elastic moduli of homogeneous, isometric materials. (Gassmann 1951)

How do these elastic moduli relate to the seismic wave propagation? The different directions of particle motion in shearing and compressional waves induce different stress and strain relationships in to the rock (Figure 11). Further elastic wave propagation is directly dependent on the moduli of the medium through which it travels. The velocity of seismic waves

traveling through a rock or other physical medium can be calculated by Equation 6 and Equation 7 for the P and S wave velocities respectively.

$$V_p = \sqrt{\frac{l + 2m}{r}}$$ **Equation 6**

$$V_s = \sqrt{\frac{m}{r}}$$ **Equation 7**

Where V_p and V_s are the wave velocities, ρ is the density of the medium, λ is Lamé's first parameter, and μ is Lamé's second parameter (shear modulus). Note that λ+2μ is defined as the p-wave modulus M. Wave velocity is inversely proportional to the square root of the density of the material and directly proportional to the square root of the moduli parameters.

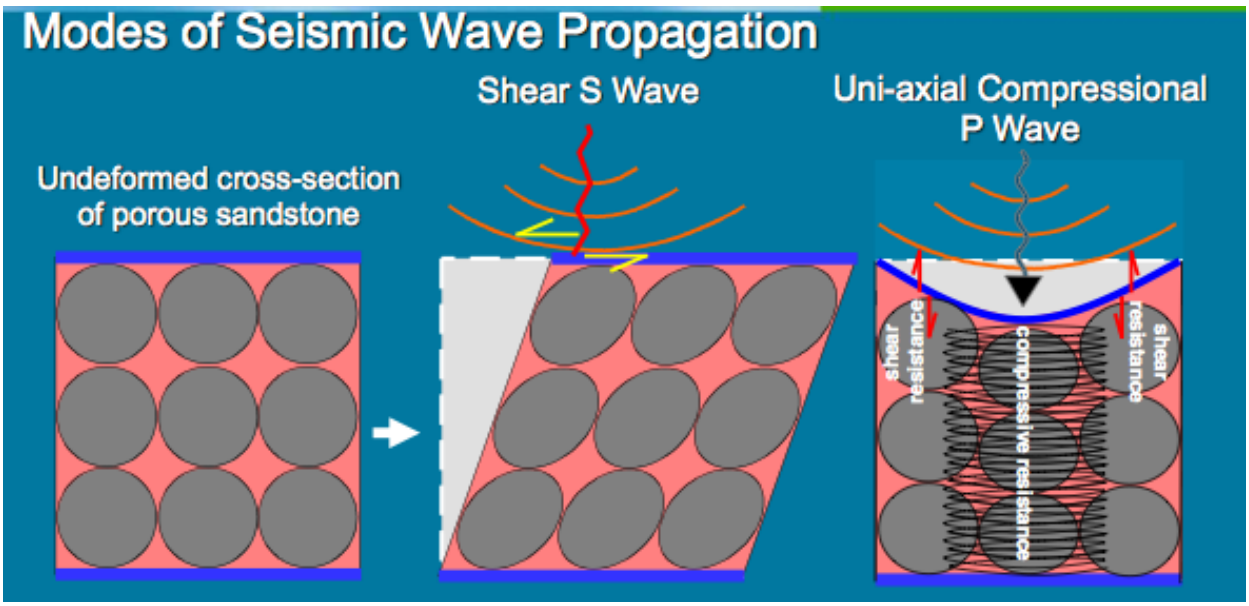

Figure 11: Cartoon illustration depicting how P and S seismic waves propagate through rock material and induce different stress strain relationships due to the direction of particle oscillation of the waves. Image Source:(Goodway 2001).

3.1.1 λρ-μρ and AVO Interpretation

AVO (amplitude variation with offset) is a powerful tool for imaging, interpreting and understanding the subsurface. Through the stacking of AVO analysis of seismic data, a robust seismic image of the subsurface with high signal to noise ratio is achieved and from studying how the amplitude changes in a reflected seismic wave due to changes when varied angle of incidence. As an incident seismic wave hits a boundary between two different rock layers, it will decompose into reflected and transmitted P and S wave components (Figure 12).

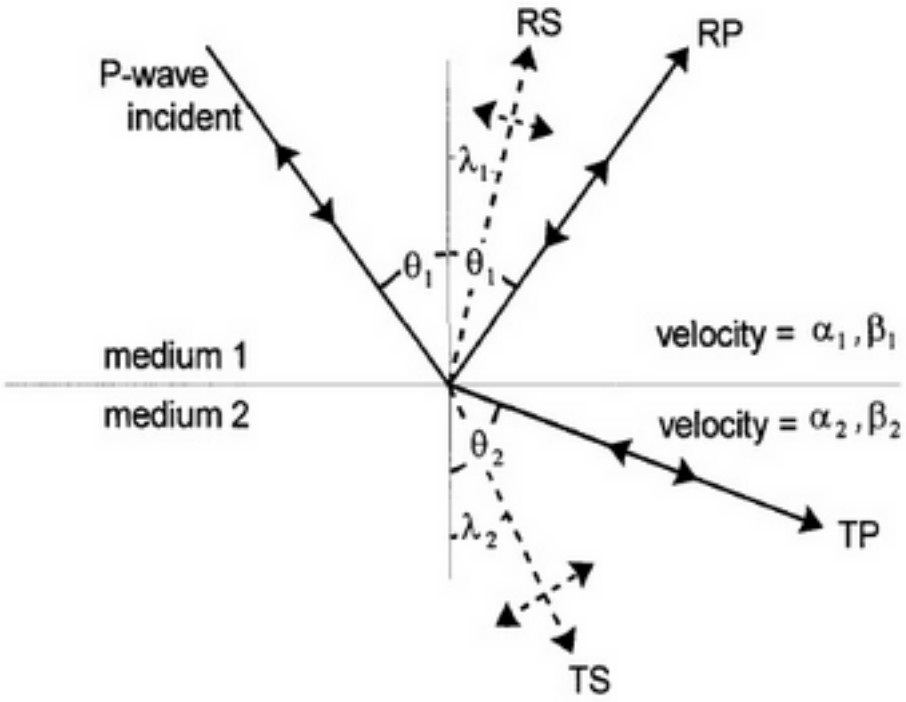

Figure 12: Displays an incident P wave at angle Θ_1 as well as reflected and transmitted P and S waves. Equation displayed depicts the relationship between wave velocities in each medium and angles of reflection and refraction via Snell's law. (Çoruh 2004)

The amplitude of these reflected and transmitted waves is dependent on the angle of incidence as well as the elastic properties of the two rock layers, including the P and S-wave acoustic impedances. Both the P and S-wave acoustic impedances are directly related to the Lamé parameters and in particular λρ and μρ. The relationship between elastic moduli and acoustic impedance is given by the following relationships (Goodway 2001).

$$I_p^2 = l r + 2 m r \qquad \textbf{Equation 8}$$

$$I_s^2 = m r \qquad \textbf{Equation 9}$$

Where I_p and I_s are the P and S-wave acoustic impedances, ρ is density, and λ and μ are the Lamé parameters. Equation 9 and Equation 15 make it clear that acoustic impedance of rock is related to the elastic properties of a rock through a simple quadratic relationship.

The partitioning of reflected, transmitted, and converted energy of an incident seismic wave is described by the Zoeppritz equations (Equation 10-Equation 13) (Çoruh 2004). Where A and B represents the wave amplitude in each rock layer, θ and λ are angles of seismic rays relative to the boundary normal (Figure 12).

$$A_1 \cos q_1 - B_1 \sin l_1 + A_2 \cos q_2 + B_2 \sin l_2 = A_0 \cos q_1 \qquad \textbf{Equation 10}$$

$$A_1 \sin q_1 + B_1 \cos l_1 - A_2 \sin q_2 + B_2 \cos l_2 = - A_0 \sin q_1 \qquad \textbf{Equation 11}$$

(Çoruh 2004)

The Boundary conditions are as follows:

$$A_1 Z_1 \cos 2 l_1 - B_1 W_1 \sin 2 l_1 - A_2 Z_2 \cos 2 l_2 - B_2 W_2 \sin 2 l_2 = - A_0 r_1 l_1 \cos 2 l_1 \qquad \textbf{Equation 12}$$

$$A_1 \frac{b_1}{a_1} W_1 + B_1 W_1 \cos 2\theta_1 + A_2 \frac{b_2}{a_2} W_2 \cos 2\theta_2 = A_0 \frac{b_1}{a_1} W_1 \sin 2\varphi_1 \quad \textbf{Equation 13}$$

(Çoruh 2004)

Due to the complexity of the Zoeppritz equations, an approximation such as the Shuey two and three term approximations is often used ((Shuey 1985, Castagna and Swan 1997)). The Shuey two term approximation is shown in Equation 14

$$R(\theta) = A + B\sin^2(\theta) + ... \quad \textbf{Equation 14}$$

(Castagna and Swan 1997)

Where R is the reflection coefficient, θ is the angle of incidence, A is the AVO intercept, and B is the AVO gradient. The AVO intercept (A) can be thought of as the amplitude of the signal at a normal angle of incidence, and the AVO gradient (B) is a measure of amplitude variation with offset angle ((Castagna and Swan 1997)).

When analyzing AVO data it is important to systematically classify observed AVO anomalies. A commonly used four-class system (classes I, II, III, and IV) for classifying and interpreting AVO anomalies is based on the relative acoustic impedances of the two rock layers making up the observed reflection boundary (Figure 14). Through examination of the cross plot of the AVO gradient (B) vs. the AVO intercept (A) we classify the AVO anomaly based off the quadrant/location of a reflection event on this cross plot (Figure 13).

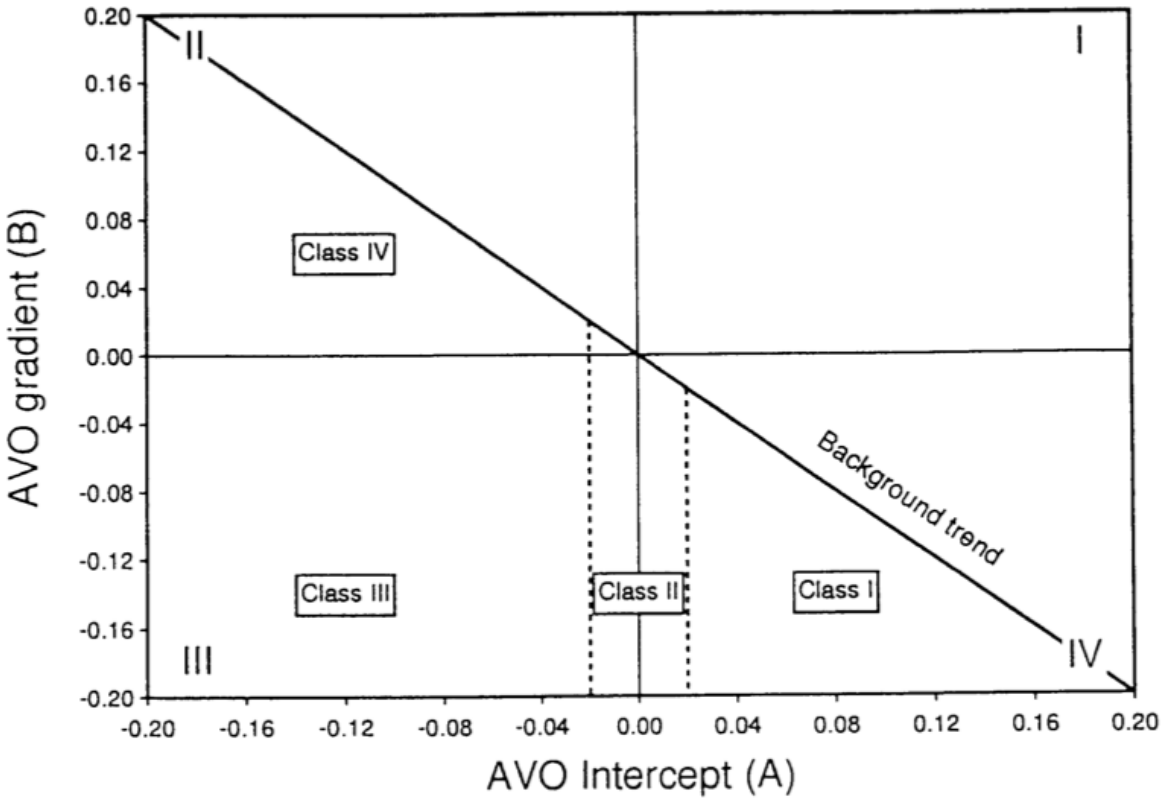

Figure 13: AVO classifications from cross plot of B vs. A. (Castagna and Swan 1997)

Class	Relative Impedance	Quadrant	A	B	Amplitude vs. Offset
I	Higher than overlying unit	IV	+	-	Decreases
II	About the same as the overlying unit	II, III, or IV	+ or -	-	Increase or decrease; may change sign
III	Lower than overlying unit	III	-	-	Increases
IV	Lower than overlying unit	II	-	+	Decreases

Figure 14: Description f AVO classes (Castagna, 1997).

Analysis and interpretation of AVO data is complicated and somewhat ambiguous for reasons as described by Castagna, Swan, and Foster (1998), quoting directly from their paper: (1) A lack of intuitive "feel" on the part of the interpreter for the physical significance of the B term:

(2) The confounding effects of the seismic wavelet: (3) Scatter caused by poor seismic data quality: (4) Nonpetrophysical influences on the extracted seismic parameters A and B.

The ambiguities as described by Castagna, Swan, and Foster (1998) hinder our ability to interpret AVO data. By utilizing seismic inversion techniques we are able to decompose angle gathers into density and the Lamé parameters (Figure 15). By decomposing reflection data into the fundamental parameterization of the Lamé parameters, we are able to extract information from seismic data including wire line log data and seismic surveys without the complications of non-fundamental formulations (Goodway 2010). Observations made and information extracted from measurements inverted into the fundamental elastic properties removes ambiguity of other methods such as examination of the AVO terms A and B (Goodway 2010).

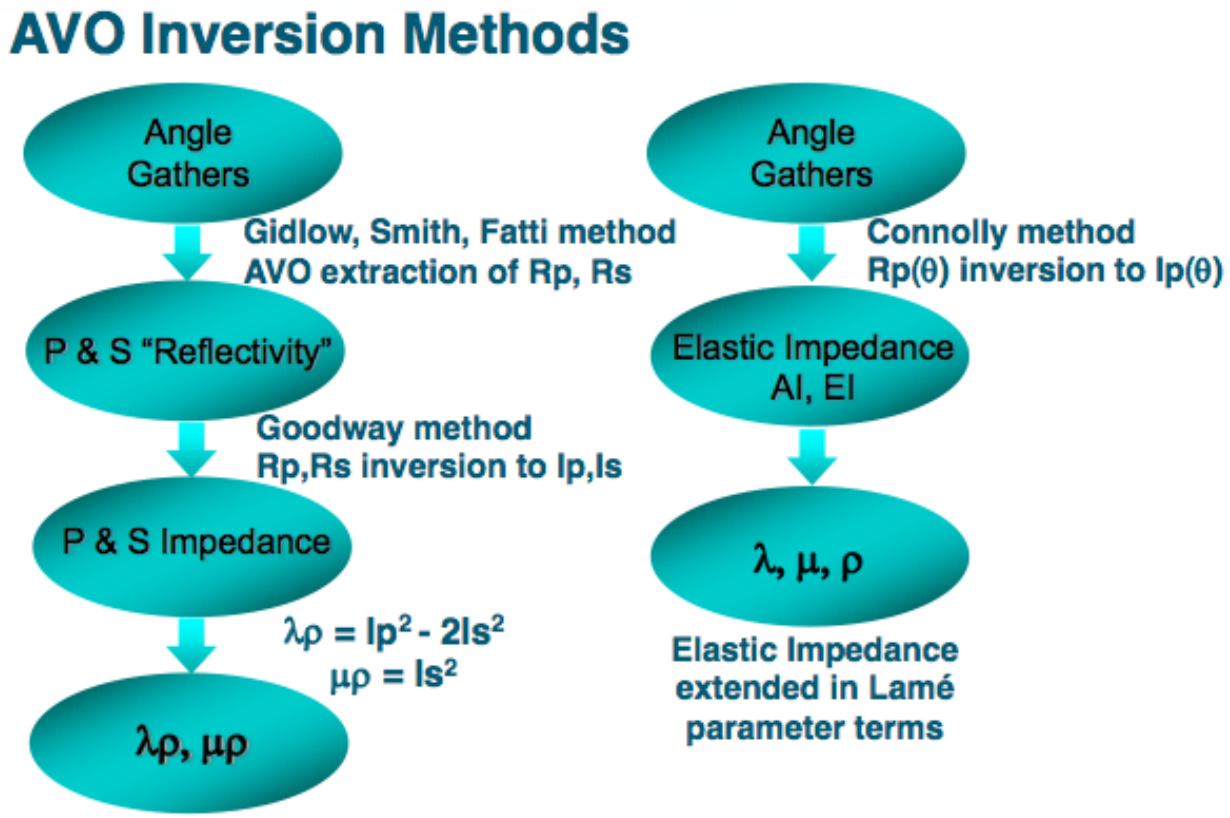

Figure 15: Flow depicting how AVO analysis methods beginning with angle gathers decomposes into λρ-μρ. (Goodway 2010)

3.2 ROCK PHYSICS MEASUREMENTS

3.2.1 Data Collection and Methodology

Wave velocity and rock moduli data was collected for 20 separate rock cores. Seventeen rhyolite samples from the geothermal field in Nevada, 2 carbonate samples (tested with various pore-filling fluids including deionized water and CO_2), as well as 1 carbonate core tested dry. Ultrasonic velocity measurements were taken using the Autolab 1500 device of the New England Research group (Figure 7) following the methodology outlined in section1.2.1. After both P and S wave velocities were recorded, the elastic moduli were calculated using Equation 6 and Equation 7 and recorded. As mentioned in previous sections, 1.2.2 and 1.2.1, porosity measurements were taken using the helium porosimeter (Figure 8).

In our analysis of the core moduli, we choose to examine the elastic properties data in $\lambda\rho$-$\mu\rho$ space (Lamé's first parameter and the shear modulus of the rock times the dry bulk density of the rock). We chose to analyze the data in this space to explore the elastic nature of the rock, as $\lambda\rho$-$\mu\rho$ are closely related to acoustic impedance (Equation 9 and Equation 15) and provide insight into AVO (Goodway 2010). Wave velocity and other relevant moduli cross plots, such as Young's Modulus vs. Poisson's ratio for rhyolite cores, are included in the Appendix Section 1.01(a)(i)A.2.

3.3 PETROPHYSICAL DATA AND RESULTS

Ultrasonic velocity as well as moduli data was collected and calculated for all rock core samples tested. Moduli data from all rock cores with varying temperatures and saturated with different fluids were compared to form a geophysical model characterizing the relationship among moduli parameters, effective pressure, temperature, pore-filling fluid, and porosity. These models were then compared with other petrophysical models.

3.3.1 λρ-μρ: Geothermal Rhyolite Core

Figure 16 below contains elastic moduli information for all rhyolite cores tested displayed in λρ-μρ space, where porosity is indicated by the color bar and the effective pressure of each measurement is indicated by the size of the point. Larger points indicate higher effective pressures and smaller points represent measurements at lower effective pressures (range of pressures is from .1 MPa to ~50MPa).

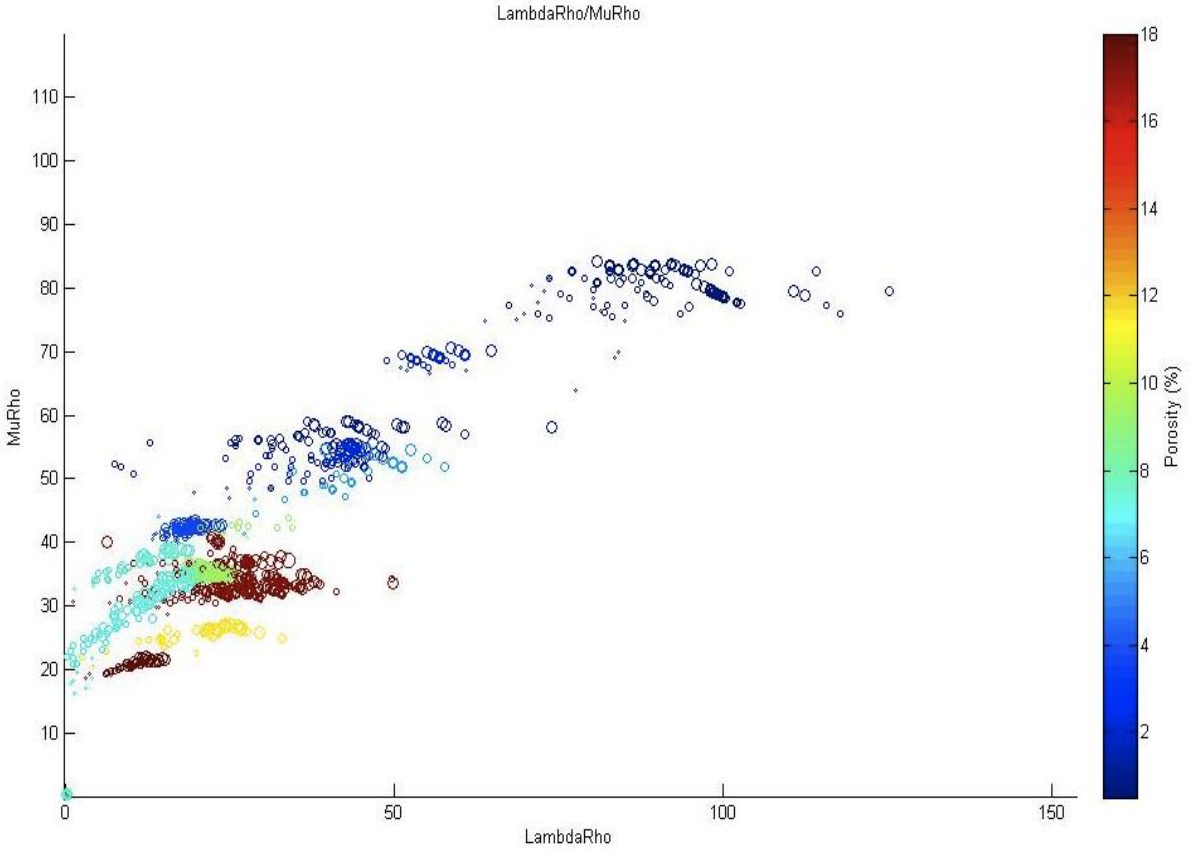

Figure 16: λρ-μρ for all rhyolite core samples.

The position of the rock core in λρ-μρ space is extremely dependent on porosity (Figure 16). We see large amounts of porosity zoning with the higher porosity samples having lover values of both λρ and μρ. We may also note that as effective pressure increases, an increase in λρ.

By examining the elastic moduli calculated from multi-temperature experiments on rhyolite rock cores, the effects of temperature on the cores elastic moduli in λρ-μρ space can be examined. Figure 17 and Figure 18 below display λρ-μρ data for multi-temperature experiments. Figure 17 depicts λρ vs. μρ vs. temperature for both the high and low porosity multi-temperature experiments.

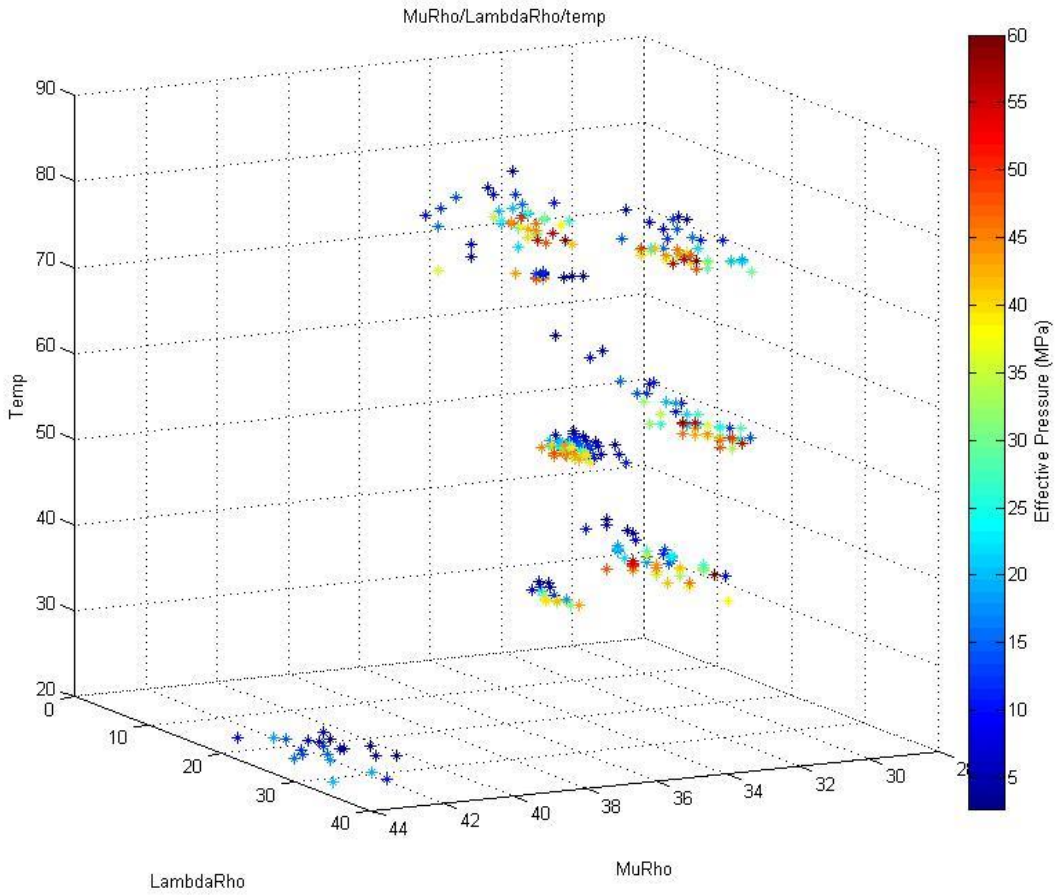

Figure 17: Plot depicts μρ vs. λρ vs. Temperature in °C for both temperature varying rhyolite cores. Color scaling indicates the effective pressure at which the measurements were taken. The effective pressure of each measurement is indicated by the color of the point and can be referenced to the color bar.

As effective pressure increases λρ increases, however, μρ is not as sensitive to pressure. It is noteworthy that as temperature increases we do see an increase in μρ. From this we can begin to conclude that λρ is pressure dependent and independent of temperature, whereas μρ seems to be somewhat dependent on temperature and relatively independent of effective pressure.

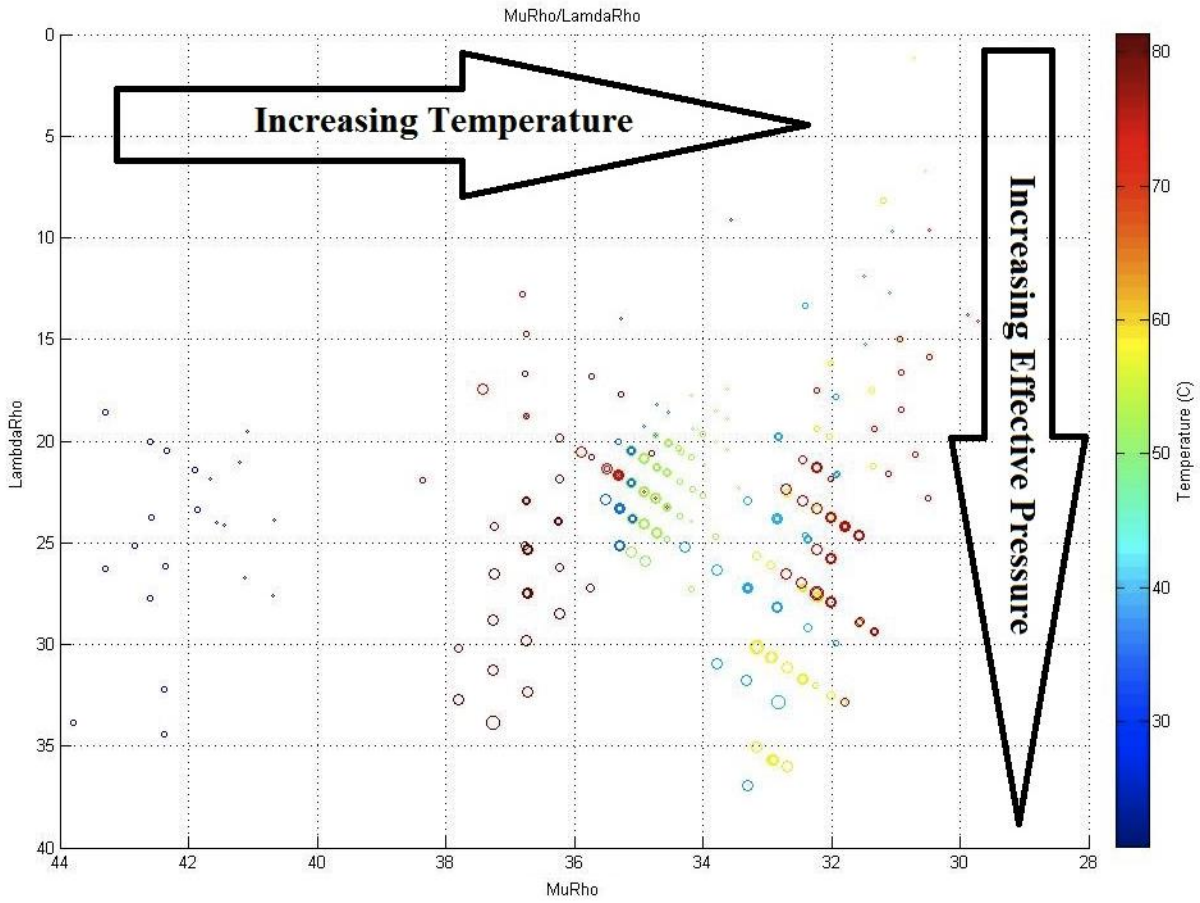

Figure 18: LambdaRho vs. MuRho for temperature variation rhyolite cores. Temperature of the experiments is indicated by color of the point and can be referenced to the color bar; larger points indicate higher effective pressures and smaller points represent measurements taken at lower effective pressures (range of pressures is from .1 MPa to ~50 MPa).

3.3.2 Vp-Vs

The relationship between the P and S seismic velocities is unique to individual lithologies making it useful in the identification of lithology and pore-filling fluids (Mavko, Mukerji et al. 2009). The V_p-V_s relationship was examined using measurements taken on 17 rhyolite core samples at varied effective pressures and temperatures. By cross-plotting the P and S seismic velocities we can relate the S seismic velocity to the P seismic velocity (Figure 19). The derived relationship between V_s and V_p by the linear fit (Equation 15)

$$V_{s1} = 0.469 * V_p + 625.64$$

Equation 15

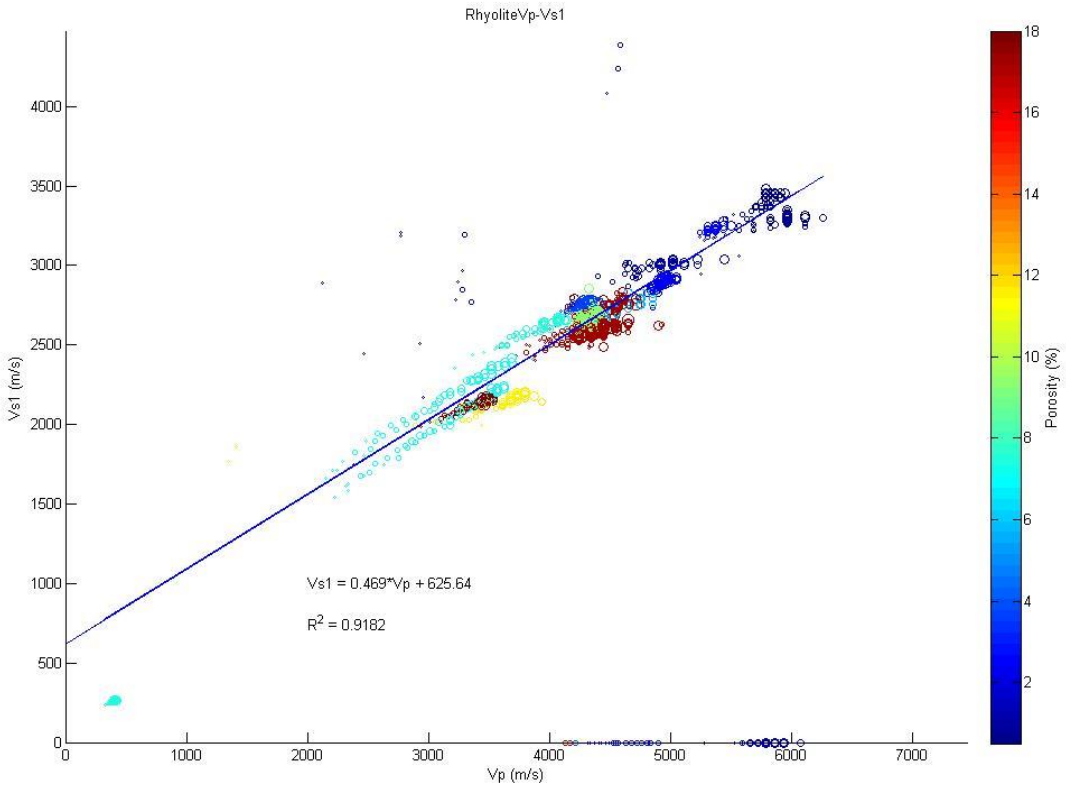

Figure 19: Displays Vp vs. Vs1 for all rhyolite core measurements. The color bar indicates the porosity of the samples and the effective pressure of each measurement is indicated by the size of the point, where small points are measurements at lower effective pressures and large points represent measurements at higher effective pressure.

As effective pressure increases the P and S wave velocities increase proportionally causing our data fall along this line. There are distinct zones of high and low porosity. The effect of porosity on the V_p-V_s relationship for rhyolite shift values along this line. The lowest porosity samples have the highest V_p and V_s values. We note that the wave velocities through cores with porosities around 8% or greater seem to group together without clear variations down the velocity line. From this we conclude, that to a first order, lower porosity rock will typically fall

further along this line, in the range of about 3000-3750 m/s for Vs and about 5000-6250 m/s for Vp. The higher porosity core samples fall, roughly, into the ranges of 1500-3000 m/s for Vs and 2250-5000 m/s for Vp.

From our results we may also conclude that changes in temperature do not seem to play a significant role in altering V_p-V_s line, porosity is far more important. Our understanding of how V_p-V_s functions not only will help us to identify rhyolite deposits in the subsurface, but to better determine some of the physical properties of the deposit such as what porosity. This knowledge of reservoir porosity could greatly aid in assessing the potential geothermal sites.

3.3.3 λρ-μρ: Permian Basin Carbonate Core

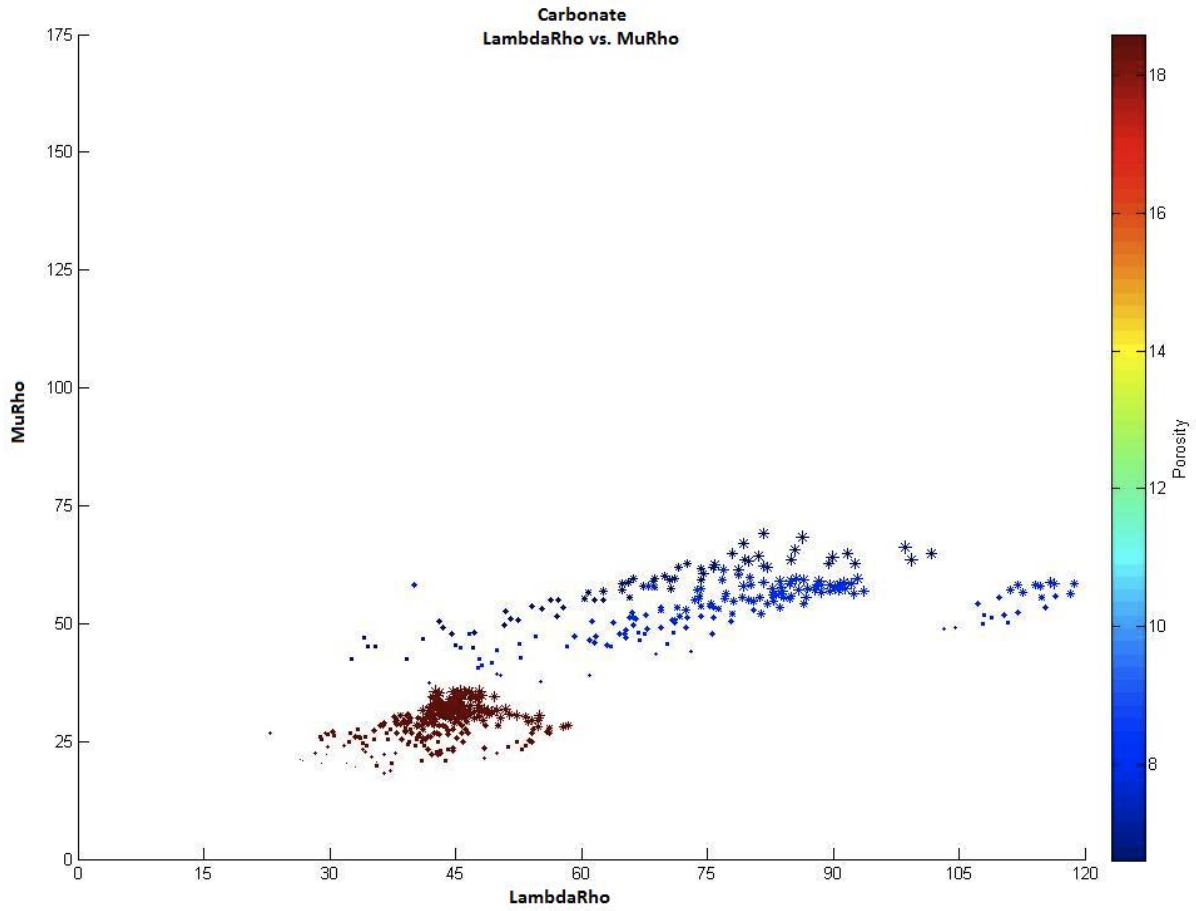

Figure 20: λρ-μρ moduli data for Carbonate cores. The samples is indicated by the color of the data point on the plot and can be referenced to the color bar, and smaller points represent measurements taken at lower effective pressures and larger points represent measurements taken at higher effective pressures ranging from 0.1-50 MPa.

Our carbonate core sample measurements (Figure 20) seem to display similar results as to rhyolite cores (Figure 16). We see distinct porosity zoning between the high and low porosity samples. Once again, lower porosity samples display both lower λρ and μρ values and λρ

increases with effective pressure. These carbonate experiments greatly agree with earlier trends observed in the rhyolite data.

Examination of the effects of pore filling fluid on the elastic moduli of rock indicates minimal effects on μρ, but distinct shifts in the value of λρ. Fluid saturation effects were tested in both a high and low porosity carbonate core samples (Figure 21 and Figure 22).

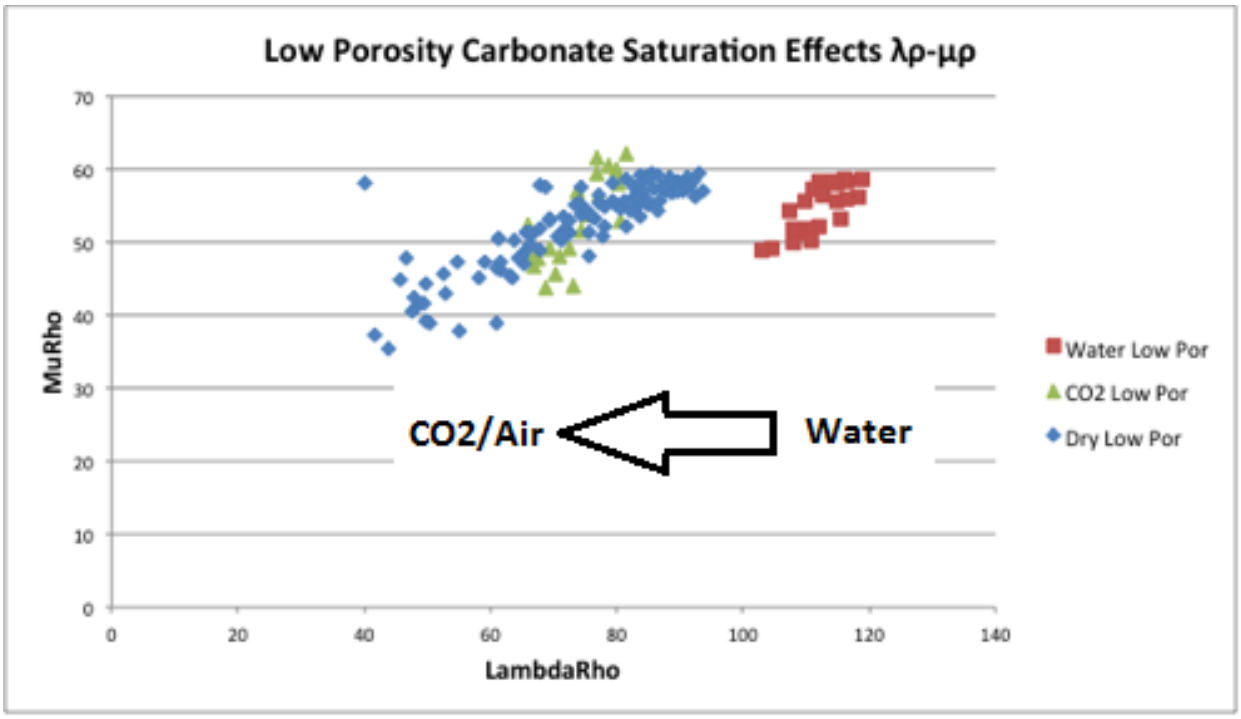

Figure 21: Fluid effects on the Elastic moduli of low porosity carbonate samples.

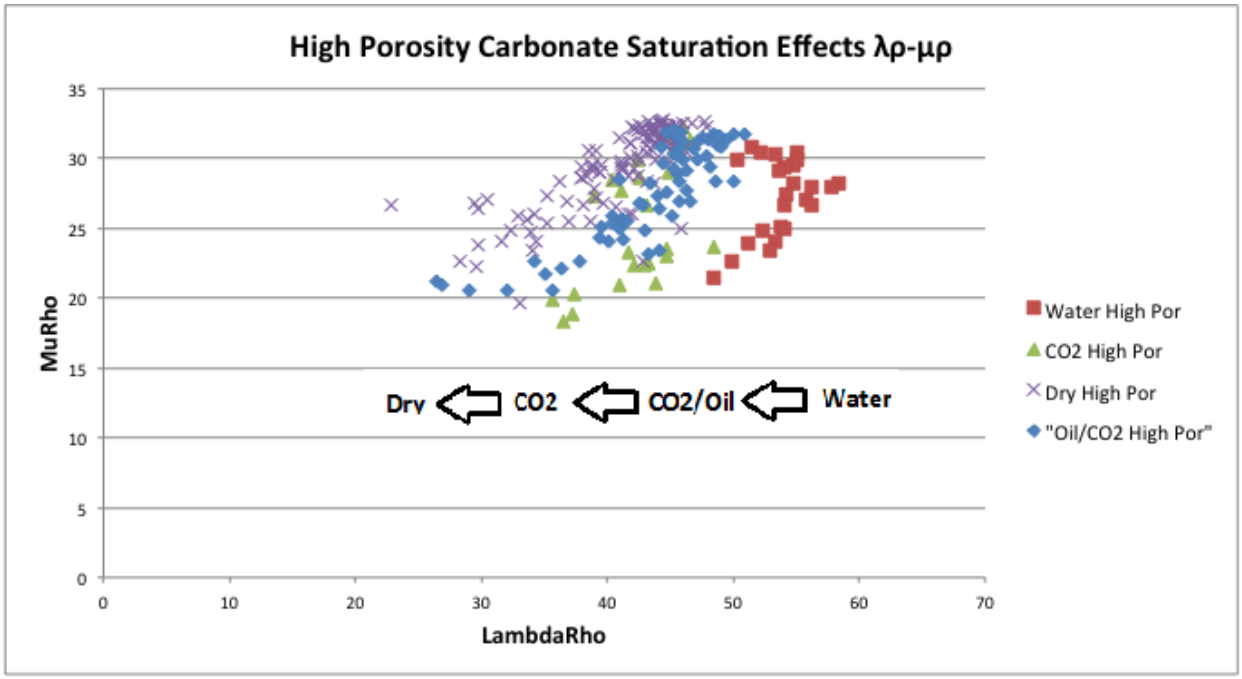

Figure 22: Fluid effects on elastic moduli of high porosity carbonate sample.

Using the dry experiment as a point of reference, and average value of experimental results, we can quantify the effects of pore filling fluids. For the low porosity carbonate sample (Figure 21) the bulk of the data collected for the dry and CO_2 saturated samples fall in similar λρ-μρ space, thus elastic changes due to CO_2 saturation of the low porosity core are minimal (both centered around 80 GPa.gm/cm^3). The water-saturated test for the low porosity sample did shift the value of λρ, increasing the value of λρ by ~33 GPa.gm/cm^3 or about 41%.

We observe similar effects of pore-filling fluids on the high porosity carbonate sample (Figure 22). The high porosity dry experiment yields a λρ of ~43 GPa.gm/cm^3. Saturating the sample with CO_2 increased λρ to ~45, only about a 5% change. The oil/CO_2 saturated sample (5% mineral oil mixed with 95% CO_2) increased λρ to ~46, a 7% change from the dry sample and ~2.22% change from the purely CO_2 saturated sample. Once again the deionized water saturated core experiment yielded the highest value of λρ at ~55 GPa.gm/cm^3. This marks an

increase of ~12 (or ~28%) from the dry experiment, ~10 (or ~22.22%) from the CO_2 saturated sample, and ~9 (or ~20%) increase from the oil/CO_2 experiment. Although the CO_2 and oil mix experiment only contained about 5% mineral oil, we do see a slight increase in $\lambda\rho$. This suggests that a sample fully saturated with mineral oil would increase $\lambda\rho$ by more than that of CO_2.

Our experiments run on both the high and low porosity core samples, indicate that water causes the greatest shifts in $\lambda\rho$, at ~41% for the low porosity sample and 28% for the high porosity sample. CO_2 also seems to increase $\lambda\rho$, however, because this increase is only apparent in the higher porosity sample, the effects of CO_2 saturation may be negligible with small CO_2 volumes.

3.3.4 Comparison to Hoffe, Perez, and Goodway's Model

It is helpful to compare our findings with existing models. Hoffe, Perez, and Goodway have presented a $\lambda\rho$-$\mu\rho$ space model for interpreting data, providing insight into AVO classes and the effects of fluids on these classes (Goodway, Chen et al. 1997, Goodway 2001, Hoffe, Perez et al. 2008, Goodway 2010). Figure 23 below depicts this model with AVO classes superimposed overtop the general rock models. This model predicts shifts in $\lambda\rho$-$\mu\rho$ space due to porosity, pore-filling fluids and lithology.

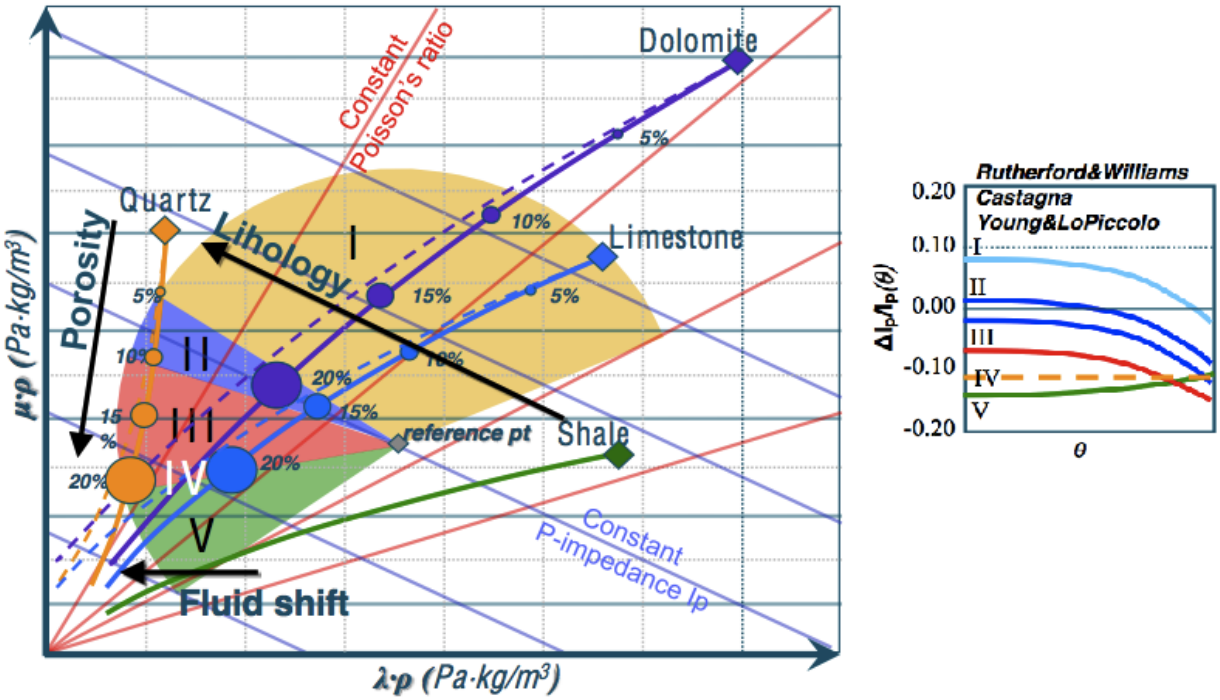

Figure 23: λρ-μρ model with AVO classes. (Hoffe, Perez et al. 2008). Shading over laying the plot represents regions of different AVO class in λρ-μρ space. The smaller figure to right is the original AVO class as described by Rutherford and Williams. AVO class curves defined by relative impedance and angle of incidence θ. (Rutherford and Williams 1989)

Our data for both the rhyolite and carbonate samples, when plotted over Hoffe, Perez and Goodway's Model suggest that our data seems to fit well with the model in terms of rock porosity (Figure 24 and Figure 25). We do not however, observe as smooth a relationship between porosity and location in the λρ-μρ domain as indicated by Hoffe, Perez, and Goodway. Our experiments indicate that the position in λρ-μρ for rhyolite may remain stable until porosity decreases below ~10%. However rhyolite (an igneous rock) is being compared to sedimentary rock trends. It is reasonable to expect differences in the elastic properties of igneous rocks compared to sedimentary rocks. Despite this deviation from Hoffe, Perez, and Goodway's model, we do observe similar general trends, with high porosity near the origin and low porosity farther out.

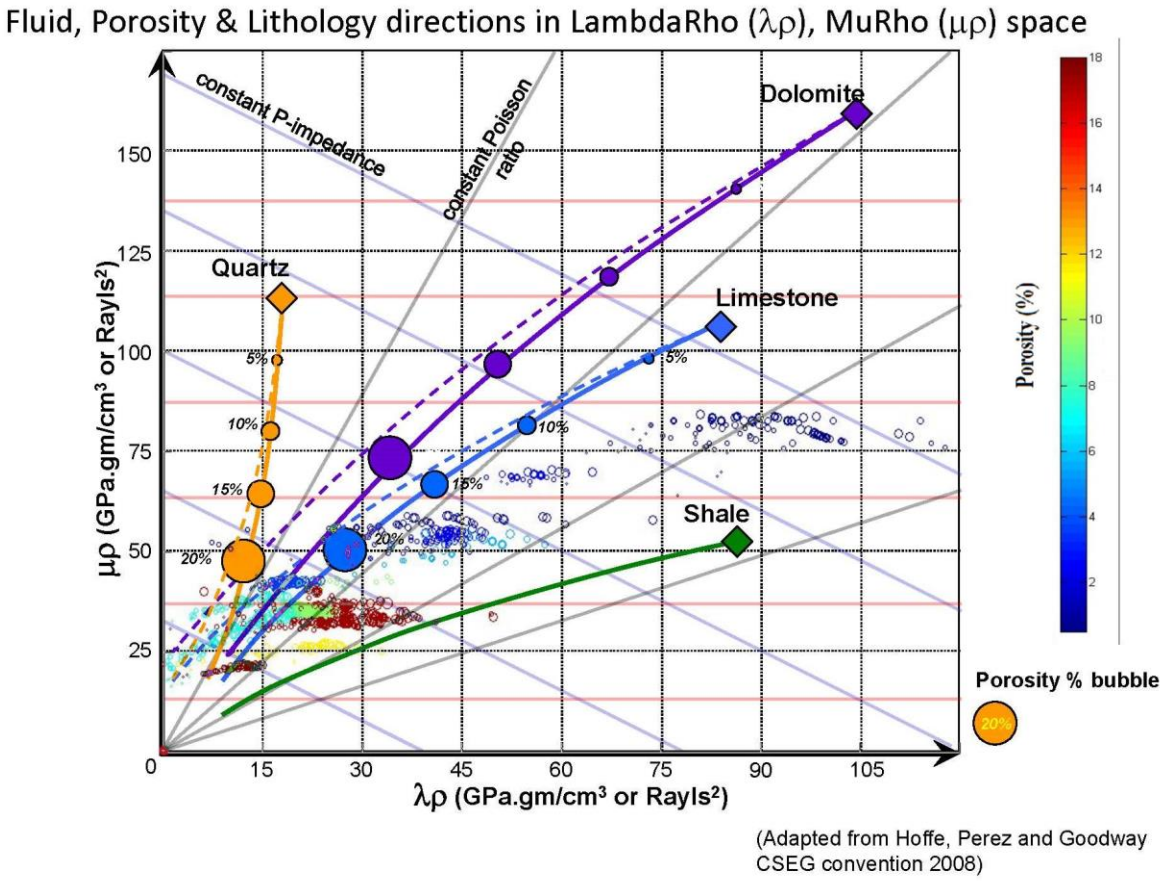

Figure 24: λρ-μρ moduli for all rhyolite core data overlain on Hoffe, Perez, and Goodway's rock moduli model.

In comparing our carbonate core measurements to the model presented by Hoffe, Perez, and Goodway, we again see trends in porosity that follow those presented in the model. Despite the few numbers of carbonate sample cores tested, the porosity zoning of our samples seems to agree with the model. Thus, our observed relationship between porosity and λρ-μρ agrees with the Hoffe, Perez, and Goodway model. Further, our results on relationships between fluid content and λρ and μρ values agree with those of Goodway's experiments which indicated the water causing the greatest increase, followed by gasses such as CO_2 and air (Goodway 2010).

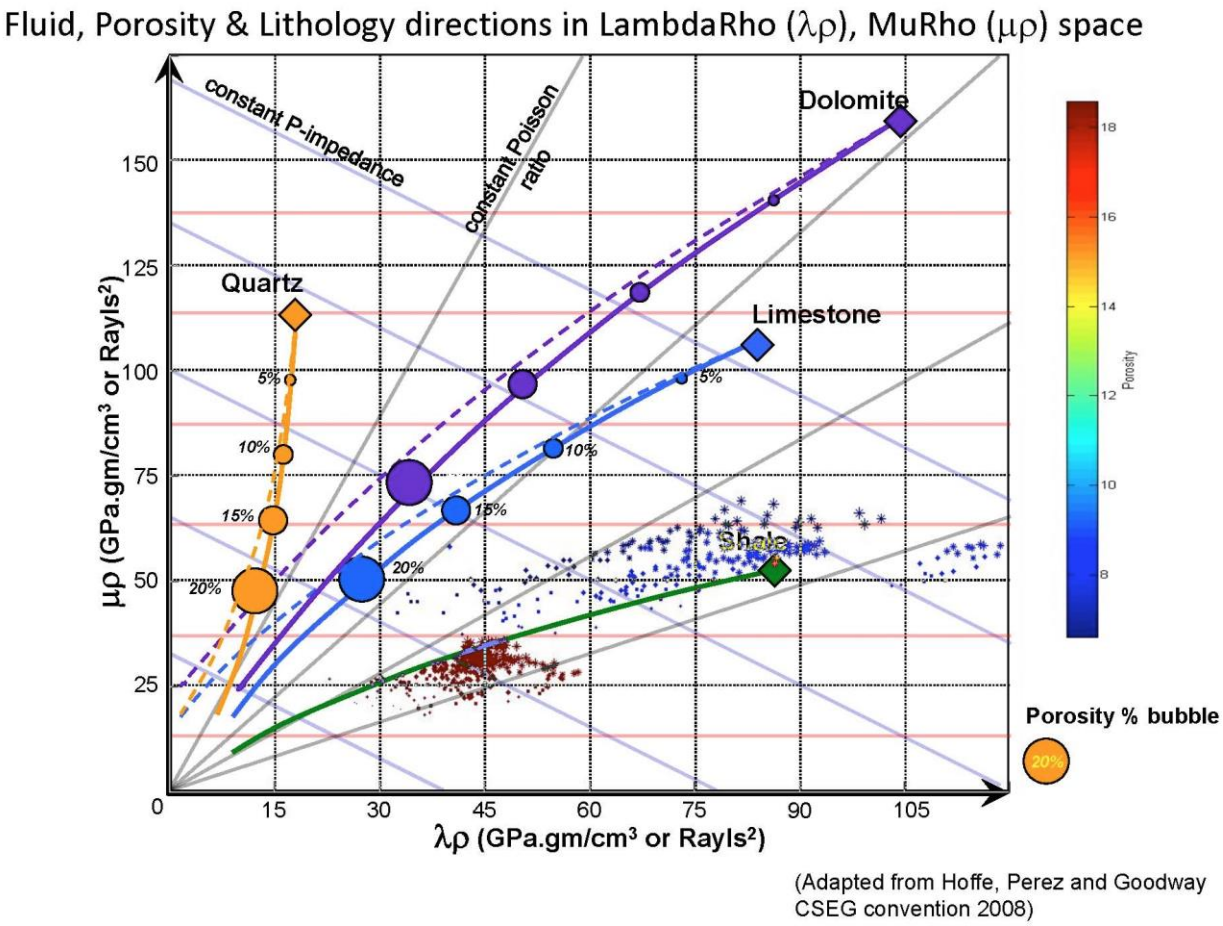

Figure 25: λρ-μρ for all Carbonate cores plotted over Hoffe, Perez and Goodway's model for rock moduli.

Relationships in our experimental data, suggest that while both lithologies have values of λρ comparable with Hoffe, Perez, and Goodway's model, μρ values are lower than predicted by the model. Carbonate samples should fall along or near the limestone curve while rhyolite does not have a comparable lithology. In terms of mineral composition, rhyolite is largely composed of quartz mineral and therefore might fall near the quartz line.

Although we observe lower values of μρ than Hoffe, Perez, and Goodway, we do still observe the same general lithology effects. A shift in lithology, from carbonate (limestone) to rhyoloite (largely composed of quartz) increases μρ and decreases λρ. From our observations we

can conclude that our petrophysical model very strongly agrees with the model presented by Hoffe, Perez, and Goodway (Hoffe, Perez et al. 2008).

3.4 PETROPHYSICAL MEASUREMENTS DISCUSSION AND CONCLUSIONS: PETROPHYSICAL MODEL

Rock is a complex material and understanding its elastic properties is not trivial. Our experiments and analysis characterize the elastic nature of rock as well as the effects of pressure, temperature, porosity and fluid saturation on elasticity. Our measurements strongly support the model presented by Hoffe, Perez, and Goodway. We have observed very similar trends in lithology, porosity and fluid saturation effects. This research has not only confirmed pre-existing models, but also acted to expand our understanding of these models. Apart from their model, we have observed a slight inverse relation between μρ and temperature. In terms of porosity, we conclude that porosity zoning is prevalent for samples in λρ-μρ space as well as for V_p-V_s for rhyolite with higher porosity samples fall nearer to the origin. However our observation seems to indicate that at higher porosities (~10%), this trend may not be accurate as our rhyolite data remains stable until in λρ-μρ space until core porosity decreases below ~10%. This observation was also examined in the V_p-V_s relationship of rhyolite (with $V_{s1} = 0.469 * V_p + 625.64$). Location of a rock in λρ-μρ space is weakly dependent on temperature as well as for effective pressure. The effects of temperature and effective pressure of the core are insignificant compared to changes in core porosity.

In terms of fluid saturation, our observations confirm Hoffe, Perez, and Goodway's model ((Hoffe, Perez et al. 2008)). Examination of fluid saturation in carbonate cores indicates

that the introduction of pore-filling fluids shifts λρ and has no effect on μρ. We observe the shift in λρ to increase with these following sets of fluids, air, CO_2, CO_2/Oil and water. Our measurements expand upon Hoffe, Perez, and Goodway model (2012) by including CO_2 as well as an oil/CO_2 mix into the fluid trend models in order to differentiate CO_2 from other gasses for purpose of carbon capture monitoring.

This research and our observations regarding the effects of physical changes in rock material in λρ-μρ space can clarify AVO analysis. The most influential physical changes affecting λρ-μρ are lithology, porosity, and fluid saturation. Paired with stratigraphic knowledge of a region, our improved understanding of λρ-μρ and porosity, lithology, and fluid saturation can allow us to infer more precisely the physical state of the subsurface through AVO analysis. This knowledge is invaluable for energy exploration CO_2 sequestration and geothermal reservoir infrastructure.

4.0 ULTRASONIC SEISMIC WAVE ATTENUATION, Q

As a seismic wave travels through rock the wave loses energy and shifts in frequencies. In other words, as the wave propagates through rock it attenuates (Figure 26). The attenuation of a simple seismic wavelet is displayed in Figure 26 below. Q represents the quality factor; it is a dimensionless term, which is related to seismic wave attenuation. It is important to note that Q is inversely proportional to the attenuation coefficient of a material, that is, as attenuation decreases; Q increases (Toksöz and Johnston 1981).

Figure 26: Figure depicts a wave pulse before and after traveling through a rock core

There are two main attenuation mechanisms that act on a wave as it propagates through rock. Geometric attenuation is a decrease in amplitude of a seismic signal as the wave spreads out over a larger area (Owino and Jacobs 1999). This geometric spreading of the energy of the wave is similar to a decrease in energy density of the wave. The second mechanism, material attenuation in which the wave attenuates due to energy absorption (intrinsic) due to internal

friction as well as scattering (extrinsic) in which portions of the wave energy are scattered off pores, fractures and other boundaries within the rock (Owino and Jacobs 1999).

The attenuation of seismic waves has been shown to be directly dependent on the physical properties of the rock including porosity, grain size, as well as the saturation levels within the rock (Velea, Shields et al. , Winkler 1983, Generazio, Roth et al. 1988, Prasad and Meissner 1992, Winkler and Murphy III 1995). This dependence of attenuation and hence Q, is advantageous in terms of analyzing seismic waves. We can understand seismic wave attenuation as a convolution signature left on the waveform due to its passage through the rock. With this in mind we can understand Q to be can be used to characterize the microstructural properties of the rock through which the wave traveled (Owino and Jacobs 1999).

4.1.1 The Spectral Ratio Method: Determining Q

To calculate the quality factor Q from ultrasonic measurements we employed the spectral ratio method. This method compares the input wave spectrum to the output wave spectrum. By examining the ratio of the input to output wave spectrum we can gain insight as to how the wave attenuated and calculate the quality factor of the rock using Equation 29. This method assumes Q is frequency independent. Because the Autolab 1500 device is only capable of recording the waveform after it has passed through the core, a reference core (an aluminum core in our case) causing little to no wave attenuation is used. For our reference core we tested an aluminum core. Because the Q of an aluminum is high (about 150,000 (Zemanek Jr and Rudnick 1961)), the wave is transmitted with virtually no attenuation, allowing approximation of the waveform entering the rock by measuring the downstream wave form. Note: The aluminum core was tested at various different effective pressures and exhibited little to no change in waveform or

spectrum. All data was processed and calculations made using MATLAB. We computed the amplitude frequency spectra of both the rock core samples as well as the aluminum reference core sample using fast Fourier transforms (fft). Data was processed for all effective pressures, temperatures, and rock core types.

4.1.2 Derivation of Relevant Formulas

The amplitudes of plane seismic waves in the reference and sample core, generated by the Autolab 1500, can be expressed by the following expressions,

$$A_{ref} = G_{ref}(x)e^{-\alpha_{ref}(f)x}e^{i(2\pi ft - k_{ref}x)} \quad \textbf{Equation 16}$$

$$A_{rock} = G_{rock}(x)e^{-\alpha_{rock}(f)x}e^{i(2\pi ft - k_{rock}x)} \quad \textbf{Equation 17}$$

(Toksoz et al. 1979)

Where A is the amplitude, G(x) represents the geometrical factor which accounts for wave spreading and reflection, f is the frequency, x is distance (core length), and $k = \frac{2\pi f}{v} = wavenumber$ where v is the velocity and $\alpha(x)$ is the frequency dependent attenuation coefficient.

For measurements between .1 and 1 MHz it is safe to assume that α is a linear function of frequency. From this we have $\alpha(f) = \gamma f$ where $Q = \frac{\pi}{\gamma v}$ and Q is the seismic attenuation

factor. We have the same geometry for the sample core and the reference cores so we can assume that G_{ref} and G_{rock} are frequency independent. (Johnston, Toksöz et al. 1979)

By taking the ratio of Equation 16 and Equation 17 we get

$$\frac{A_{ref}}{A_{rock}} = \frac{G_{ref}(x)e^{-\alpha_{ref}(f)x}e^{i(2\pi ft - k_{ref}x)}}{G_{rock}(x)e^{-\alpha_{rock}(f)x}e^{i(2\pi ft - k_{rock}x)}} \quad \textbf{Equation 18}$$

$$\frac{A_{ref}}{A_{rock}} = \frac{G_{ref}(x)e^{-\alpha_{ref}(f)x}e^{i(2\pi ft - k_{ref}x)}}{G_{rock}(x)e^{-\alpha_{rock}(f)x}e^{i(2\pi ft - k_{rock}x)}} \quad \textbf{Equation 19}$$

$$\frac{A_{ref}}{A_{rock}} = \frac{G_{ref}}{G_{rock}}e^{x[\alpha_{rock}(f) - \alpha_{ref}(f)]}e^{ix[k_{rock} - k_{ref}]} \quad \textbf{Equation 20}$$

$$\frac{A_{ref}}{A_{rock}} = \frac{G_{ref}}{G_{rock}}e^{x[\alpha_{rock}(f) - \alpha_{ref}(f)]}e^{ix[k_{rock} - k_{ref}]} \quad \textbf{Equation 21}$$

$$\frac{A_{ref}}{A_{rock}} = \frac{G_{ref}}{G_{rock}}e^{x[\alpha_{rock}(f) - \alpha_{ref}(f)] + ix[k_{rock} - k_{ref}]} \quad \textbf{Equation 22}$$

And finally we have

$$[\frac{A_{ref}}{A_{rock}}] = \frac{G_{ref}}{G_{rock}}e^{x[\alpha_{rock}(f) - \alpha_{ref}(f)]} \quad \textbf{Equation 23}$$

We can assume $\alpha(f)$ to be frequency independent over the range of .1-1.0MHz, so we assume $\alpha(f) = \gamma f$ where $\gamma = \frac{\pi}{Qv}$ (Johnston, Toksöz et al. 1979).

Substituting this into Equation 23 we achieve

$$\frac{A_{ref}}{A_{rock}} = \frac{G_{ref}}{G_{rock}} e^{xf[\gamma_{rock} - \gamma_{ref}]} \quad \textbf{Equation 24}$$

Because $\gamma = \frac{\pi}{Qv}$, and Q for aluminum is high (about 150,000 (Zemanek Jr and Rudnick 1961)), We can safely assume $\gamma_{ref} = 0$

$$\frac{A_{ref}}{A_{rock}} = \frac{G_{ref}}{G_{rock}} e^{xf[\gamma_{rock}]} \quad \textbf{Equation 25}$$

Taking the Natural Log

$$\ln\left(\frac{A_{ref}}{A_{rock}}\right) = \ln\left(\frac{G_{ref}}{G_{rock}} e^{xf[\gamma_{rock}]}\right) \quad \textbf{Equation 26}$$

$$= f\gamma_{rock}x + \ln\left(\frac{G_{ref}}{G_{rock}}\right)$$

$\ln\left(\frac{G_{ref}}{G_{rock}}\right)$ is a constant as G is assumed frequency independent. This is now in the linear form $y = mx + b$.

By taking the first derivative

$$\frac{\partial}{\partial f}\left[\ln\left(\frac{A_{ref}}{A_{rock}}\right)\right] = x\gamma_{rock} \quad \textbf{Equation 27}$$

Substituting $\gamma = \frac{\pi}{Qv}$ into Equation 27 we achieve

$$\frac{\partial}{\partial f}[\ln\left(\frac{A_{ref}}{A_{rock}}\right)] = x\frac{\pi}{Q_{rock}v} \quad \textbf{Equation 28}$$

Finally, by rearranging Equation 28

$$Q_{rock}^{-1} = \frac{v}{x\pi}\frac{\partial}{\partial f}[\ln\left(\frac{A_{ref}}{A_{rock}}\right)] \quad \textbf{Equation 29}$$

With this we are able to calculate attenuation Q from the slope of a straight line fit to the natural log of the ratio of aluminum wave amplitude spectra to rock wave amplitude spectra.

4.1.3 Errors and Waveform Clipping

Waves will reflect inside the rock core samples. As the seismic waves propagate through the rock cores, they not only reflect off of the sides of the core and ends, but the waves can change direction (increasing the path length) and convert between P and S waves inside the sample core. The resulting mixture of reflections and transmitted waves strongly affect our measurements. To minimize error due to wave reflections, only the initial waveform peak was used, precluding the chance for any reflection (Figure 28). By clipping the waveform to the initial peak we are taking the wave before any reflection was ever able to occur, thus making any error due to reflection nonexistent or negligible. In order to consistently pick these initial arrivals, a power criterion was written into the MATLAB script which detecting the beginning of the waveform by using a threshold where the amplitude exceeds noise and ends the waveform a

designated amount of steps after the picked beginning of the waveform. Because clipping a waveform adds high frequencies, this would introduce error into our measurements. In order to reduce this error padding was added to the beginning and end to the clipped waveform and the waveform was tapered out using a simple hamming window, which uses a Gaussian window to taper out the edges of the wave. Sample code is provided below

```
        alumPick = find(alumAmplP > .025, 1, 'first') - 357;
        alumPickEnd = alumPick + 1071;
        alumTimePick = (alumPick*alumdt:alumdt:alumPickEnd*alumdt);
        ClippedAlumWave = alumAmplP(alumPick:alumPickEnd);
        ClippedAlumT = (alumTimePick);
        TaperClippedAlumWave                                                    =
window(@hamming,numel(ClippedAlumT)).*transpose(ClippedAlumWave)';
```

Figure 27: Sample code for windowing and tapering waveforms.

The provided code above picks the initial peak of the aluminum core and pads it with a time stamp of about 150% of the period of the initial wave peak. This same time padding was also added to the end of the waveform (Figure 28).

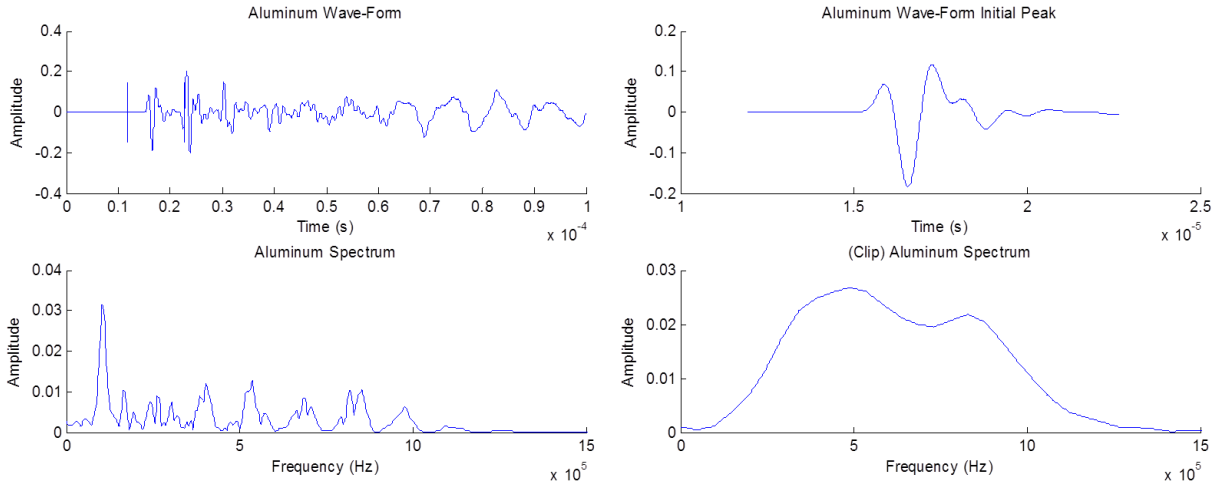

Figure 28: Top left is aluminum core P-wave form and directly below is the spectrum. Top right is the clipped segment of the aluminum waveform (the initial peak) and below is the spectrum of the clipped waveform.

This same clipping and tapering process was performed for each rock core waveform (Figure 29 and Figure 30). As effective pressure increases, the spectrum of the clipped rock core waveform increases and begins to approach the aluminum core spectrum.

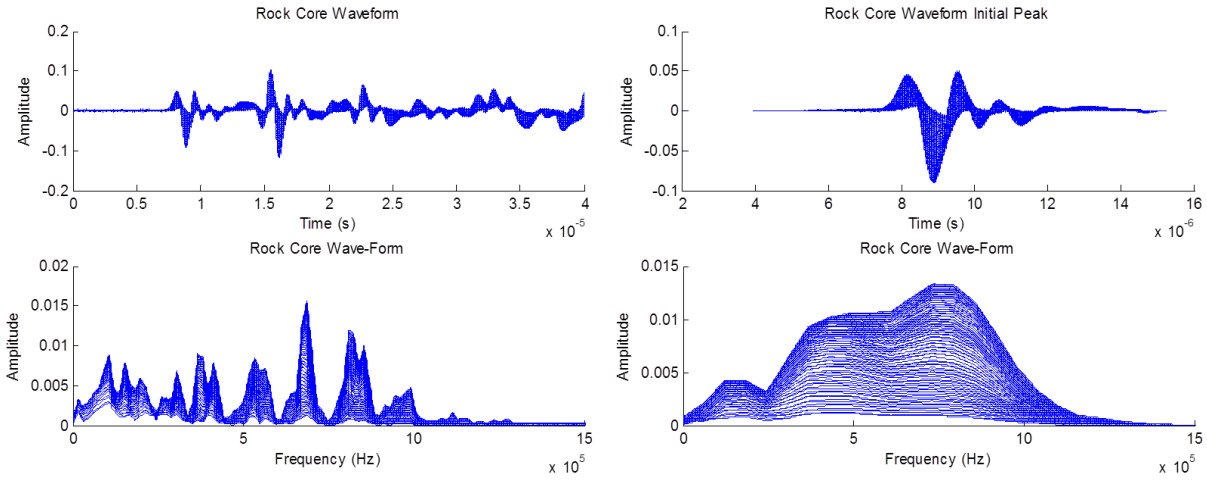

Figure 29: The plots to the left contain the original rock core waveforms and below is there corresponding frequency spectrum. To the right, the clipped and tapered rock core waveforms and its frequency spectra below it. Note: The plots are of all rock core waveforms at each effective pressure superimposed over one another.
Rhyolite Sample: 1294779408

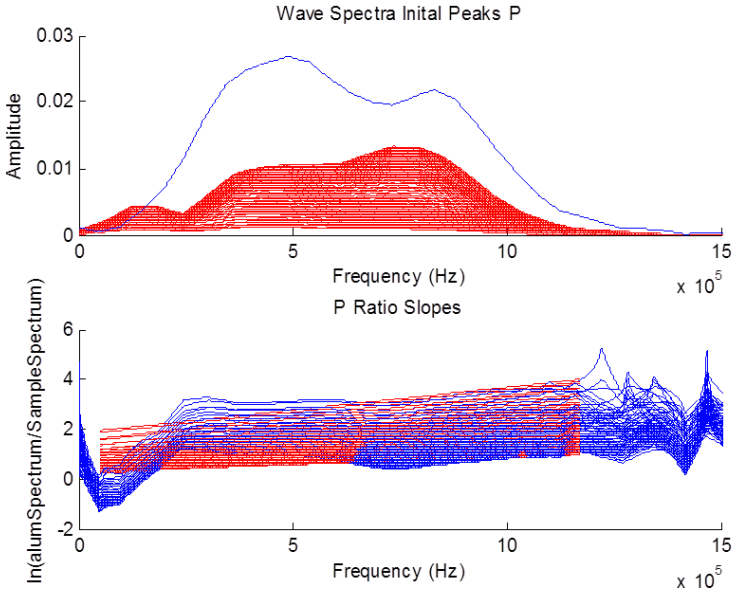

Figure 30: Top Plot- The blue curve is the wave spectrum of the clipped and tapered aluminum wave. The red curves are the rock core waveforms with increasing effective pressure superimposed over top each other.
Bottom Plot- The blue curves are the natural log for of the ratio of the wave spectra for each effective

pressure. The red is the linear best-fit line from the slope of which Q was calculated from. Rhyolite Sample: 1294779408

4.1.4 Fourth Generation CT Scanner

Using a Universal systems HD-350E Computer Tomography (CT) scanner (Figure 31) at the National Energy Technology Laboratory, a CT scan for the low porosity carbonate sample was taken. The carbonate core was entered into the device, which a 140 kV source. Using the gathered X-ray attenuation data from each of these detectors, a 2D image slice of the core can be created. By taking multiple image slices of the core, we are able to create a 3D virtual image of the carbonate core. Using the Fiji ImageJ software the image slices were stacked and the virtual core was generated and examined. This method of imaging the core sample is non-invasive and does not affect or alter the core. We have utilized the fourth generation CT scanner to investigate into the internal structure of our low porosity carbonate core to better understand our observations regarding Q.

Figure 31: Medical CT scanner. Image source: <http://www.universal-systems.com/HD_350.php#house1>

4.2 DATA

4.2.1 Carbonate: Effects of Pore-Filling Fluids

Two separate carbonate cores were tested, at and were tested at 50 °C, dry and with various pore-filling fluids. The two cores were geometrically similar however one had a porosity of 18.5% and the other a porosity of 8%. Table 5 summarizes the experimental design.

Porosity (%)	Experiment	Temperature (°C)	-Pore-Filling Fluids
18.5	1321544044	50	Dry (Air)

	1322579001 1326468617 1328199323		CO_2 DeionizedWater Oil/CO_2
8	1320693557 1325778014 1326822698	50	Dry (Air) CO_2 DeionizedWater

Table 5: Experiments performed on core samples.

Prior to our examination of wave attenuation, we examine the effects of pore filling fluid on ultrasonic seismic velocities (Figure 26 and Figure 28).

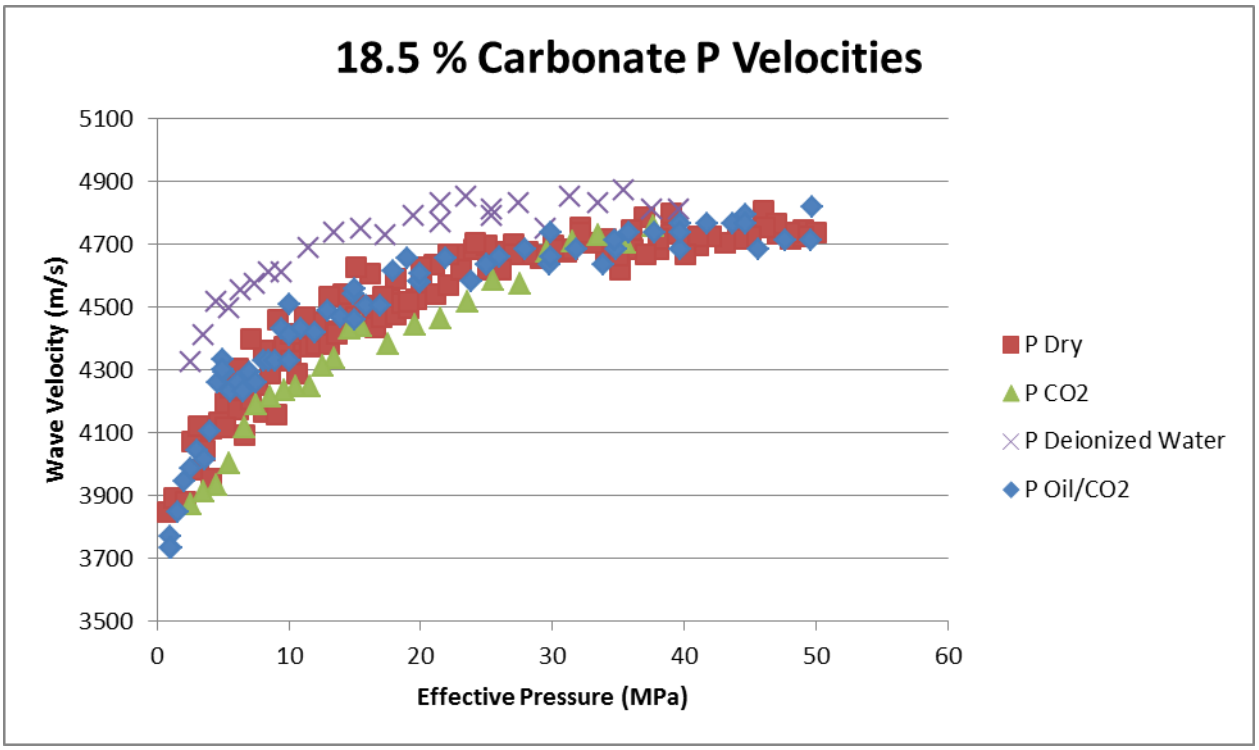

Figure 32: P-wave ultrasonic velocities measured on high porosity carbonate sample. The oil/CO_2 mix experiment was run with ~5% oil and 95% CO_2.

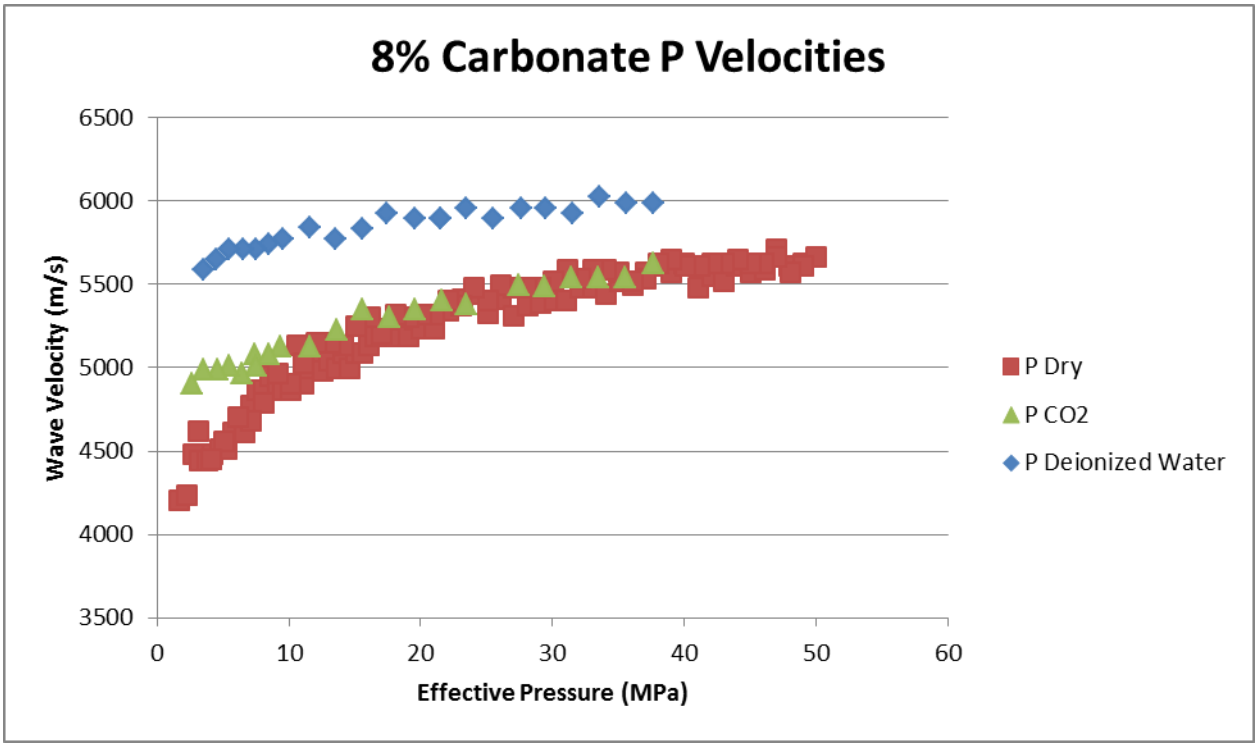

Figure 33: Ultrasonic P-wave velocity measurements for low porosity carbonate sample.

Seismic velocity through the low porosity sample is significantly higher than that of the high porosity carbonate core. With less pore space, waves encounter less of the lower velocity material (air, CO_2, water) and therefore slowing the observed wave velocity. Our measurements from both the high and low porosity cores indicate that varying the pore-filling fluid of the cores does affect the wave velocity. Water filled pores results in the fastest wave velocity in both cases. The effects of CO_2 (as well as our 5% oil 95%CO_2) seem to be insignificant in the low porosity sample, but do slightly decrease in wave velocity in the higher porosity core. It is interesting to note that the introduction of water into the lower porosity core caused the greatest change in velocity (~500 m/s increase). This effect could be due to only partial saturation of the higher porosity core sample. For our analysis we have assumed total core saturation, however the assumption is challenging to test.

The quality factor of the rock (Equation 29), is inversely proportional to the wave velocity, this is observed in our Q measurements. Figure 34 and Figure 35 below display our results in measuring the quality factor of the rock cores with each different pore-filling fluid as well as both the high and low porosity samples respectively.

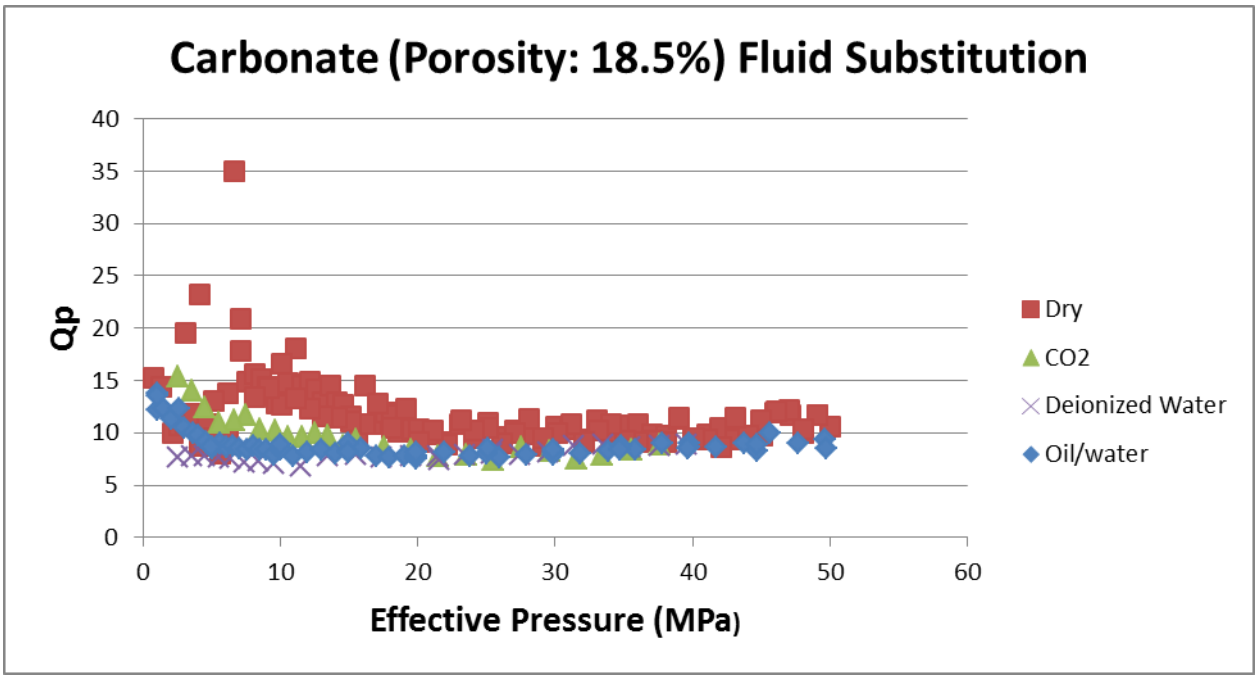

Figure 34: Q vs. Effective Pressure for the high porosity carbonate sample. The sample was tested dry as well as with CO_2, deionized water, and a mix of deionized water with ~5% oil.

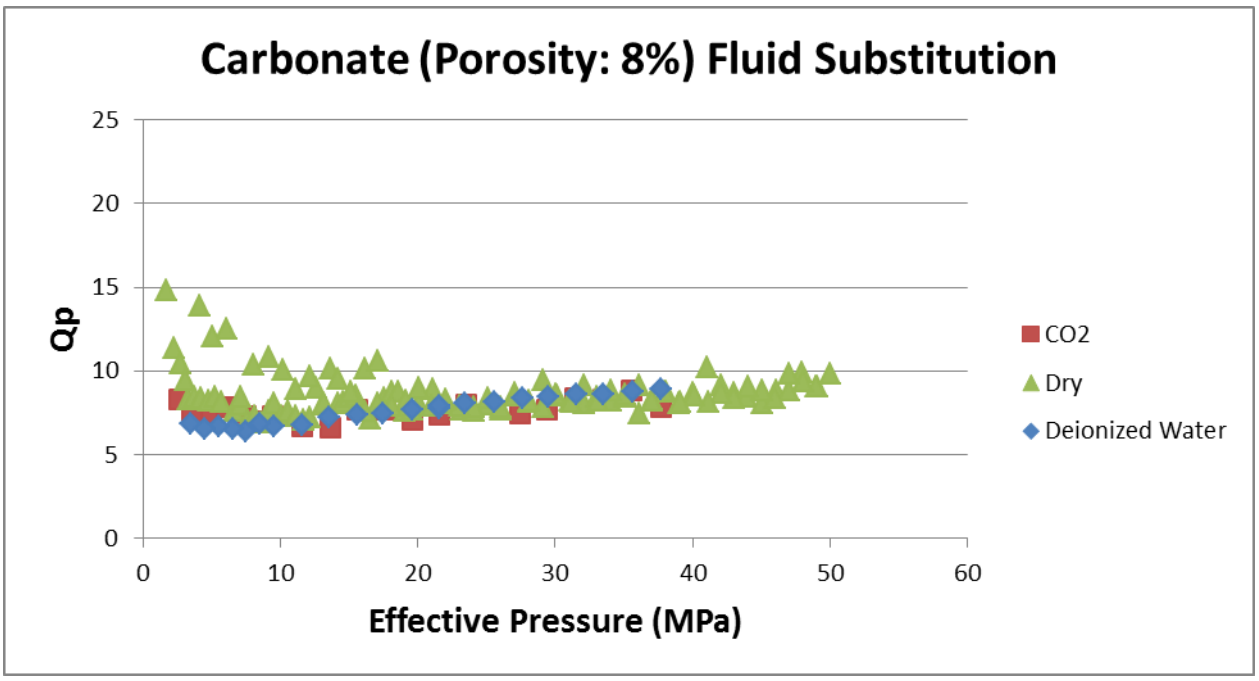

Figure 35: Q vs. Effective Pressure for the low porosity carbonate sample. The sample was tested dry, saturated with CO_2, and with deionized water.

In both the high and low porosity carbonate rock cores we see abnormally low values for Q, which seem to level out around 10 (typical values of Q range from ~20-100). These low values for Q in our sample indicate large amounts of energy loss possible due to large scattering. This scattering could be the result of some sort of large void or pocket or other heterogeneity inside the sample core.

Utilizing the CT scans from the fourth generation medical scanner, we were able to investigate the internal structure of the low porosity carbonate sample and the source of scattering in the carbonate samples (Figure 34). A large heterogeneity cross cutting our sample core and is likely the result of precipitated material within the core. Unfortunately a CT image for the higher porosity core sample was not collected, however due to the similar attenuation observations we may expect a similar heterogeneity in the higher porosity sample. It is unfortunate that this large scattering confounds the effect of pore-filling fluids onto Q, this

analysis clarifies the dominant effect of heterogeneities on the quality factor. With the inclusion of heterogeneities, the effects of varying pore-filling fluids on Q are insignificant.

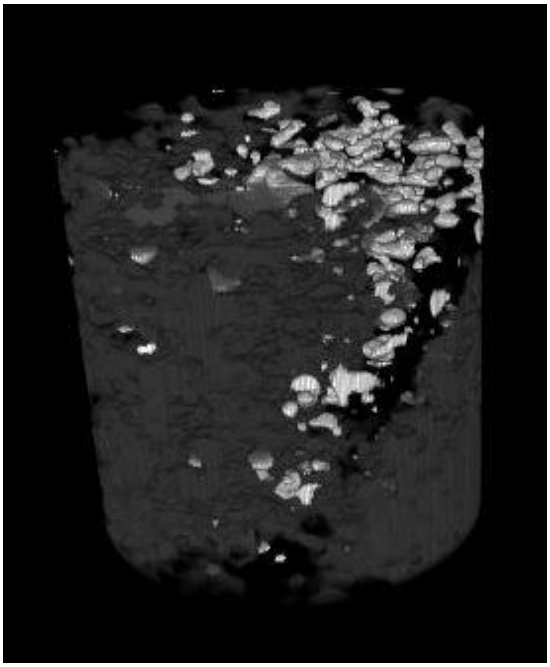

Figure 36: CT scan of low porosity carbonate sample. Darker regions are regions of lower porosity and the lighter regions represent regions of higher porosity.

Despite the effects of pore-filling fluid on wave velocity, Q is relatively insensitive to pore-filling fluids. There are small variations in the quality factor with the addition of different pore-filling fluids at lower effective pressures. Water yields the lowest value of Q, followed by CO_2 and with the dry (air saturated) sample having the highest values of Q. This effect seems to diminish at higher pressures. We also observe a larger variance in the value of Q for the dry sample than for fluid saturated experiments. This phenomenon is likely the result of stabilization of the compliant pore framework and less compressible fluids such as water propping open otherwise compliant pores.

Hysteresis effects of pressurization on Q can be observed for the dry experiments (Figure 37). We may note that at higher effective pressures we do not observe any variance between the pressurizing and depressurizing measurements. At lower effective pressures Q measurements

display some difference between pressurizing and depressurizing measurements. Depressurization of the core results in higher observed values of Q at lower effective pressures, however these effects are minimal. The inclusion of pore-filling fluids negates in the rock seems to negate hysteresis effects in the core by stabilizing the compliant internal core structure.

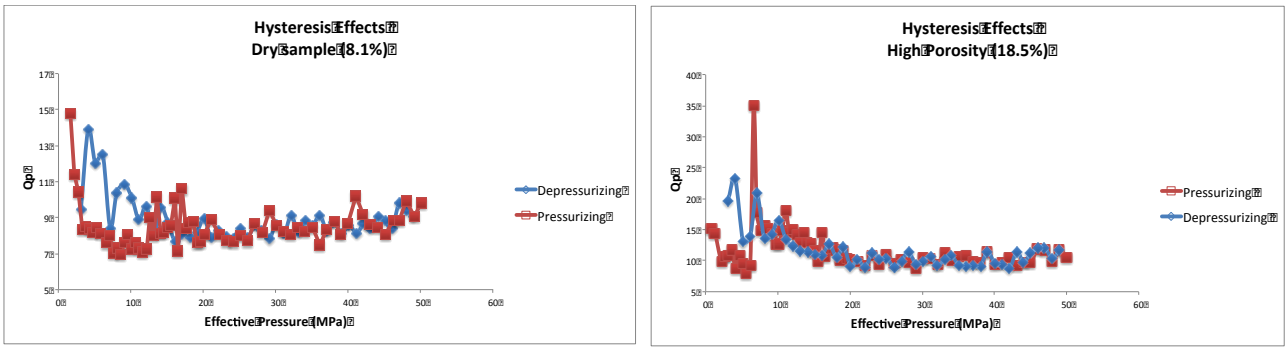

Figure 37: Hysteresis effects of pressurizing and depressurizing of dry carbonate cores. The red line is the pressurization curve and the blue line is the depressurization measurements.

Our observations indicate fluid effects as well hysteresis effects diminish with increasing effective pressure. We also observe that the inclusion of fluids seems to negate hysteresis effects of pressurization, by stabilizing the compliant structure of the core and propping open compliant cores. We must remember that even though some variation in Q with pore filling fluid is observed, the effects are very small and due to the large amount of uncertainty introduced by scattering effects, no firm conclusions can be drawn from them.

4.2.2 Carbonate Anisotropy

The internal pore and matrix structure of rock is complex. Varying the orientation of the internal structure of the rock material changes the propagation and interaction of seismic waves throughout the material; in other words, the propagation of a seismic wave is dependent on the orientation of the rock. This phenomenon is known as seismic anisotropy. Purcell (2012)

described the relationship between ultrasonic velocities and the orientation of sample core, showing that seismic velocities have a preferred (higher velocity) direction of propagation through the rock core samples. This velocity anisotropy suggest similar anisotropic phenomena for seismic wave attenuation. In order to better constrain and understand the effects of core matrix orientation on ultrasonic seismic attenuation, two carbonate cores were tested, one of high porosity (18.6%) and one of far lower porosity (8%) (Figure 38).

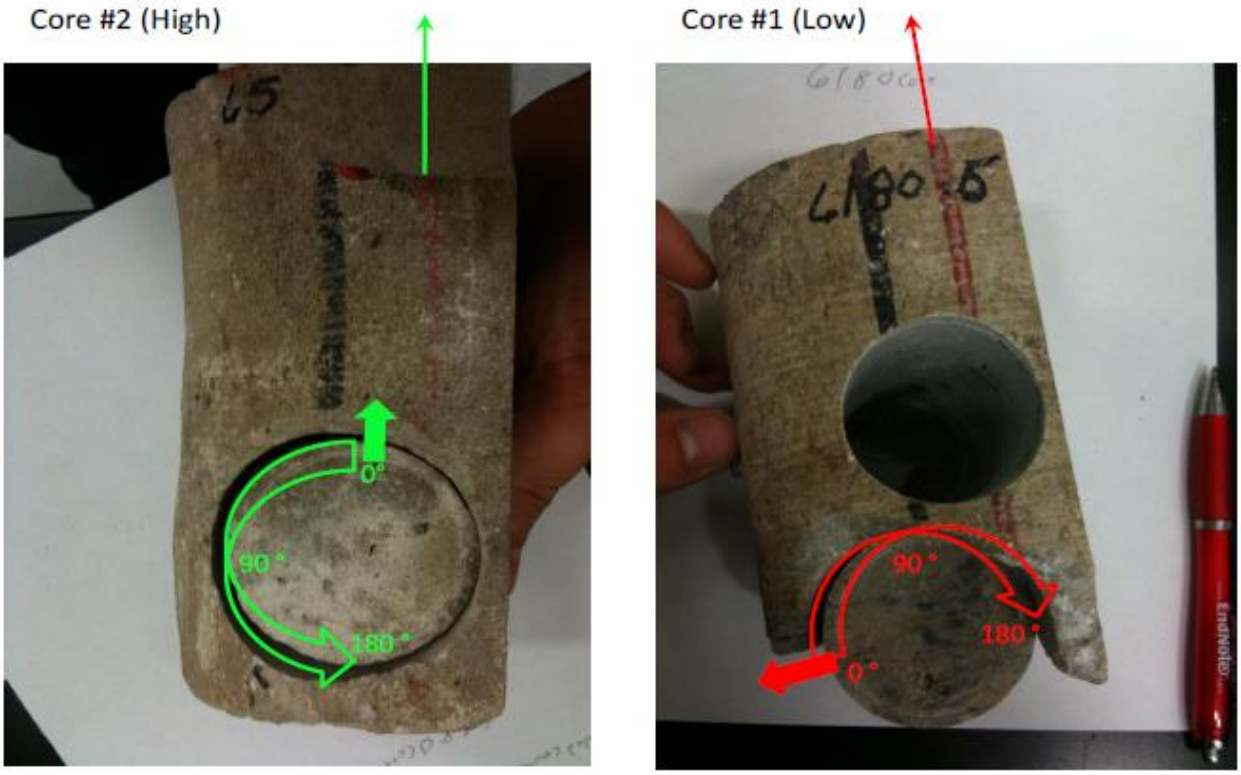

Figure 38: Depicts both the high (left) and low (right) porosity carbonate cores which anisotropy measurements were taken. Arrows indicate the zero degree or orientation and the direction of core rotation. Thinner arrows indicate the top of the rock sample which cores were cut from. (Purcell 2012)

Both cores were tested at four different orientations, rotating the cores 45°, and performing the same ultrasonic measurements. This ensures that waveforms and attenuation can be observed for multiple different pore and matrix orientation. Table 6 summarizes anisotropy experiments performed on carbonate cores.

Core #	Experiment	Porosity (%)	Angle (°)	Pore-Filling Fluid
1	1269616938 1269626264 1269630911 1269634529	8	0 45 90 135	Dry (Air)
2	12713461668 1271354462 1271359503 1271686967	18.6	0 45 90 135	Dry (Air)

Table 6: Contains anisotropy experiment information

The low porosity core sample has a lower value of Q at an angle of 0°(Figure 39), suggesting that this orientation of the internal pore and matrix structure of the core sample most effectively scatters the seismic wave and absorbs more seismic energy than other orientations. It is noteworthy that at higher effective pressures (~50 MPa) we see the anisotropic effects of roting the core to diminish. This may result from compliant pores closing and the transformation of irregular shaped pores assume a more stable spherical shape, appearing isotropic to propagating waves.

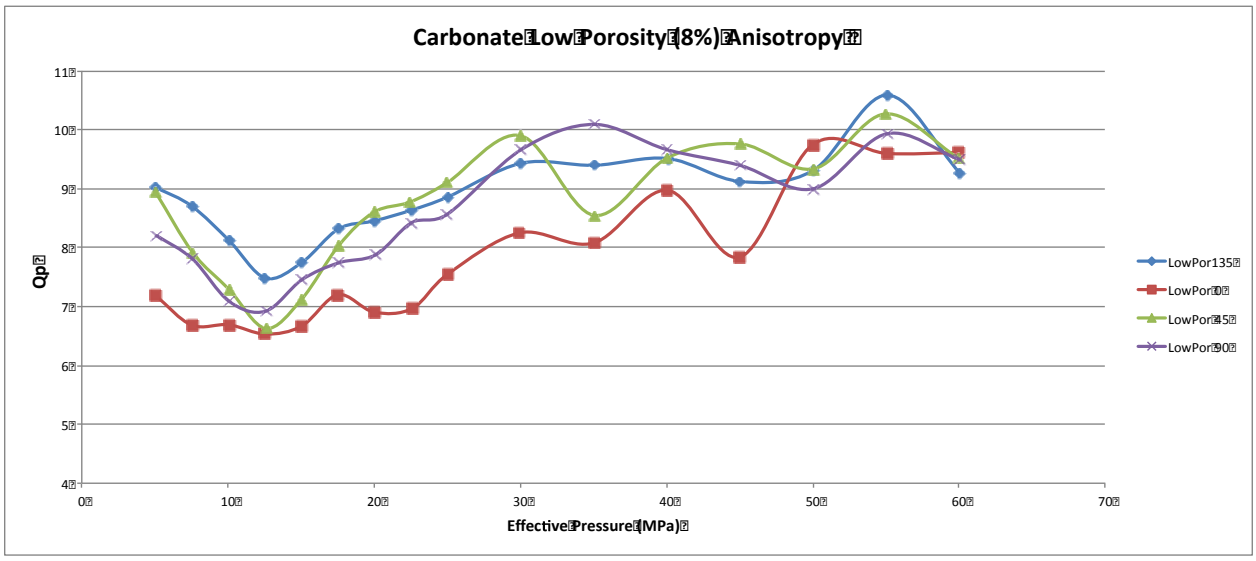

Figure 39: Depicts P-wave quality factor vs. effective pressure at multiple different core orientations for low porosity carbonate sample.

The higher porosity carbonate sample seems to display far less anisotropy effects onto the wave attenuation (Figure 40). The quality factor Q of the high porosity core seems to decrease with increasing effective pressure, suggesting that the effects of closing compliant pores is less important in higher porosity carbonates. The 90° orientation our measurement at 30 MPa we see an outlier with significantly higher value of Q. Because this observation is only made at one effective pressure we conclude that this outlier the result of experimental error. A similar but smaller effect can also be seen at 0° and 20 MPa.

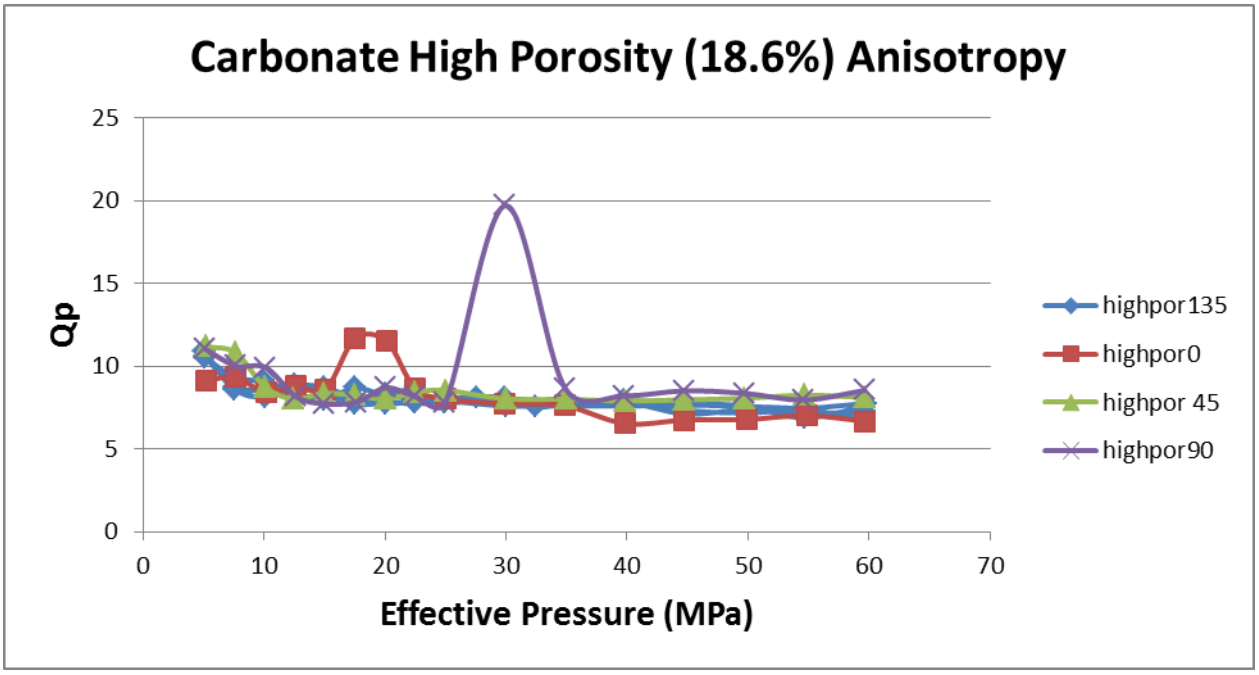

Figure 40: Depicts carbonate P-wave quality factor vs. effective pressure at multiple different core orientations for high porosity carbonate sample.

It is helpful to take a second look at the relationship between core orientation and wave attenuation by comparing Qp at various effective pressures with the angle of orientation (Figure 41 and Figure 42). This allows examination the effects of core anisotropy as a function of both porosity (as per the high and low porosity core) and effective pressure. This clarifies the relationships between Qp and angle of orientation.

Figure 41 below depicts Qp vs. angle for various different effective pressures for the low porosity carbonate sample. Qp increase with effective pressure as well as sinusoidal variations in Qp with respect to core orientation. This implies that there are orientations of more efficient wave propagation through the carbonate core. We see higher values of Qp for orientations at 45° and 135°. At these orientations waves travel most efficiently though the core i.e. the lowest attenuation occurs at these orientations. With this we also note that we see the lowest values of values of Qp at 0° and 90° core orientation. At these orientations we observe the largest amount

of attenuation, therefore the most scattering and absorption occurs at these orientations. We observe a maximum change in Q of ~20% from 0 degree orientation to a 45 degree core orientation. This increase in Q is significant and leads us to believe that Q is dependent on the orientation of the rock matrix.

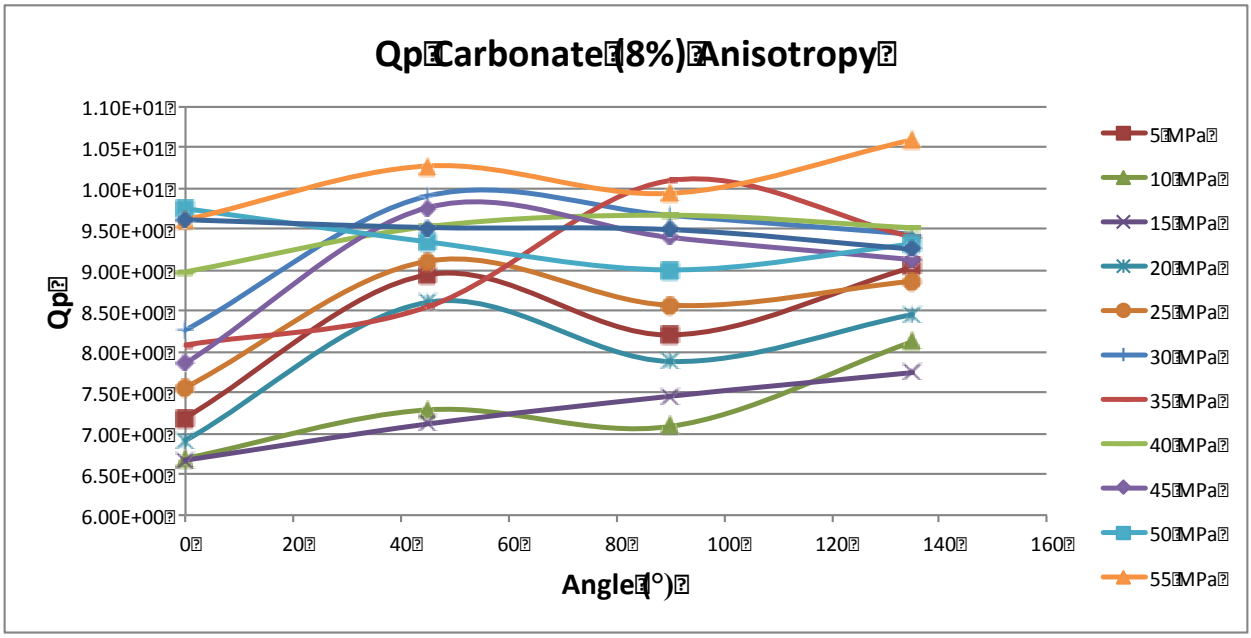

Figure 41: Qp for low porosity carbonate sample vs. angle at various different effective pressures.

When examining high porosity carbonate attenuation results (Figure 42), we see a different relationship than observed for low porosity sample. Qp for the high porosity carbonate sample does not display a strong relationship to effective pressure. Quality factor measurements for the high porosity carbonate sample reveals the most efficient angle of wave propagation at 90° and the least efficient orientation at 0° core orientation, however these relationships are very weak. This indicates that Qp for the high porosity sample is not strongly dependent on orientation of the core. From these measurements we observe that as effective pressure increases, our measurements collapse. Observed Q (disregarding outliers from our 30 MPa measurements), is highest at 5 MPa, followed by 10 MPa, and measurements above 10 MPa seem to collapse to the same points.

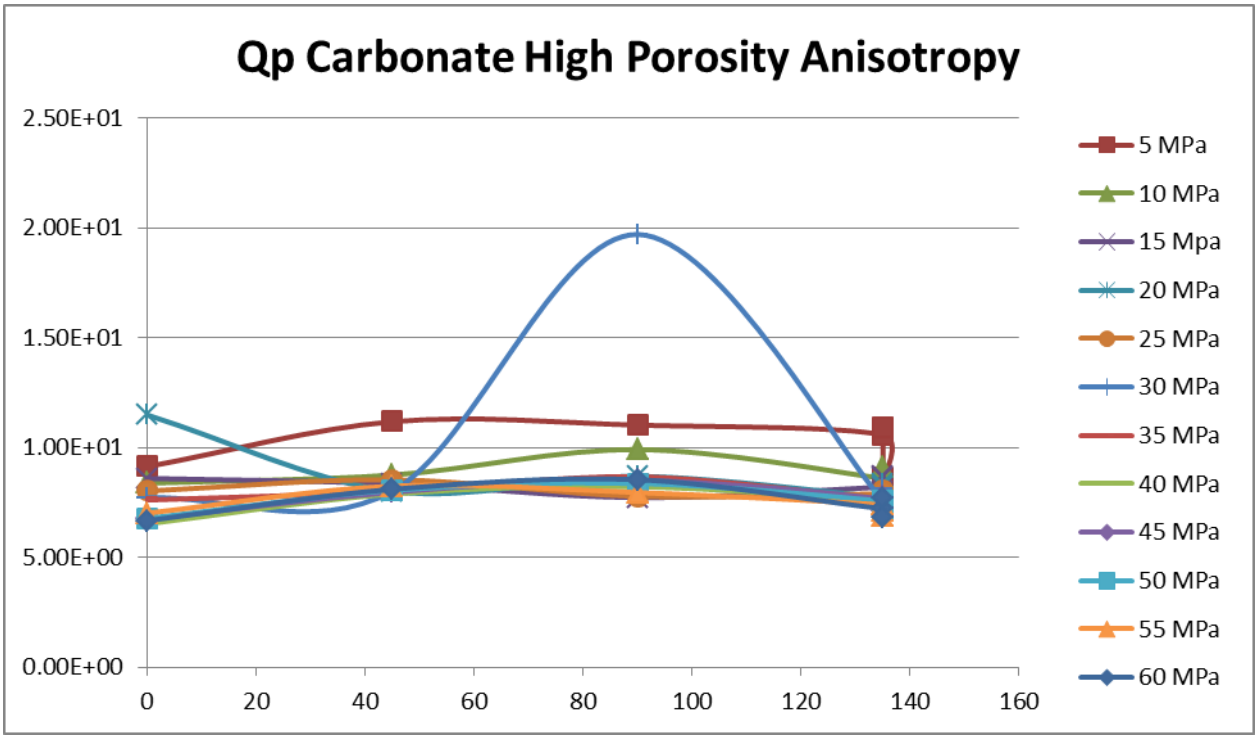

Figure 42: Qp for high porosity carbonate sample vs. angle at various different effective pressures.

The closing of pores and altering the internal pore structure (ie. Pore shapes and closing compliant pores) due to increasing pressure seem to mitigate the effects of core orientation on Q. Plotting ΔQp between angles of orientation 45° and 90° as a function of effective pressure (Figure 43 and Figure 44.) 45° and 90° as these orientations seem to provide consistent representation of preferred and not preferred directions of wave propagation (i.e. a low and high value of Q.)

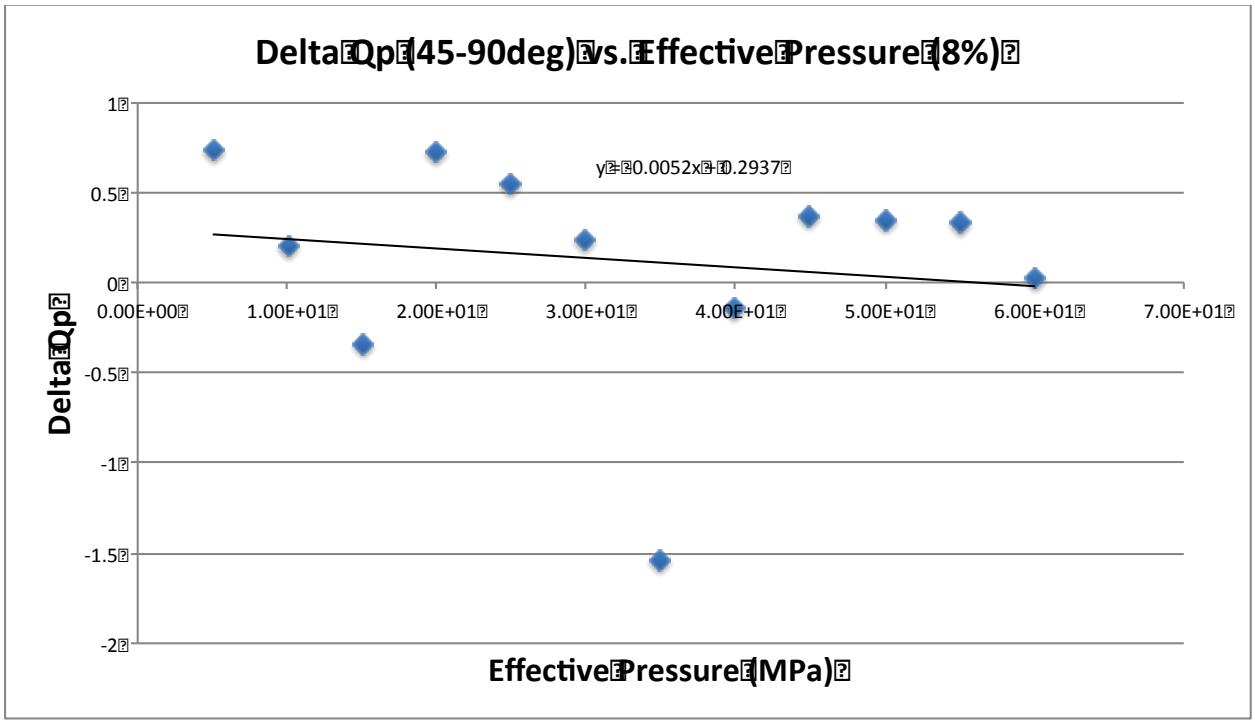

Figure 43: ΔQp vs. effective pressure for the low porosity carbonate sample. ΔQp is calculated using Qp values at 45° and 90° core orientation. R^2=0.02349 for this linear fit.

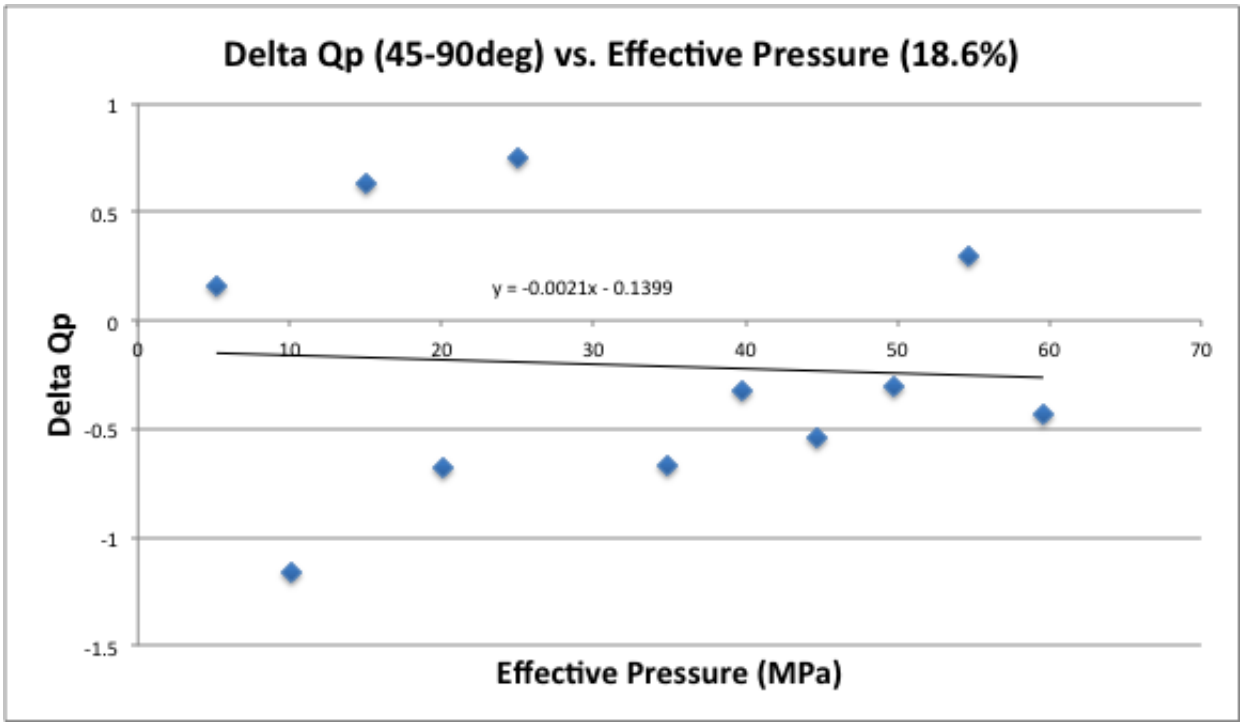

Figure 44: ΔQp vs. effective pressure for the high porosity carbonate sample. ΔQp is calculated using Qp values at 45° and 90° core orientation. Outlier at 90° 30 MPa was omitted from this plot. R^2=0.00427 for this fit.

Core anisotropy effects are more sensitive to increasing effective pressure in the low porosity core than that of high porosity. A linear best fit indicates a rate of change of -.0052 MPa^{-1} for the low porosity core and -.0021 MPa^{-1} for the high porosity core. That is the anisotropy of the low porosity core is attenuated at a rate of about 2.5 times as fast as that of the high porosity carbonate core sample.

At first thought our results regarding the anisotropy of the core samples may seem a bit counterintuitive. One might expect the greater porosity core to be more sensitive to orientation and pressure, however this is not the case. The high porosity core has so many pores that the orientation really does not matter. With the greater number of pores, we can imagine that no matter which way you orientate the core, an elastic wave will interact with so many pores that their orientation is of little importance. That is to say, the greater number of pores makes the

core appear more isometric and homogeneous to an ingoing seismic wave. Following this conclusion, we can understand that for the low porosity carbonate core sample the scarce number of pores causes the interaction between an ingoing seismic wave and an individual pore to be more important, thus leaving core orientation to be more important in a core of lower porosity than that of higher porosity.

When considering the effects of effective pressure on the anisotropy of the core, we must consider the relative change in pore space due to the closure of compliant pores and cracks. The higher porosity sample is less affected by the overall change in pore space as compliant pore closure is small compared to total porosity. Q for the lower porosity sample on the other hand is more susceptible to changes in pressure as the closure of compliant pore space results in a larger percent change in pore space than the high porosity sample.

4.2.3 Rhyolite Temperature Variation

In eight separate experiments the temperature dependence of Q was tested in two separate rhyolite cores. The rhyolite cores were tested dry (air as a pore-filling fluid) at various different temperatures and effective pressures. Effective pressures ranged from .1-50 MPa and temperatures ranged from 21-73°C (Table 7).

Multi-Temperature Experiments	Temperature (°C)	Depth (ft)	Depth (m)	Porosity (%)
1294677940	21°C	3151	960	9.5
1294687827	21°C			
1294779408	36°C			
1294851929	52°C			
1294928993	73°C			

1295445999 1294575261 1295533015 1295014950	38°C 57°C 75°C 80°C	3366	1026	17.5

Table 7: Multi-temperature experiments run on rhyolite core samples.

Figure 45 and Figure 46 below depict multi-temperature data collected for the low and high rhyolite cores respectively. The plots display Qp vs. effective pressure; measurements taken at various different temperatures have been superimposed onto the plot.

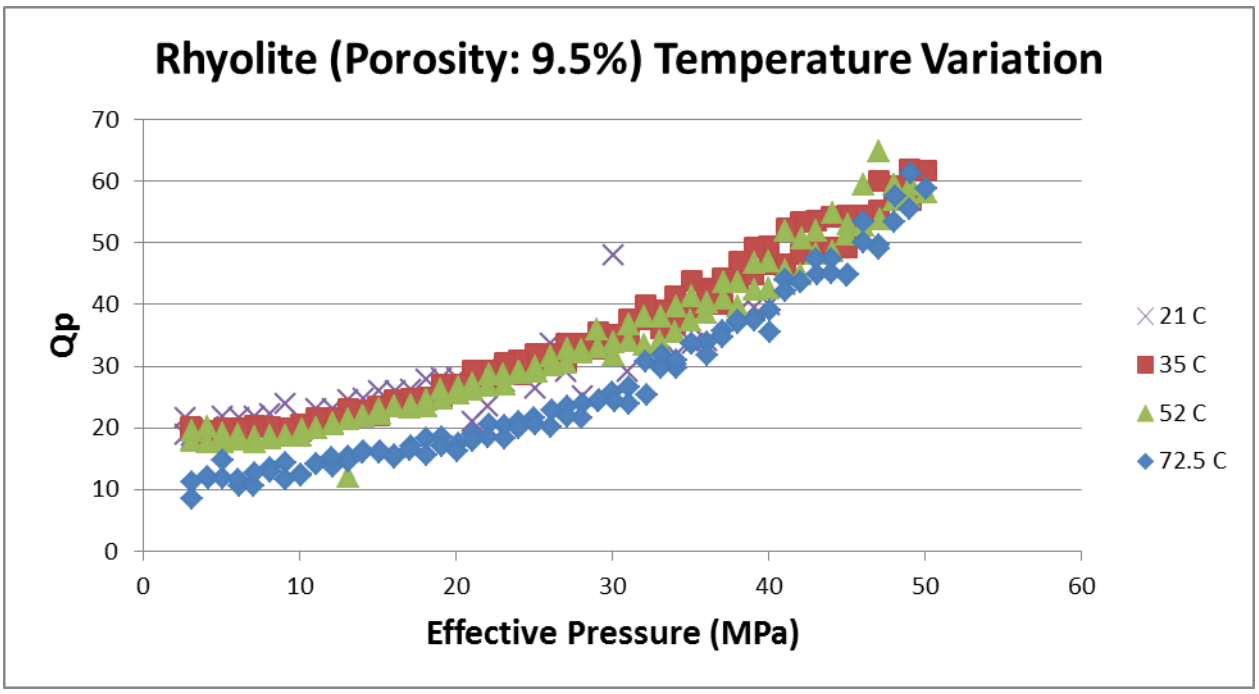

Figure 45: P-wave attenuation factors (Q) against Effective pressure for the low porosity rhyolite sample. Plot contains superimposed Q measurements at various temperatures.

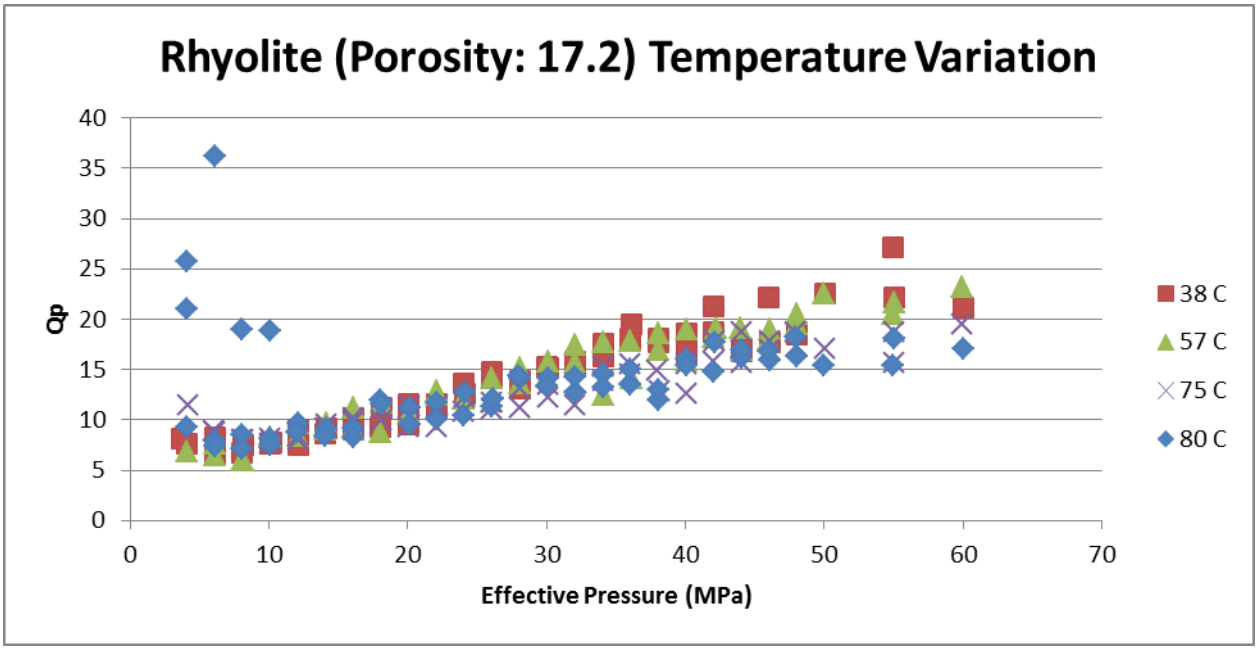

Figure 46: P-wave attenuation factors (Q) against Effective pressure for the high porosity rhyolite sample. Plot contains superimposed Q data at various different temperatures.

The higher porosity core displays a significantly lower value of Q. That is to say that it seems Q is inversely proportional to porosity. These observations are consistent with those of our carbonate cores. We also note that the relationship between seismic wave attenuation and effective pressure is consistent with prior studies where Q is directly proportional to pressure (Winkler and Nur 1979; Prasad and Meissner 1992; Windler and Murphy 1995). This relationship between pressure and Q is primarily due to the effects of compliant pores closing with increasing pressure (Johnston et al. 1979). Q is also weakly dependent on sample temperature. In order to better examine the relationship between the quality factor and the temperature of the core, we plot Qp vs. Temperature for various different effective pressures (Figure 47 and Figure 48).

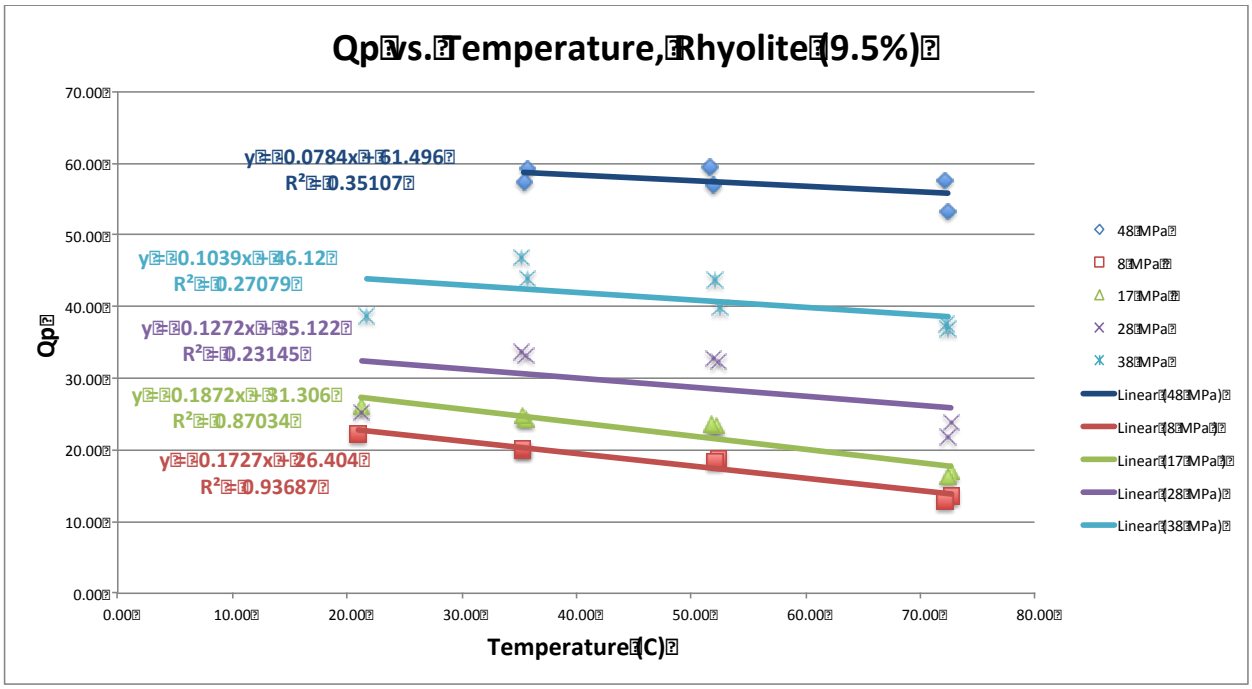

Figure 47: Displays Qp vs. Temperature for the low porosity rhyolite core. Best-fit lines have been fit to data at constant effective pressures.

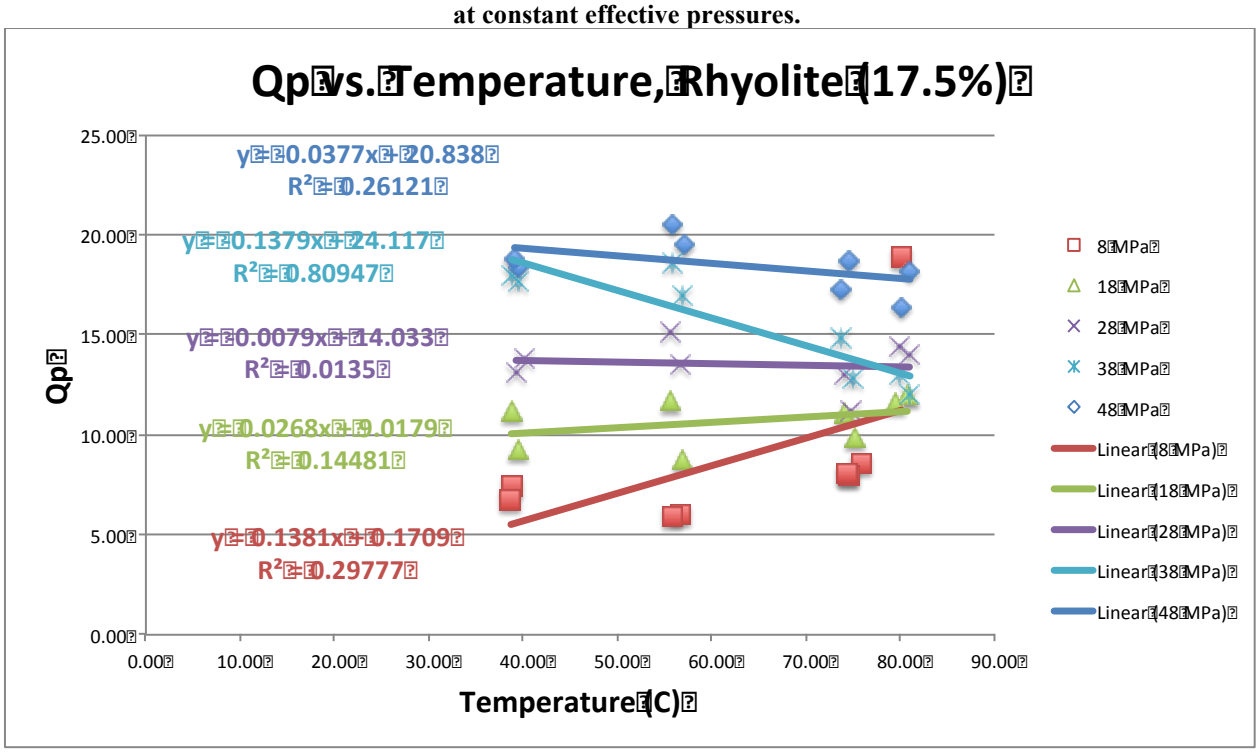

Figure 48: Displays Qp vs. effective pressure for the high porosity rhyolite sample core at various different effective pressures. Best-fit lines have been included for measurements at each effective pressure.

The linear relations between temperature and velocity in addition to Q and temperature at varied effective pressures (8, 17, 28, 38 and 48 MPa) are displayed for the low porosity core in Table 8 below. Y is the wave velocity in meters per second and x is temperature in degrees Celsius unless otherwise indicated. In general, for the low porosity sample, we observe a decrease in velocity as well as Qp with temperature. These results and linear relations can be used to interpolate P, S1 and S2 ultrasonic velocities as well as Qp to higher temperatures. We observe a very consistent linear trend relating temperature to the quality factor. The low porosity sample displays a clear and inversely linear proportionality between Q and temperature.

The high porosity rhyolite sample displayed a much more erratic relationship between Qp, wave velocity and temperature. As can be seen in both Figure 48 as well as Table 9 below, the linear relationships between temperature, Qp, and wave velocity are extremely inconsistent between measurements of varying effective pressures. We observe some measurements that indicate Qp increasing with temperature and others where Qp decreases with increasing temperature. The high porosity sample velocity measurements also display an inconsistent relationship with Qp.

Effective Pressure	**P velocity**	**S1 velocity**	**S2 velocity**	**Qp y=Qp, x=Temp**
8 MPa	y = 1.8203x + 4203.5	y = 0.0563x + 2668.2	y = -0.3438x + 2662.8	y = -0.1727x + 26.404
17 MPa	y = -0.819x + 4365.5	y = -0.2784x + 2703.4	y = -0.6069x + 2685.4	y = -0.1872x + 31.306
28 MPa	y = -1.085x + 4396.4	y = -0.0534x + 2693	y = -0.6544x +	y = -0.1272x +

			2689.2	35.122
38 MPa	y = -1.3435x + 4418	y = -0.3546x + 2712.3	y = -0.6432x + 2691	y = -0.1039x + 46.12
48 MPa	y = -2.0962x + 4457.3	y = -0.4083x + 2720.3	y = -0.5122x + 2686.9	y = -0.0784x + 61.496

Table 8: Displays temperature dependence of ultrasonic velocities where y is ultrasonic velocity in m/s and x is temperature in °C. Core 3151 ft depth, porosity 9.5%

Effective Pressure	P velocity	S1 velocity	S2 velocity	Qp y=Qp, x=Temp
8 MPa	y = -0.8523x + 4176.5	y = 1.5444x + 2460.4	y = 3.134x + 2413.9	y = 0.1381x + 0.1709
17 MPa	y =3.8607x + 4072.6	y = 2.282x + 2458.9	y =1.5214x + 2521.8	y = 0.0268x + 9.0179
28 MPa	y = 2.5205x + 4232.3	y = 2.696x + 2444.7	y = 2.1112x + 2477.1	y = -0.0079x + 14.033
38 MPa	y = -.69x + 4442.3	y =-1.8407x + 2500.4	y = 1.8862x + 2498.3	y = -0.1379x + 24.117
48 MPa	y = 2.2201x + 4310.8	y = 1.2612x + 2561.9	y = 1.6836x + 2539.3	y = -0.0377x + 20.838

Table 9: Displays temperature dependence of ultrasonic velocities for rhyolite core sample from depth 3366 ft, porosity 17.5%. Y represents ultrasonic velocity in m/s and x is temperature in °C.

Ultrasonic seismic attenuation in the low porosity sample does show some minor dependence on temperature. The high porosity sample does not seem to display this dependence possibly due to the more complex internal structure within the core. In order to better understand this result we examine the elastic moduli for these samples. Figure 49 is a plot of Young's Modulus vs. Poisson's ratio for each sample at multiple temperatures. The relationship to temperature is consistent with the rock moduli. We observe the same relationship in the moduli data as with velocity and temperature. The high porosity sample, as previously observed in Qp, displays an erratic non-uniform behavior in terms of elastic properties with regards to temperature whereas the low porosity sample shows some dependence on temperature. From this we can understand that in the low porosity sample, a physical change in elastic nature of the low porosity core is taking place with increasing temperature and affecting the quality factor of the rock. This is not observed in the higher porosity sample.

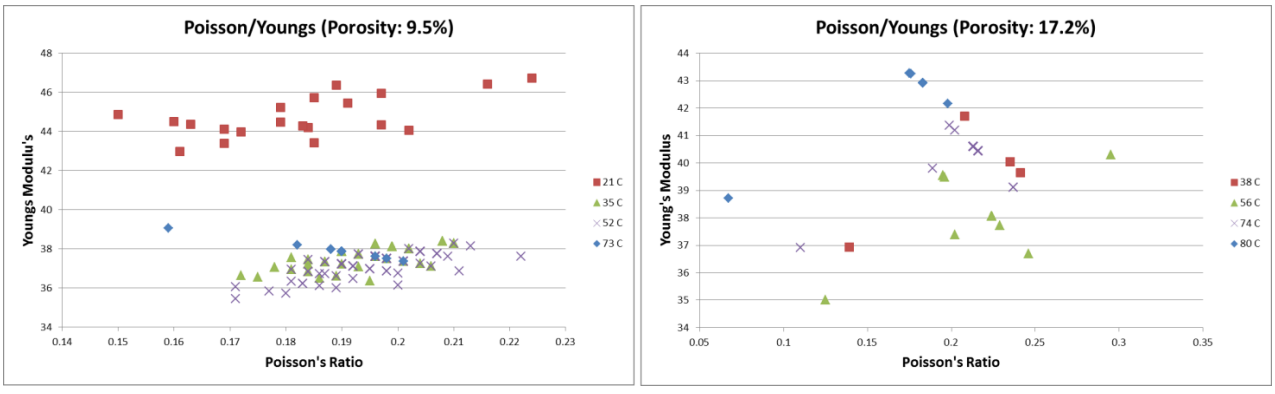

Figure 49: Young's Modulus cross plotted with Poisson's ratio superimposing calculated values at various different temperatures for both high and low porosity samples.

We are able to further interpolate our results in to achieve the slope m and intercept b as a function of effective pressure. From this, we achieve a generalized equation for ultrasonic wave velocity and P wave attenuation as a function of both effective pressure and temperature (Equation 30-Equation 37). Where v is wave velocity Q_p is the P-wave attenuation, P_{eff} is effective pressure, and T is temperature. These results allow us to extrapolate our wave velocities and attenuation to higher temperatures and effective pressures.

Low Porosity Sample (9.5%)

$$v_p = (-0.0818P_{eff} + 1.5682)T + (5.4895P_{eff} + 4215.5) \quad \textbf{Equation 30}$$

$$v_{s1} = (-0.0098P_{eff} + 0.0642)T + (1.1041P_{eff} + 2668.7) \quad \textbf{Equation 31}$$

$$v_{s2} = (-0.0036P_{eff} - 0.452)T + (0.5247P_{eff} + 2668.5) \quad \textbf{Equation 32}$$

$$Q_p = (0.0022P_{eff} - 0.2005)T + (0.8413P_{eff} + 16.702) \quad \textbf{Equation 33}$$

High Porosity Sample (17.2%)

$$v_p = (0.0132P_{eff} + 1.0444)T + (6.4237P_{eff} + 4068.3) \quad \textbf{Equation 34}$$

$$v_{s1} = (-0.0047P_{eff} + 2.4954)T + (2.421P_{eff} + 2418) \quad \textbf{Equation 35}$$

$$v_{s2} = (-0.0243P_{eff} + 2.7431)T + (2.1956P_{eff} + 2429) \quad \textbf{Equation 36}$$

$$Q_p = (-0.0051P_{eff} + 0.1377)T + (0.5574P_{eff} - 1.8592) \qquad \textbf{Equation 37}$$

From our analysis we can conclude that Q has some dependence on temperature however the effects seem to be insignificant within rock of higher porosity. This conclusion is inconsistent with previous studies, which indicate that Q is totally independent of temperatures that are relatively low when compared to the melting point of the rock (Volarovich and Gurevich, 1957; Gordon and Davis, 1968). Although we do see only a minor dependence of Q in our low porosity core, it is important to note that at temperatures approaching the boiling point of pore fluids, Q may become very strongly dependent on temperature (Johnston et al. 1979).

4.3 Q: DISCUSSION AND CONCLUSIONS

Through our analysis of ultrasonic seismic wave attenuation through various lithologies, we have characterized the effects of temperature, porosity, and pore-filling fluids on the quality factor of rock. We have found that Q is inversely proportional to rock porosity and is weakly dependent on temperature. We were able to extrapolate our results to determine a relationship describing ultrasonic velocity and Q as a function of both temperature and effective pressure (Equation 30-Equation 37). Further experimentation is required to assess the relationship between Q and pore-filling fluids. However, carbonate experiments suggest that scattering effects arising heterogeneities is an incredibly dominant process in the attenuation of seismic waves. This dominance could prove useful in detecting heterogeneities in the subsurface. Finally we observed a dependence of Q on core orientation leading us to conclude that anisotropy effects are important in the attenuation of waves.

From this research we conclude that the most dominant physical attributes affecting the value of Q is porosity and rock heterogeneities. Applying Q and wave attenuation to field applications questions seems promising, particularly when paired with stratigraphic knowledge of a region. For example, Q can provide insight into the average porosity of a reservoir/stratigraphic layer, and perhaps even aid us in detecting heterogeneities within the subsurface. It is reasonable to expect that Q might be used to detect and track fluids in the subsurface including sequestered CO_2, however further research is necessary. Our studies indicate that large amounts of information can be retrieved via Q analysis of seismic waves making it a potentially useful attribute in energy exploration and sequestered fluid tracking. Through understanding how seismic waves attenuate, we can gain a better idea of what a collected seismic wave has traveled through.

4.4 ACKNOWLEDGMENTS

This work was supported by the National Energy Technology Laboratory by the United States Department of Energy. In concluding this work I would like to thank everyone who has helped me throughout my career here at the University of Pittsburgh. I would like to thank my family for all of their support through my schooling as well as the wonderful friends I have made throughout my time as a PITT student. Thank you to Dr. Igor Haljasmaa for working with and mentoring me at NETL, I learned and unimaginable amount from Igor. I would also like to thank the Department of Geology and Planetary Science and its excellent staff and faculty. Finally I would like to thank Dr. Tom Anderson, Dr. Dan Bain, and Dr. William Harbert. Without all of you my time PITT would not have been the same. Thank you.

APPENDIX A

ADDITIONAL INFORMATION AND MEASUREMENTS

This Appendix provides additional measurements and information regarding the definitions of elastic moduli, additional velocity and moduli measurements taken for all rhyolite core samples as well as additional Q measurements performed on coal core samples.

A.1 DEFINITION OF MODULI PARAMETERS

Elastic Moduli for a linear isotropic material

(As Defined in the Rock Physics Handbook) (Mavko, Mukerji et al. 2009)

- Bulk Modulus (K): defined as the ratio of the hydrostatic stress to the volumetric strain. The bulk modulus is the reciprocal of compressibility, β, of a material.

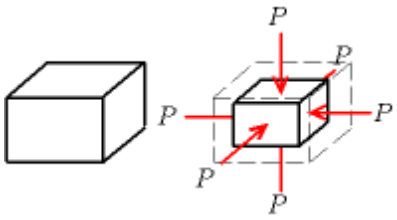

Figure 50: Cartoon depiction of Bulk Modulus. Image Source: Wikipedia <http://en.wikipedia.org/wiki/Bulk_modulus>

- Young's Modulus (E): defined as the ratio of the shear stress to the extensional strain in a uniaxial stress state.

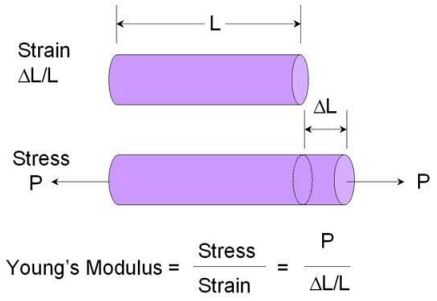

Figure 51: Cartoon depiction of Young's Modulus. Image Source: <http://www4.ncsu.edu/~franzen/public_html/CH795N/dft_modules/polymer_module/crystalline/elastic_constants.htm>

- Lame's First Parameter (λ): Is often thought to have no physical meaning, however can be viewed as the rigidity of the material.
- Shear Modulus (μ): defined as the ratio of the shear stress to the shear strain. Some times denoted as G.

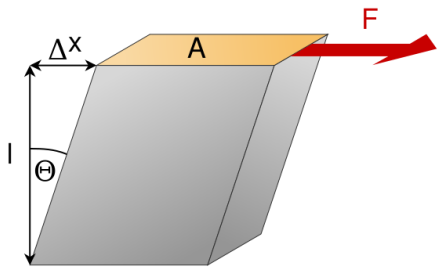

Figure 52: Cartoon depiction of shear modulus stress to strain relationship. Image source: Wikipedia <http://en.wikipedia.org/wiki/Shear_modulus>

- Poisson's Ratio (ν): defined as minus the ratio of the lateral strain to the axial strain in a uniaxial stress state.

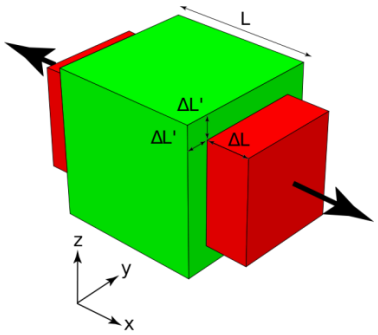

Figure 53: Cartoon depiction of the P-Wave Modulus stress to strain relationship. Image Source: Wikipedia <https://en.wikipedia.org/wiki/Poisson's_ratio>

- P-Wave Modulus (M): defined as the ratio of the axial stress to the axial strain in a uniaxial strain state.

A.2 ULTRASONIC VELOCITY AND ROCK MODULI MEASURMENTS: RHYOLITE

Figure 54 through Figure 58 below provide additional data and measurements for rhyolite rock cores from the geothermal field. The plots depict ultrasonic wave velocity measurements vs. effective pressure as well as moduli cross plots of Young's modulus vs. Poissons' ration for different core depths. We note that the wave velocity increases with effective pressure. In these plots we can observe the closure of compliant pores as pressure increases. We can see that the seismic velocities start relatively low and begin to increase with effective pressure. The leveling off of ultrasonic wave velocities indicates that the closure of compliant pores. The effective pressure, at which velocity ceases to increase, is the pressure at which all compliant pores have been closed.

The effects of increasing effective pressure on the sample and closing compliant pores can also be viewed in the cross plots of Young's modulus, and Poisson's ratio below. We observe in samples with high compliant pore behavior (ex. Core depth 3884 ft) that changes in the elastic moduli are also large. Samples displaying little change in seismic velocity with pressure, i.e. few compliant pores, (ex. Core depth 3151 ft) we observe very consistent values of Young's modulus and Poisson's ratio.

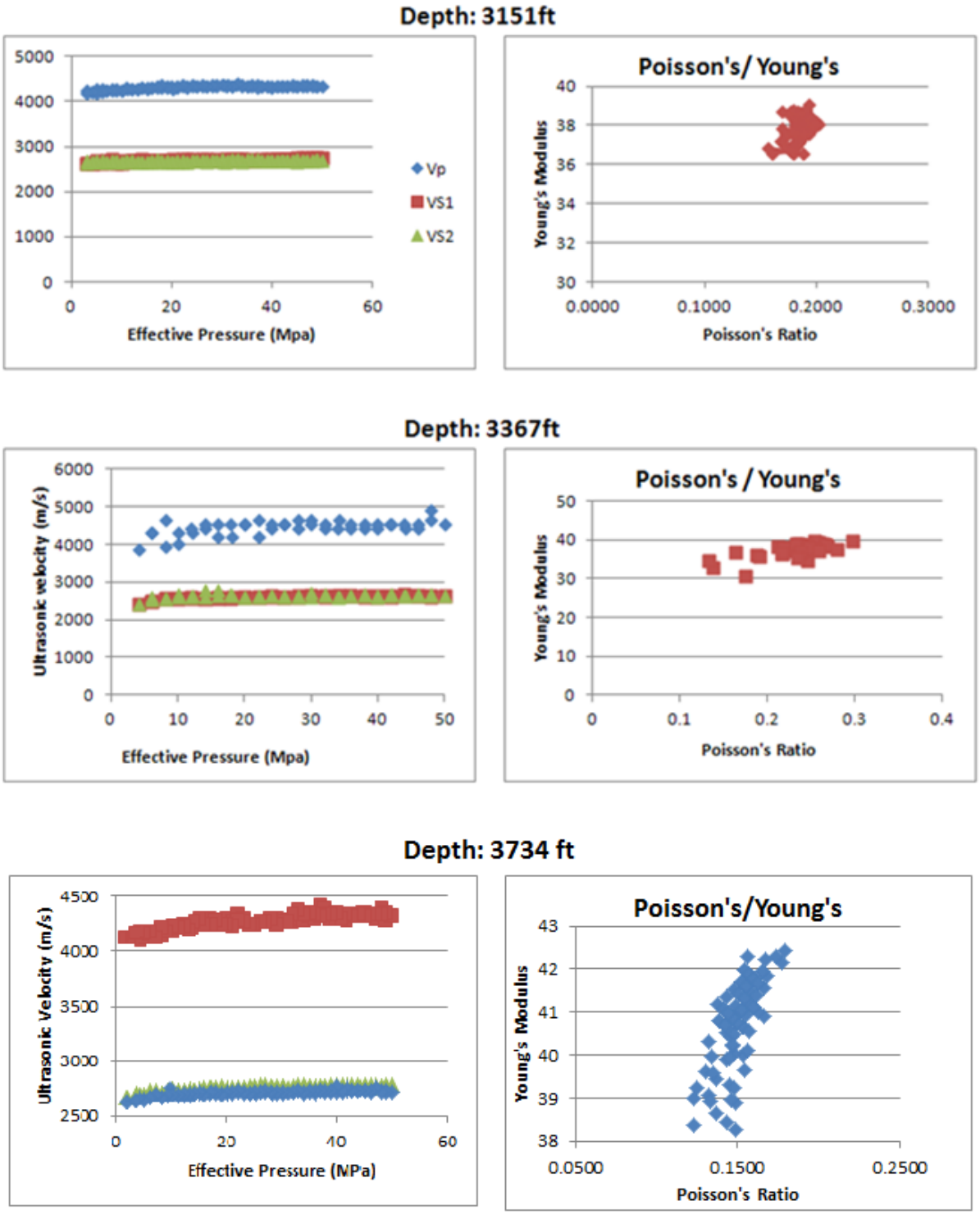

Figure 54: Variation of ultrasonic P, S1, S1, Poisson's ratio and Young's modulus during variation of effective pressure between 0.1 and 50 MPa.

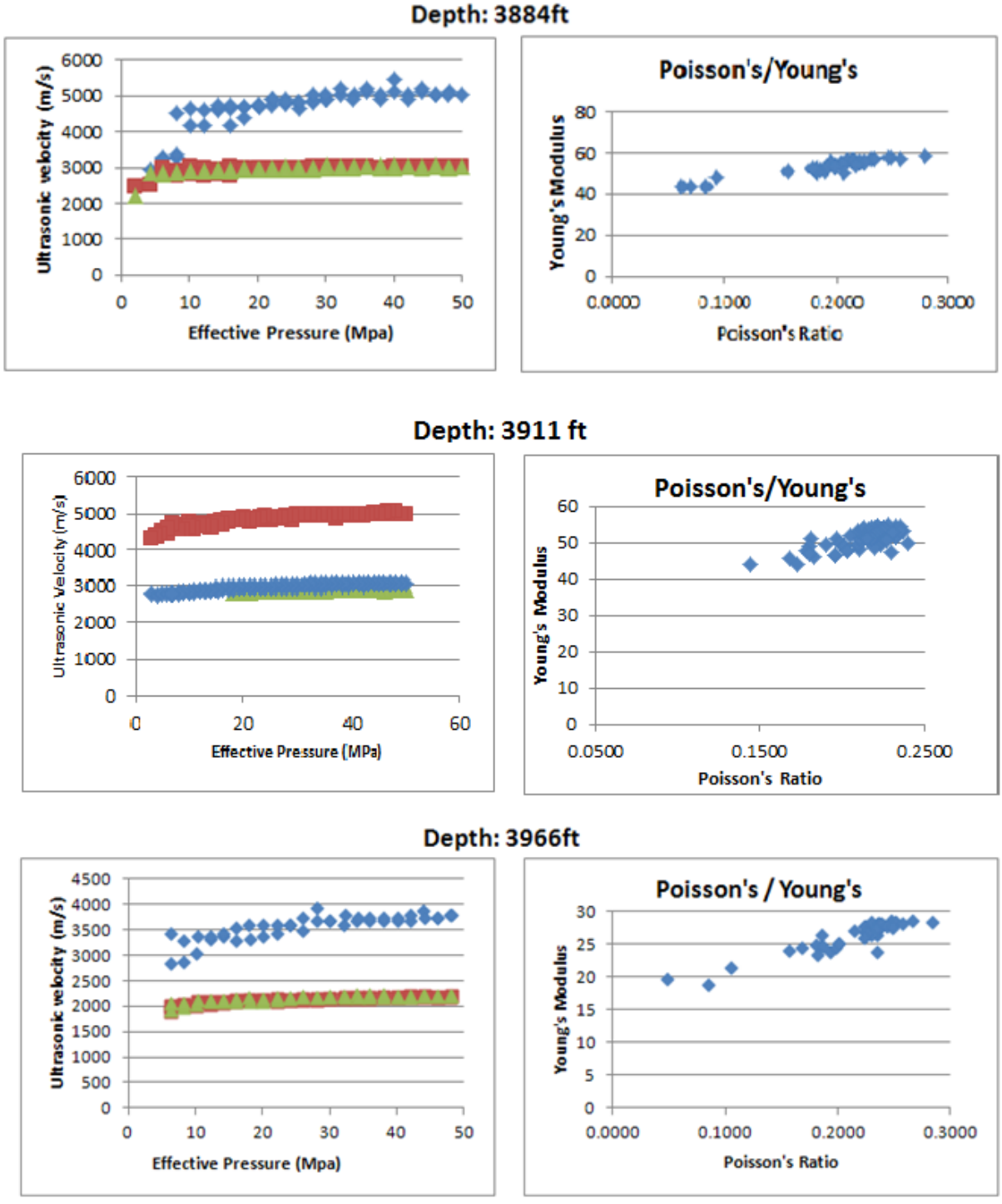

Figure 55: Variation of ultrasonic P, S1, S1, Poisson's ratio and Young's modulus during variation of effective pressure between 0.1 and 50 MPa.

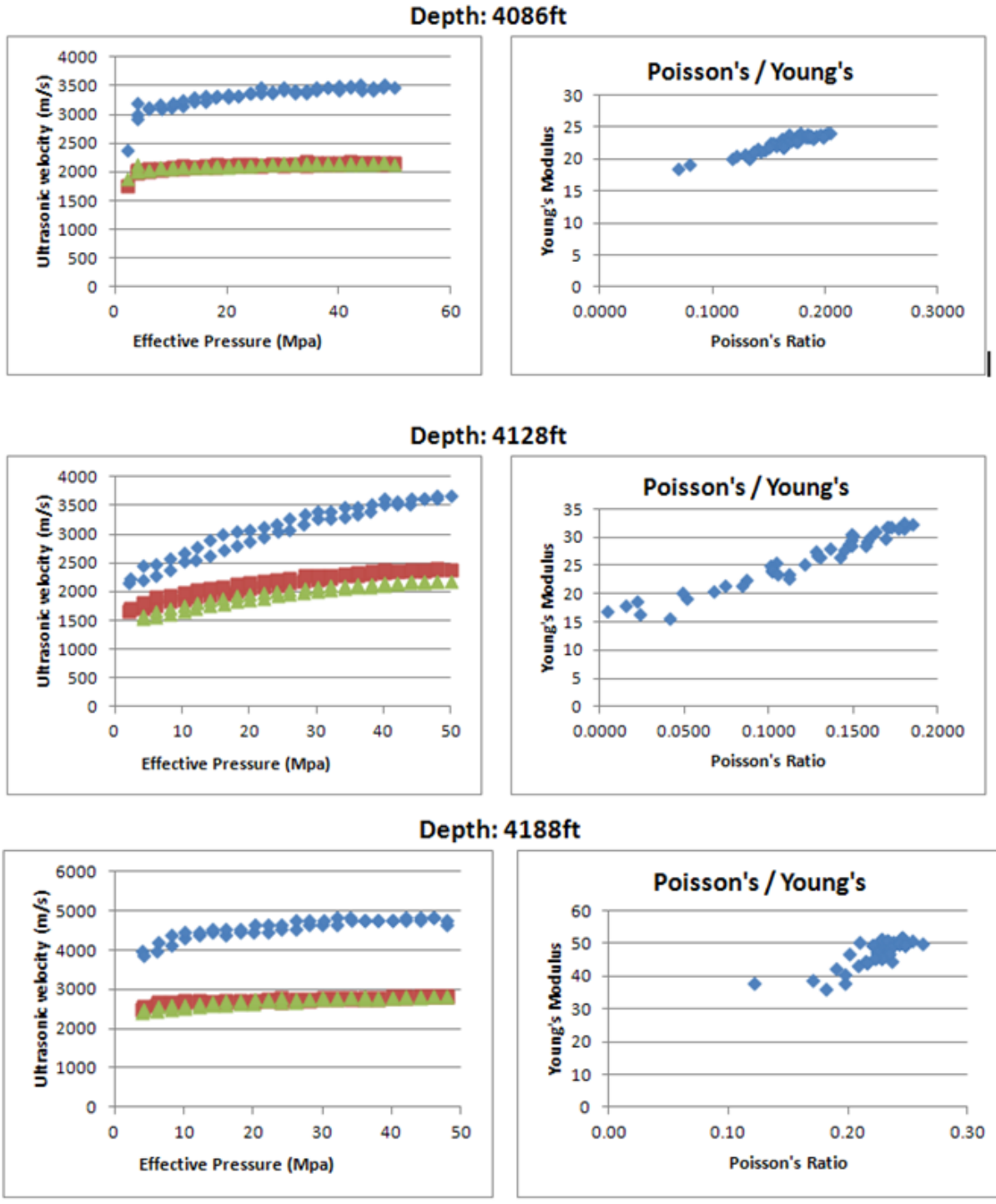

Figure 56: Variation of ultrasonic P, S1, S1, Poisson's ratio and Young's modulus during variation of effective pressure between 0.1 and 50 MPa.

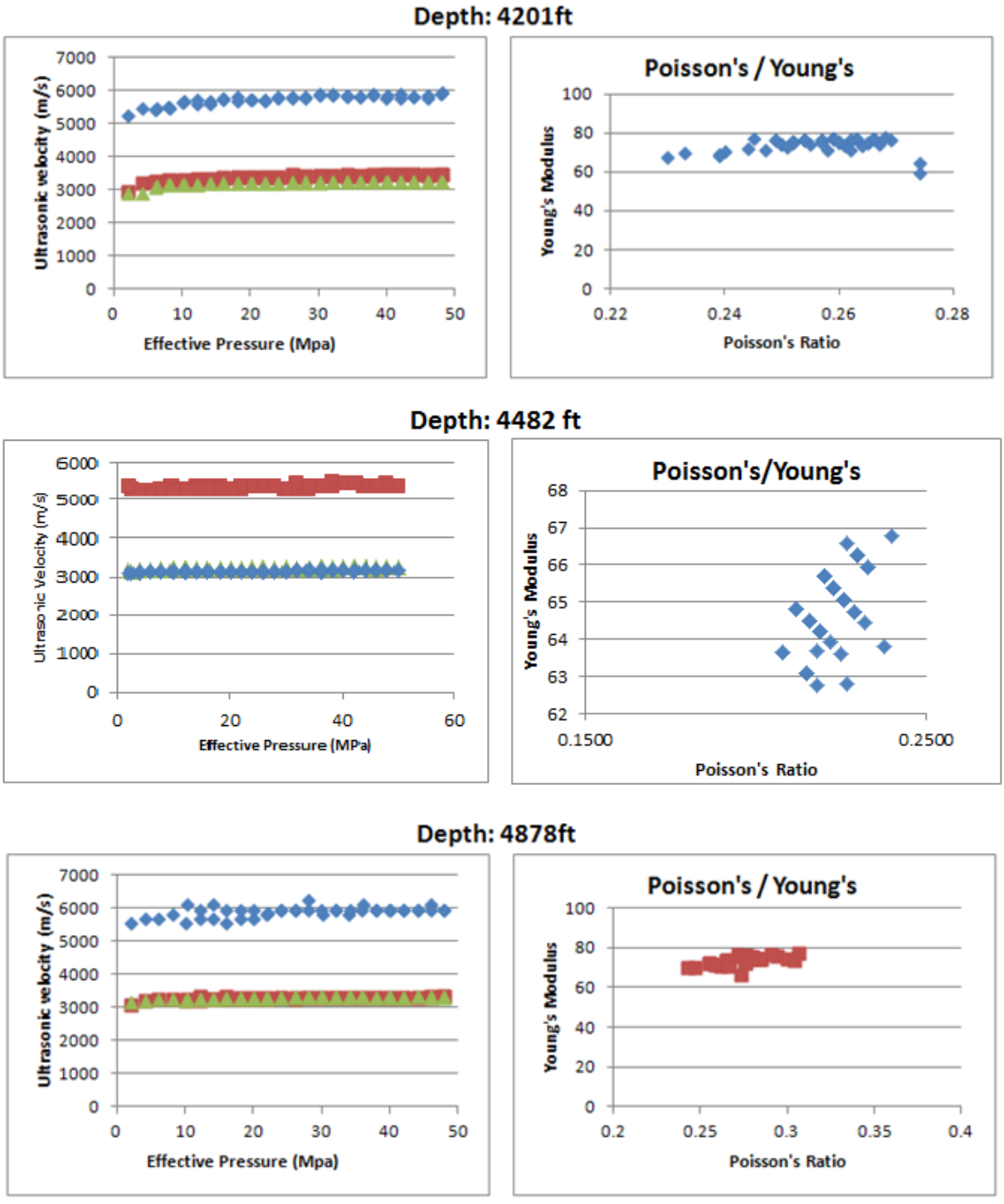

Figure 57: Variation of ultrasonic P, S1, S1, Poisson's ratio and Young's modulus during variation of effective pressure between 0.1 and 50 MPa.

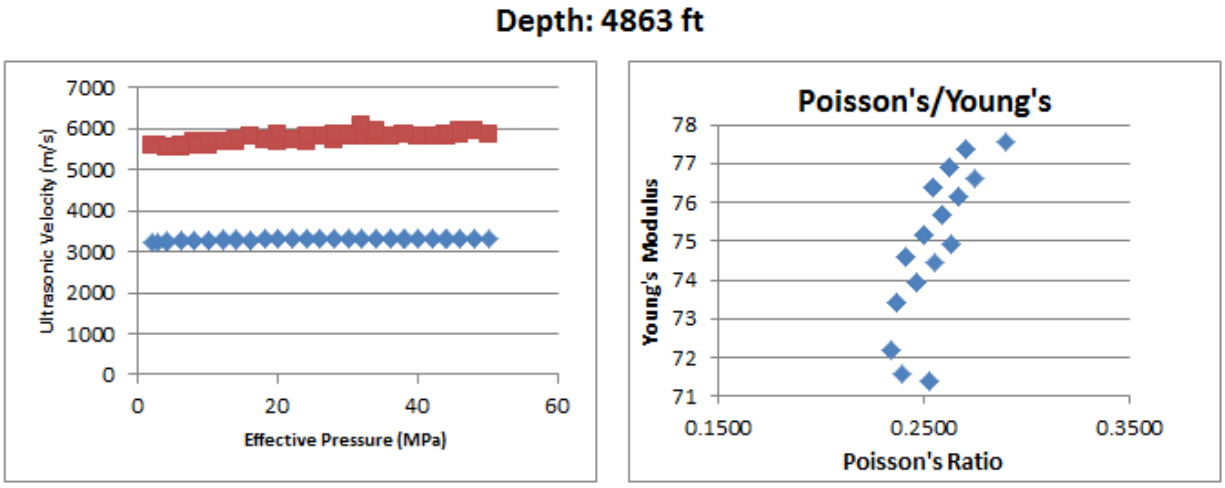

Figure 58: Variation of ultrasonic P, S1, S1, Poisson's ratio and Young's modulus during variation of effective pressure between 0.1 and 50 MPa.

A.3 Q MEASUREMENTS: COAL

Ultrasonic measurements were also performed on coal rock cores as well. Three coal samples were tested and Q was calculated for each and information regarding these calculations is displayed in the table below. Because of the brittle nature of Coal these experiments were performed at low effective pressures. The value of Q displayed below is the average of several low-pressure experiments on the core sample (Effective Pressure <10MPa). Although these experiments were run at low pressures, ultrasonic wave velocities in coal core samples have been shown to be dependent on the confining pressure (Morcote et al. 2010). With this knowledge we can expect that Q will also be dependent on the effective pressure (confining-pore pressure) as it was in previous experiments.

Experiments	Porosity (%)	Dry Density	Depth (m)	Depth (ft)	Qp (Average)
1262108878	0.9	1.28	400	1312	24.77
1259947152 1253285440	1.63	1.28	400	1312	15.73
1247147065 1246554441 1245419098	-	1.3	440	1443.5	27.32

Table 10: Ultrasonic wave attenuation measurements performed on coal core samples.

APPENDIX B

MATLAB SCRIPT FOR THE CALCULATION OF Q

```
alumdt=1E-8; % Time Step
alumt0=0+alumdt; % Start pick point
alumFs=1/alumdt; % Sampling Frequency
L=9999; % Length
alumt=(0:L-1)*alumdt; % Time array by steps of dt



%%%%%%%%%%%%%%%%%%%%%%%%%%%%%%%%
%Alum P clipping and spectrum

alumAmplP=alumdata (9:10008,5); % Amplitude Array P wave
alumAmplP2=alumdata (9:10008,4); % Amplitude Array P wave

NFFT=2^nextpow2(L);
alumfP=alumFs/2*linspace (0,1,NFFT/2+1);
alumAmplP_2=alumAmplP (1:L); % Amplitude through all steps
alumAmplP2_2=alumAmplP2 (1:L);
alumYP=fft (alumAmplP_2,NFFT)/L;
```

```
alumYP2=fft (alumAmplP2_2,NFFT)/L;
absalumYP=abs(alumYP);

AlumSpectrum = [transpose(alumfP),2*absalumYP(1:NFFT/2+1)];
absoluteRange = (0:1500:1.25*10^8);
alumYYP =
interp1(transpose(AlumSpectrum(1:8193,1)),AlumSpectrum(1:8193,2),absoluteRang
e);

alumPick = find(alumAmplP > .025, 1, 'first') - 357;
alumPickEnd = alumPick + 1071;
alumTimePick = (alumPick*alumdt:alumdt:alumPickEnd*alumdt);
ClippedAlumWave = alumAmplP(alumPick:alumPickEnd);
ClippedAlumT = (alumTimePick);
TaperClippedAlumWave =
window(@hamming,numel(ClippedAlumT)).*transpose(ClippedAlumWave)';

alumL2 = length(alumTimePick);
NFFT=2^nextpow2(alumL2);
alumfP=alumFs/2*linspace (0,1,NFFT/2+1);
ClippedalumAmplP_2=TaperClippedAlumWave; % Amplitude through all steps
ClippedalumYP=fft (ClippedalumAmplP_2,NFFT)/alumL2;
absClippedalumYP = abs(ClippedalumYP);

ClippedAlumSpectrum =
[transpose(alumfP),2*absClippedalumYP(1:NFFT/2+1)];
absoluteRange = (0:1500:1.25*10^8);
```

```
      ClippedalumYYP                                                    =
interp1(transpose(ClippedAlumSpectrum(1:1025,1)),ClippedAlumSpectrum(1:1025,2
),absoluteRange);
      %%%%%%%%%%%%%%%%%%%%%%%%%%%%%%%%%%%%

      A = 20;
      B = 2*A;
      C = 3*A;

      for n = 1 : 1 : A

      AmplP=data (9:10008,n); % Amplitude Array P wave
      ConfPressure = infodata(n,2);
      PorePressure = infodata(n,3);
      EffectivePressure = (ConfPressure - PorePressure);
      Temperature = infodata(n,4);
      Pvelocity = infodata(n,20);
      Porosity = infodata(n,16);
      Experiment = infodata(n,19);
      Length = infodata(n,8);
      Diameter = infodata(n,10);

      %dt=AmplP(7,1); % Time Step
      dt = 1E-8;
      t0=0+dt; % Start pick point
      Fs=1/dt; % Sampling Frequency
      L=9999; % Length
      t=(0:L-1)*dt; % Time array by steps of dt
```

```
scale = alumdt/dt;

NFFT=2^nextpow2(L); % Nyquist Frequecy maybe, length of Fourier window
fP=Fs/2*linspace (0,1,NFFT/2+1);
AmplP_2=AmplP (1:L); % Amplitude through all steps
YP=fft (AmplP_2,NFFT)/L;
absYP=abs(YP);

Spectrum = [transpose(fP),2*absYP(1:NFFT/2+1)];
absoluteRange = (0:1500:1.25*10^8);
YYP =
interp1(transpose(Spectrum(1:8193,1)),Spectrum(1:8193,2),absoluteRange);

afterpicker = AmplP(1000:L);
Pick = find(afterpicker > .001, 1, 'first') - round(357*(scale)) +
1000;
PickEnd = Pick + round(1071*(scale));
TimePick = (Pick*dt:dt:PickEnd*dt);
ClippedAmplP = AmplP (Pick:PickEnd);
ClippedT = (TimePick);
TaperClippedAmplP =
window(@hamming,numel(ClippedT)).*transpose(ClippedAmplP)';

L2 = length(TimePick);

NFFT=2^nextpow2(L2); % Nyquist Frequecy maybe, length of Fourier window
```

```
fP=Fs/2*linspace (0,1,NFFT/2+1);
ClippedAmplP_2=TaperClippedAmplP; % Amplitude through all steps
ClippedYP=fft (ClippedAmplP_2,NFFT)/L2;
ClippedabsYP=abs(ClippedYP);

ClippedSpectrum = [transpose(fP),2*ClippedabsYP(1:NFFT/2+1)];
absoluteRange = (0:1500:1.25*10^8);
ClippedYYP                                                                    =
interp1(transpose(ClippedSpectrum(1:length(fP),1)),ClippedSpectrum(1:length(f
P),2),absoluteRange);

figure(1)

subplot(2,1,1)
hold on
plot(alumt, alumAmplP(1:9999))
title('Aluminum Wave-Form')
xlabel('Time (s)')
ylabel('Amplitude')
hold on
line([alumPick*alumdt alumPick*alumdt], [-.15 .15])
line([alumPickEnd*alumdt alumPickEnd*alumdt], [-.15 .15])

subplot(2,1,2)
hold on
plot(absoluteRange,alumYYP)
title('Aluminum Spectrum')
xlabel('Frequency (Hz)')
```

```
ylabel('Amplitude')
xlim([0 1.5E6])



figure(2)
subplot(2,1,1)
hold on
plot(ClippedAlumT,TaperClippedAlumWave)
title('Aluminum Wave-Form Initial Peak')
xlabel('Time (s)')
ylabel('Amplitude')

subplot(2,1,2)
hold on
plot(absoluteRange, ClippedalumYYP)
title('(Clip) Aluminum Spectrum')
xlabel('Frequency (Hz)')
ylabel('Amplitude')
xlim([0 1.5E6])



figure(3)
subplot(2,1,1)
hold on
plot(t,AmplP (1:9999))
title('Rock Core Waveform')
xlabel('Time (s)')
ylabel('Amplitude')
```

```
subplot(2,1,2)
hold on
plot(absoluteRange,YYP)
title('Rock Core Wave-Form')
xlabel('Frequency (Hz)')
ylabel('Amplitude')
xlim([0 1.5E6])


figure(4)
subplot(2,1,1)
hold on
plot(ClippedT,TaperClippedAmplP)
title('Rock Core Waveform Initial Peak')
xlabel('Time (s)')
ylabel('Amplitude')


subplot(2,1,2)
hold on
plot(absoluteRange,ClippedYYP)
title('Rock Core Wave-Form')
xlabel('Frequency (Hz)')
ylabel('Amplitude')
xlim([0 1.5E6])


Ratio = (ClippedalumYYP./ClippedYYP);
LNRatio = log(Ratio);
```

```
figure(5)
subplot(2,1,1)
hold on
plot(absoluteRange,ClippedYYP, 'r')
plot(absoluteRange, ClippedalumYYP, 'b')
xlabel('Frequency (Hz)')
ylabel('Amplitude')
title('Wave Spectra Inital Peaks P')
xlim([0 1.5E6])

subplot(2,1,2)
hold on
plot(absoluteRange(1:1500),LNRatio(1:1500))
title('P Ratio Slopes');
xlabel('Frequency (Hz)')
ylabel('ln(alumSpectrum/SampleSpectrum)')
xlim([0 15E5])

clipLNRatio = LNRatio(35:782);
clipabsoluteRange = absoluteRange(35:782);

hold on
% Fit a line thru the data and plot the result over the data plot
[temp,error]  =  polyfit(clipabsoluteRange,clipLNRatio  ,1);  %  least
squares fitting to a line
a1 = temp(2); % y-intercept of the fitted line
a2 = temp(1); % slope of fitted lines
%plot(clippedfP,temp)
```

```
Rstat=error;
Pratiofit = a1+a2*clipabsoluteRange;
plot(clipabsoluteRange,Pratiofit, 'r')
hold on

clipLNRatio2 = LNRatio(135:782);
clipabsoluteRange2 = absoluteRange(135:782);
% Fit a line thru the data and plot the result over the data plot
[temp,error]  =  polyfit(clipabsoluteRange2,clipLNRatio2  ,1);  %  least
squares fitting to a line
a3 = temp(2); % y-intercept of the fitted line
a4 = temp(1); % slope of fitted lines
%plot(clippedfP,temp)
Rstat=error;
Pratiofit2 = a3+a4*clipabsoluteRange2;
%plot(clipabsoluteRange2,Pratiofit2, 'g')
hold on

clipLNRatio3 = LNRatio(35:300);
clipabsoluteRange3 = absoluteRange(35:300);
% Fit a line thru the data and plot the result over the data plot
[temp,error]  =  polyfit(clipabsoluteRange3,clipLNRatio3  ,1);  %  least
squares fitting to a line
a5 = temp(2); % y-intercept of the fitted line
a6 = temp(1); % slope of fitted lines
%plot(clippedfP,temp)
Rstat=error;
Pratiofit3 = a5+a6*clipabsoluteRange3;
```

```
%plot(clipabsoluteRange3,Pratiofit3, 'k')
hold on

%Q-Calculation
QPinverse=((Pvelocity/(pi*Length*.001))*a2);
QpRed = (1/QPinverse);

QPinversegreen =((Pvelocity/(pi*Length*.001))*a4);
QpGreen = (1/QPinversegreen);

QPinverseblack =((Pvelocity/(pi*Length*.001))*a6);
QpBlack = (1/QPinverseblack);

fprintf('Pslopes(red) %u Pslopes(green) %u Pslopes(black) %u
EffectivePressure %u Experiment %u Temperature %u Pvelocity %u Porosity %u
Length %u Diameter %u Qp(red) %u Qp(green) %u Qp(black) %u \n', a2, a4, a6,
EffectivePressure, Experiment, Temperature, Pvelocity, Porosity, Length,
Diameter, QpRed, QpGreen, QpBlack)



end
```

BIBLIOGRAPHY

Bear, J. (1972). Dynamics of Fluids in Porous Media. New York, Elsevier.

Brohmal, G., Crandall, D., Eastman, H., Harbert, B., Haljasmaa, I., Sirwardane, H., Disenhof, C., Magdalena, G., Roberts, E., Gyovai, K., and Soong, Y. (2011). "Core Evaluation: Brady's Hot Springs Well BCH-03, U. S. Department of Energy." U. S. Department of Energy(DE-PS36-09GO99017).

Castagna, J. and H. Swan (1997). "Principles of AVO crossplotting." The Leading Edge **16**(4): 337-344.

Castagna, J. P. and H. W. Swan (1997). "Principles of AVO crossplotting." The Leading Edge **16**(4): 337-344.

Çoruh, J. K. C. a. C. (2004). "Basic Theory of Exploration Seismology", Elsevier.

Faulds, J., et al. (2010). "Structural Assessment and 3D geological modeling of the Brady's Geothermal area, Churchill county (Nevada, USA): A Preliminary Report". 35 th Workshop on Geothermal Reservoir Engineering, Stanford University, Stanford, California.

Faulds, J. E., et al. (2002). "Geologic setting and preliminary analysis of the Desert Peak-Brady geothermal field, western Nevada." Transactions-Geothermal Resources Council: 491-494.

Gassmann, F. (1951). "Elasticity of porous media." Vierteljahrschrift der Naturforschenden gesellschaft in Zurich **96**: 1-21.

Generazio, E., et al. (1988). Imaging Subtle Microstructural Variations in Ceramics with Precision Ultrasonic Velocity and Attenuation Measurements. Review of Progress in

Quantitative Nondestructive Evaluation. D. Thompson and D. Chimenti, Springer US**:** 1237-1246.

Goodway, B. (2010). "The magic of Lamé." The Leading Edge **29**(11): 1432-1432.

Goodway, B., et al. (1997). "Improved AVO Fluid Detection And Lithology Discrimination Using Lamé Petrophysical Parameters;"λρ", μρ, λμ Fluid Stack", From P And S Inversions". 1997 SEG Annual Meeting.

Goodway, W. (2001). "AVO and Lamé constants for rock parameterization and fluid detection." CSEG Recorder **26**(6): 39-60.

Hoffe, B. H., et al. (2008). AVO interpretation in LMR space: A primer, CSEG, Expanded Abstracts.

Johnston, D. H., et al. (1979). "Attenuation of seismic waves in dry and saturated rocks: II. Mechanisms." Geophysics **44**(4): 691-711.

Keslin, J. (1978). "Viscosity of Liquid Water in the Range—8 C to 150 C." J. Phys. Chem. Ref. Data **7**(3).

Mavko, G., et al. (2009). The rock physics handbook: Tools for seismic analysis of porous media, Cambridge University Press.

Owino, J. and L. Jacobs (1999). "Attenuation Measurements in Cement-Based Materials Using Laser Ultrasonics." Journal of Engineering Mechanics **125**(6): 637-647.

Prasad, M. and R. Meissner (1992). "Attenuation mechanisms in sands: Laboratory versus theoretical (Biot) data." Geophysics **57**(5): 710-719.

Purcell, C. C. (2012). "Velocity Measurements in Reservoir Rock Samples from a Limestone Unit using Various Pore Fluids, and Integration with Well Logs and Seismic Data. " University of Pittsburgh.

Rutherford, S. R. and R. H. Williams (1989). "Amplitude-versus-offset variations in gas sands." Geophysics **54**(6): 680-688.

Shuey, R. (1985). "A simplification of the Zoeppritz equations." Geophysics **50**(4): 609-614.

Siriwardane, H., et al. (2009). "Influence of carbon dioxide on coal permeability determined by pressure transient methods." International Journal of Coal Geology **77**(1–2): 109-118.

Toksöz, M. N. and D. H. Johnston (1981). "Seismic wave attenuation", Soc of Exploration Geophysicists.

Velea, D., et al. "Elastic Wave Velocities in Partially Saturated Ottawa Sand." Soil Sci. Soc. Am. J. **64**(4): 1226-1234.

Winkler, K. W. (1983). "Frequency dependent ultrasonic properties of high-porosity sandstones." Journal of Geophysical Research: Solid Earth **88**(B11): 9493-9499.

Winkler, K. W. and W. F. Murphy III (1995). "Acoustic velocity and attenuation in porous rocks." AGU Reference Shelf **3**: 20-34.

Zemanek Jr, J. and I. Rudnick (1961). "Attenuation and dispersion of elastic waves in a cylindrical bar." The Journal of the Acoustical Society of America **33**: 1283.